LES and Unsteady RANS Simulations of Multiple Jet Impingement System

Prithvi Sai Penumadu

Master of Science Thesis

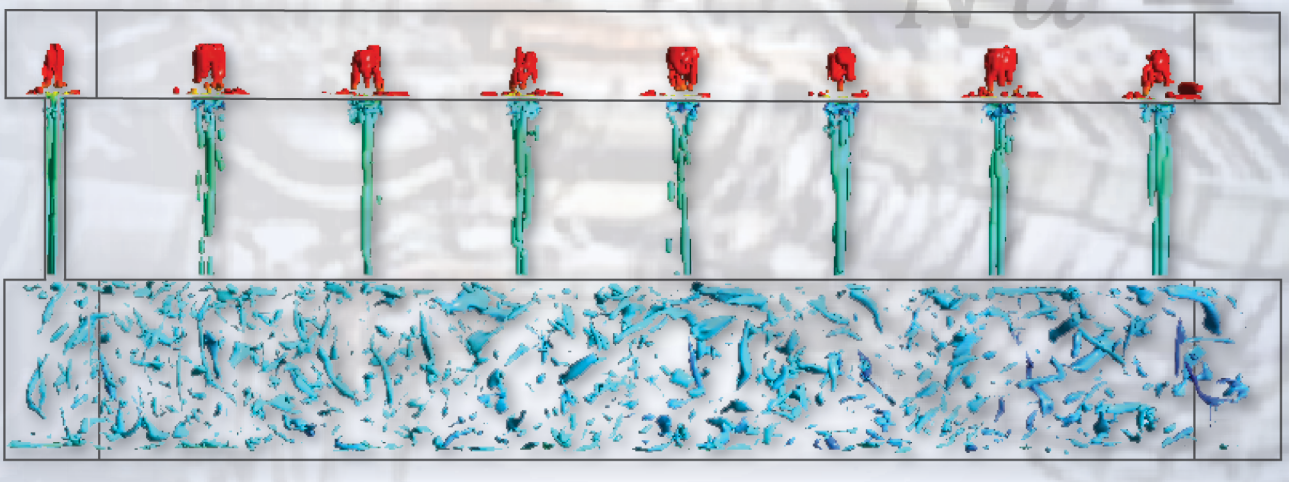

TU Delft Delft University of Technology

Challenge the future

LES AND UNSTEADY RANS SIMULATIONS OF MULTIPLE JET IMPINGEMENT SYSTEM

MASTER OF SCIENCE THESIS

By

Prithvi Sai Penumadu

in partial fulfillment of the requirements for the degree of

Master of Science
in Aerospace Engineering

at the Delft University of Technology (TU Delft),

to be defended publicly on Friday December 11, 2015 at 09:30

Student number:	4306732	
Thesis registration number:	059#15#MT#FPP	
Supervisor:	Dr. Arvind. G. Rao,	TU Delft
Thesis Committee:	Prof. dr. ir. Piero Colonna,	TU Delft
	Dr. Steven. J. Hulshoff,	TU Delft
	Dr. Mauro Gallo,	TU Delft

This thesis is confidential and cannot be made public until 31 December 2015.

TU Delft Delft University of Technology

PREFACE

This document is written as the final deliverable of my M.Sc thesis in the department of aerospace engineering at Delft University of Technology. During the past nine months, I had the opportunity to work with a lot of people who have been instrumental in shaping this work. I would like to take this opportunity to thank all of them from bottom of my heart who constantly supported me to achieve my dreams and goals.

Firstly, I would like to extend my deepest gratitude to my thesis supervisor, Dr. Arvind G. Rao, who helped me to formulate the structure and plan for my thesis. Your critical feedback and constant motivation helped me to accept new challenges and shaped myself into a new individual. I should be gifted to have you as my supervisor. Thank you very much for believing in me and my work.

I would also like to thank Dr. Matteo Pini for his unconditional support and guidance at various crucial levels through out my master thesis. Furthermore, I try appreciate the help of Dhruv Mehta and Rakesh sharma for their valuable inputs during my unsteady simulations. With out them, my thesis would not have been completed on time. Thank you very much for the time you devoted to discuss all my doubts through out this study though you are busy with your Ph.D studies. I am also grateful to my examination committee for devoting time in reviewing and evaluating this content.

Finally, I would like dedicate my master thesis to my beloved grand parents, parents and my uncles Pradeep Kumar and Praveen Kumar with out whom, I would not be in this position. I would also like to thank my house mate Stefan for helping me in designing my thesis cover layout. Last but not least, special thanks to my brother Ram Kumar and my friends Vishwanath, Balu and Bharadwaj for their constant support and encouragement during my master's phase. I shall always relish these memorable moments that I spent during these two years with you guys.

Prithvi Sai Penumadu
Delft, December 2015

SUMMARY

Jet impingement is a subject of extensive research over the years due to its industrial importance and the fundamental physics of heat transfer and turbulence. These jets generate high heat transfer rates with better uniformity on the surface which is to be heated or cooled compared to other heat transfer techniques. However, to study the flow phenomenon and heat transfer rates, conducting experiments overtime for change in design has become expensive. Hence, to reduce the cost and time, the best possible way to study the jets behavior is to perform numerical simulations. With numerical simulations, one can predict the flow physics inside the domain, which is difficult to obtain from the experiments. In the recent times, there have been tremendous developments in terms of computation power and numerical models that have proved to produce good and accurate results for many applications. With these approaches, the flow characteristics can be studied in depth at each and every time step which provides better understanding about the jets behavior inside the array.

However, these new models have to be tested and should be compared with experimental data to see how good these approaches can fit with the experimental results. Moreover, Large-Eddy Simulations (LES) have not been carried out in the past to investigate the flow features in an impinging jet array. So, this master thesis is focused on performing LES and Unsteady Reynolds-averaged Navier-Stokes Simulations (URANS) for multiple impinging jets and validate these CFD results with the experimental data. The primary objective of the thesis is to predict the pressure drop characteristics across the nozzles and the flow channel as the pressure drop directly affects the efficiency of the system. Simulations with Reynolds-averaged Navier-Stokes (RANS) is a good method to analyze these quantities, but it was found that through RANS approach, the results obtained from CFD simulations are over predicted than the experimental values and this deviation increases with increase in Reynolds number. So to analyze these quantities, transient simulations are performed to predict the flow physics and heat transfer characteristics.

From the unsteady RANS and large eddy simulations, it was understood that the major pressure loss occurs inside the nozzles and due to contraction effect at the nozzle's inlet. It was also observed that inside the nozzles the pressure drop occurs differently for the particles near the wall and particles which are in the mean flow. The pressure drop values obtained from the CFD simulations are validated with the analytical and experimental results. It was found that, the results are in good agreement with the analytical results. Furthermore, the heat transfer characteristics obtained from these transient simulations also show a substantial improvement compared to RANS models. The deviation in the results were found to vary between 7% - 10%.

To study the effect of geometrical parameters on the heat transfer and pressure drop characteristics, a sensitivity analysis was performed by varying the nozzle to plate distance and hole diameter. It was noticed that, with the change in nozzle diameter by 10 microns, the total pressure drop of the impingement system is affected significantly. Therefore, when designing these precision systems, it is important to manufacture them accurately as, a minor change in the jet diameter would affect the system performance on a large scale. Finally, It can be concluded that, the unsteady RANS simulations would be a good approach to study the heat transfer characteristics and flow physics inside the array. However, it would be a difficult task for any turbulence model to accurately predict the pressure drop characteristics in the impinging array, as the pressure drop inside the array is extremely sensitive with the change in geometrical parameters.

CONTENTS

LIST OF FIGURES

List of Tables

NOMENCLATURE

Latin Symbols	Description	Units
a	Thermal diffusivity	m^2/s
A	Area	m^2
C_P	Specific heat at constant pressure	J/kg.K
C_s	Smagorinsky coefficient	-
D	Jet diameter	mm
$\mathscr{D}$	Length scale	mm
h	convective heat transfer coefficient	W/m^2 - K
k	Thermal Conductivity	W/m - K
l_s	Smagorinsky length scale	-
$\dot{m}$	Mass flow rate	kg/s
N	Number of jets in an array	-
Nu	Nusselt number	-
P_k	Production of turbulent kinetic energy	m^2/s^2
p	Pressure	N/m^2
Δp	Pressure	N/m^2
Pr	Prandtl number	-
q	Heat input	W
Re	Reynolds number	-
S_{ij}	Strain rate tensor	1/s
T	Temperature	K
T_w	Wall temperature	K
T_∞	Free stream Temperature	K
t	Thickness of jet plate	mm
U	Bulk velocity	m/s
$\mathscr{U}$	Velocity scale	m/s
$\overline{U}$	Mean velocity	m/s
U^+	Velocity scale relative to the wall	-
u'	Fluctuating velocity	m/s
u_τ	Frictional velocity	m/s
$\mathscr{V}$	Volume	m^3
X	Streamwise distance	mm
Y	Spanwise distance	mm
Y^+	Dimensionless wall distance	-
y	distance to the nearest wall	mm
Z	Nozzle to plate distance	mm

Greek Symbols		
Δ	Characteristic mesh size, filter width	mm
δ	Boundary layer thickness	
ϵ	Dissipation	-
η	Kolmogorov length scale	-
κ	Kinetic energy	m^2/s^2
μ	Dynamic viscosity	$N.s/m^2$
ν	Kinematic viscosity	m^2/s
ν_t	Eddy viscosity	m^2/s
ρ	Density	kg/m^3
τ	Shear stress	Pa

ξ	Pressure resistance coefficient	-

Subscripts

av	average
ch	channel
C	cross flow
fr	friction
in	inlet
HP	heated plate
J	jet
n	nozzle
out	outlet
tot	total

Acronyms

CFL	Courant-Friedrichs-Lewy
CFD	Computational Fluid Dynamics
DNS	Direct Numerical Simulations
LES	Large Eddy Simulations
RANS	Reynolds Averaged Navier Stokes
URANS	Unsteady Reynolds Averaged Navier Stokes
SGS	Subgrid Scale Stresses
SyBC	Symmetric Boundary Conditions

1

INTRODUCTION

The current chapter presents an overview of the jet impingement cooling system in section 1.1. This section also explains why jet impingement cooling is the most preferred heat transfer technique in various industrial applications, followed by section 1.2, which discusses the research aim and objectives of the thesis. Having introduced the background of jet impingement cooling concept and the thesis aim and objectives, the structure of this report is presented in section 1.3.

1.1. BACKGROUND

Heating or cooling processes are quite important for any industry. In most cases, high heat transfer rates are required within very short span of time. There are quite many techniques for heating or cooling the surfaces but heat transfer through jet impingement became well established and widely used technique over the past few years, where high heat transfer rates are necessary within short span of time. Figure 1.1 represents a sketch of impinging jet from a round pipe on to a flat surface.

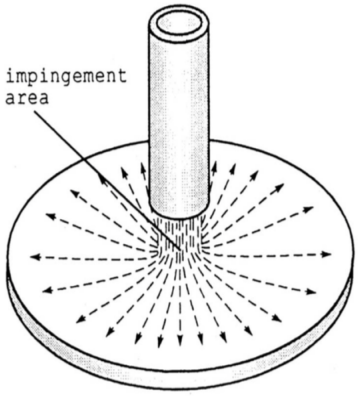

Figure 1.1: Impinging jet from a round pipe on to a flat surface [Peper *et al.*, 1995]

This high-performance technique for cooling or heating involves a series of fluid jets impinging on a surface to promote high rates of heat exchange. This is because direct impingement of turbulent jets onto a

surface leads to high local heat transfer rates [Viskanta, 1993]. These orthogonal jets, when impinged on surfaces, produces high Nusselt numbers in the vicinity of the stagnation point [Cooper *et al.*, 1993]. So, this process is widely applied in process industries, annealing of glass, outer walls of combustion chambers, cooling of gas turbine components, textile drying, paper processing and electronic equipment etc. There are also various types of impinging jet flow with varying flow phenomenon for each different configuration. Some of the main configurations are:

- Single circular nozzle
- Single slot nozzle
- Array of round nozzles
- Array of slot nozzles

For systems which require high localized cooling or heating, a single jet may be sufficient, but if the applied systems require continuous cooling or heating, multiple jets or array of jets are required to enhance the overall heat transfer rates. In the recent years, as the turbines are more prone to experience high temperatures, this technique has gained importance in cooling of the gas turbines stators and rotors. The leading edge of the blade where the flow stagnates experiences high thermal loads due to high turbine inlet temperature. This effect deteriorates the material and the temperature has to be maintained below the melting point by cooling internally. The mid-chord and trailing edge is cooled by rib cooling and pin fins as they do not experience high thermal loads like the leading edge. Figure 1.2 represents the different types of cooling techniques used in a modern rotor blade.

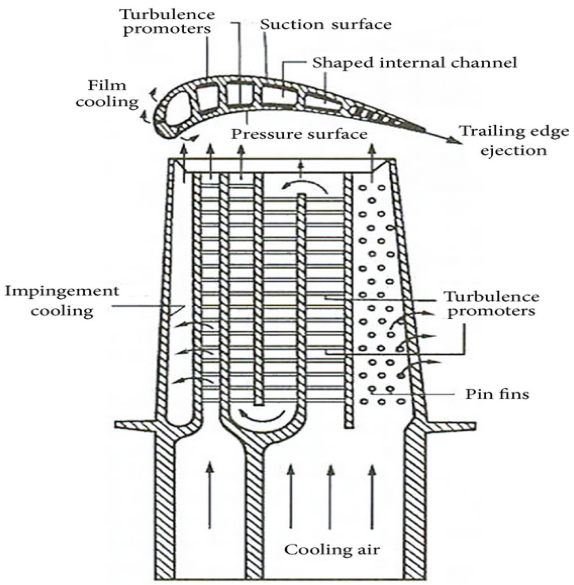

Figure 1.2: Various cooling techniques in rotor blade [Je-Chin-Han, 2002]

The heat transfer of an impinging jet is a complex function of many non-dimensional parameters like Reynolds number, Prandtl number, nozzle-to-surface spacing (Z/D), distance between successive jets (X/D), effect of confinement, nozzle geometry, spanwise distance (Y/D), turbulence effect etc. The design of this equipment is based on many empirical relations derived from experimental data. The most frequently used correlations for single and multiple impinging jets are given by Florscheutz (1981). However, empirical relations do not provide detailed explanation as they just provide a range of correlations for impinging jets. Hence, they cannot be used to design or optimize the heat transfer processes. Most of the research on multiple impinging jets have focused on evaluating the correlations of jet arrays in turbulent regime. Furthermore,

the studies in the past were more focused on the experimental analysis of turbulent jets with high Reynolds number ranging from 3000 - 150000. In addition, majority of the experiments were conducted on single jets, therefore, very little information is known regarding the flow structure of multiple jets in laminar regime. With the multiple jets, the flow structure is more complex due to the interaction between neighboring jets and other interaction mechanisms. [Findlay *et al.*, 1999] and [Matsumoto *et al.*, 1999] have studied the flow pattern and heat transfer characteristics for a turbulent jet array. Though their geometry was a generic one, they studied the flow in a qualitative way. To increase the applications of multiple impinging jets where the available pressure is small or systems with dimensional constraints, the impinging jets behavior has to be studied in laminar regime.

From the previous studies, it is understood that the enhancement of heat transfer of impinging jets lies in the flow and turbulence fields. Some recent works done by Kataoka [Kataoka, 1990] and Cooper [Cooper *et al.*, 1993] have also concluded that, the heat transfer can be enhanced through turbulence fields. Though, a lot of effort has been put to study the flow physics through experimentation, the physics of the impinging flows are not fully understood. The experimental techniques are limited in providing the necessary data. So to understand and discover the physics of turbulence mechanisms and flow interactions, computational fluid dynamics (CFD) has become a generic tool for both industrial and fundamental research. However, the numerical simulation of the impinging jets poses a great challenge. The main methods are direct numerical simulations (DNS), large eddy simulations (LES) and reynolds-averaged Navier-Stokes simulations (RANS). RANS models have dominated the industrial CFD for many decades, but these models hardly provide information about the flow physics. Their intuitive and empirical approximations which are used for closing the Reynolds equations limit their application as a predictive tool. For better understanding of the flow phenomenon, a better approach would be resolving the scales to the smallest to capture the the flow. For these purposes, direct numerical simulations can be used which provides detailed information by capturing full resolution to the smallest eddy scales. However, this approach is very computationally expensive and time consuming.

The recent improvements in LES approach and the computation power increased the applicability in the fundamental research areas. It is expected that LES will soon be a powerful method in industrial applications. However, this approach is limited to low-to-moderate Reynolds numbers, as at high Reynolds numbers, modeling of near wall turbulence and very high mesh resolution requirements limit their application to simple geometries. The current thesis being focused on understanding the flow physics and heat transfer mechanism of multiple impinging jets in low Reynolds number application, modeling of the jet array through LES and unsteady RANS approach would not only provide a good understanding of the flow phenomenon, but also on pressure drop characteristics in the jet array which will contribute to the scientific database to extend the boundaries of the research.

1.2. OBJECTIVES

As discussed in the section 1.1, the concept of jet impingement has been a subject of research for quite a long time. Realizing the interaction between multiple impinging jets and their complex flow phenomenon, the heat transfer and the pressure drop are the key parameters that controls the efficiency of the impinging jet system. Therefore the primary objective of the current thesis study is to gain a better understanding of the flow structure with the heat transfer in jet impinging arrays. This can be achieved by performing numerical investigations of large array of impinging jets in the low Reynolds number region, typically <2000. However, with numerical simulations, there are always uncertainties involved. To accurately predict the flow structure, the following thesis objectives have been formulated:

1. To perform RANS computations of a multiple impinging jet array on a flat surface with different Reynolds number varying in the laminar regime using ANSYS Fluent, a finite volume implicit solver with hexa-

hedral computational grid. These numerical simulations requires a model which captures the heat transfer and flow effects with an appropriate solution to solve the Reynolds Averaged Navier- Stokes (RANS) equations. A suitable RANS model has to be identified which can capture the flow effects accurately by computing different turbulence models. The results have to be validated with experimental data to find out the model which can best represent the realistic conditions.

2. To explore the possibility of unsteady RANS approach for the same impinging jet array to determine the flow and heat transfer characteristics of the impinging system at various time intervals. The fundamental aim is to understand the pressure drop characteristics across the cross-flow channel and impinging nozzles inside the jet array. The pressure drop values obtained will have to be validated with the experimental values to predict the flow conditions and efficiency of the system.

3. To investigate the potential of LES approach in predicting the flow phenomenon of impinging jet array, as the flow and heat transfer mechanism is unique in the array which depends on the jet configuration. Since the near wall region is of utmost importance, a suitable sub-grid scale model has to be identified which can capture the non-uniformities near the wall region.

4. To study the effects of geometrical parameters on the jet impingement system. It is important to understand how the manufacturing tolerances play an important role in influencing the heat transfer and pressure drop characteristics of an impinging array.

5. To draw conclusions from the current study, especially on the pressure drop characteristics of the jet array by maintaining the heat transfer characteristics of the system.

1.3. OUTLINE

This thesis consists of six chapters.

In chapter 2 an overview to theoretical background and literature review is presented. Section 2.1 and section 2.2 discusses the fluid dynamics of single and multiple impinging jets. In section 2.3, an overview on the numerical methods used in the current research is discussed. This section also presents with the governing equations for heat and fluid flow used in the computational methods. A brief description of the experimental setup from literature is given in section 2.4. The experimental setup and the results are used for validating the current numerical investigations.

Chapter 3 begins with a brief description of the computational methodology used in Reynolds-averaged Navier-Stokes (RANS) approach. In section 3.1, a hypothesis of the three eddy-viscosity models used in this research are discussed. Section 3.2 presents with the computational geometry, numerical grid, solution procedure and results obtained through RANS simulations. In section 3.3, the computational methodology and the results obtained through unsteady RANS simulations are discussed.

Chapter 4 introduces the principle methodology behind large eddy simulations (LES). Section 4.1 presents with a brief description on the available sub-grid-scale models in fluent. In section 4.2, the computational domain, mesh requirements for LES approach and the solution procedure is discussed. The results obtained through LES simulations are discussed in section 4.3.

Chapter 5 presents an overview on the sensitivity analysis performed on the multiple jet impingement array to analyze the effect of manufacturing tolerances of the geometrical parameters. In section 5.1, the effect of nozzle to plate distance is analyzed by varying the height between the nozzle exit and the target surface, followed by section 5.2, which discusses the effect of nozzle diameter on the impinging system. In this section, few interesting findings are achieved with respect to the flow phenomenon. In section 5.3, the effect of clogged jet on the impingement system is analyzed by clogging the jet which produces highest local heat transfer rates.

Chapter 6 contains general conclusions drawn from the validation of computational results with the experimental results obtained from the literature.

2

THEORETICAL BACKGROUND AND LITERATURE REVIEW

The current chapter presents an overview of the theoretical background of impinging jets. Section 2.1 explains the flow dynamics and heat transfer characteristics of a single jet, followed by the flow features and heat transfer characteristics of multiple jet arrays in section 2.2. The dependencies of the Nusselt number on the non-dimensional parameters and geometrical parameters are also discussed in the above sections. In section 2.3, the numerical methods that are required to perform the computational simulations to model the impinging jets are discussed. It gives a brief overview on the governing equations for heat and fluid flow. A description of the experimental setup from literature is given in section 2.4. This experimental setup and the results are used for validating the results obtained from the current CFD simulations.

2.1. FLOW STRUCTURE OF AN IMPINGING JET

Jet structure

An impinging jet is commonly divided into three regions on the basis of the flow structure: the free jet region, the wall jet region and the stagnation region. For very high distances between nozzle exit and the impinging surface, the free jet region has three zones: the potential core region, the developing region and fully developed region [Viskanta, 1993]. Figure 2.1 shows the flow structure of a single round impinging jet with different regions in the flow configuration.

2.1.1. FREE JET REGION

In the free jet region, the shear interaction of the jet and the ambient air produces entrainment of mass, momentum and energy. This results in the development of a non-uniform radial velocity profile within the jet, expansion of the jet profile, an increase in total mass flow rate and the change of the jet temperature before it impinges on the surface. The axial velocity of the jet decreases continuously after the jet exits from the nozzle. This is due to the radial spreading of the jet. As discussed earlier, the free jet regions has three sub-divided regimes: the potential core, developing and fully developed regions for high nozzle-to-plate distances.

In the potential core, the velocity remains constant and equal to the nozzle exit velocity. The flow in this region is irrotational. Due to the growth of shear layer surrounding the potential core, the core gradually starts decreasing in width. Initial velocity profile and the turbulence intensity at the nozzle exit are the im-

portant parameters for the length of the potential core. Many works reported that for axisymmetric jets the length typically varies between 5-7 diameters, whereas, for slot jets it varies between 4.5-7.5 slot diameters [Livingood and Hrycak, 1973]. In the free jet region, various characteristic flow structures can be visualized. These are formed in the shear layer. If the jet is in laminar regime, these flow structures can be compared to the Kelvin-Helmholtz instabilities. These instabilities can be classified as linear type as mentioned in the theory.

The instabilities in the shear layer produce a train of vortex rings. These shear layer instabilities are identical to the ones that are explained by the Kelvin-Helmholtz linear stability theory. As they move downstream, these vortices coalesce with the neighboring vortices, also known as vortex pairing. This ultimately will result in a large scale of vortices and the distance between them increases with increased distance from the nozzle. Also, these vortices lose the phase agreement across the jets as they move downstream from the nozzle. The gradual increase of fluctuations will result in the growth of vortex rings and this eventually decreases the level of circumferential cross-correlations [Yule, 1978]. The fluid in the jet gets accelerated or decelerated due to the trains of growing vortices [Kataoka, 1990]. The resulting larger vortex is called the primary vortex. These structures are named as vortices and not eddies due to their coherent structure. In the region between two successive vortex rings, few secondary azimuthal vortices grow and these vortices results in the formation of counter-rotating vortex pairs.

The developing zone starts at approximately 6-8 nozzle diameters downstream the nozzle and the potential core does not exist anymore. In the developing zone, the axial velocity profile caused by the large shear stresses at the jet boundary starts to decay and the turbulence level starts to increase. The level of turbulence or turbulence intensity is defined as the ratio between the root mean square of the axial velocity fluctuations to the initial axial velocity. These large stresses are responsible for turbulence and promotes the entrainment of fluid. In the developed zone, the axial velocity decays linearly, besides linear broadening of the jet which results in the decay of turbulence level. This zone starts at 8 to 10 nozzle diameters downstream of the nozzle [Kataoka, 1990]. Furthermore, in the developed zone, the reynolds stresses becomes self-similar [Pope, 2000] just like the radial velocities due to its much smaller magnitude than the axial components.

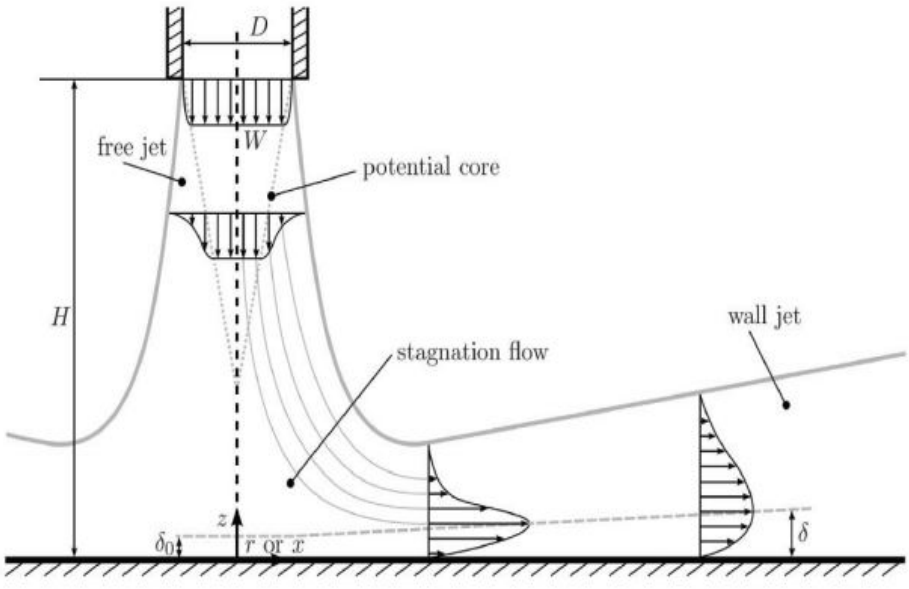

Figure 2.1: Flow structure of a round impinging jet [Viskanta, 1993]

2.1.2. STAGNATION REGION

The stagnation region is characterized by strong curvature of stream lines caused by the impinging plate due to the flow obstruction. On the basis of mean momentum transport equation, [Nishino *et al.*, 1996] showed that the axial transport of the momentum and the normal stresses, in this case turbulent normal stresses, is converted to static pressure. He also claimed, that the change in fluctuations of radial and axial velocity components with respect to radial direction is negligible. The deceleration of axial velocity towards the surface is the main reason for transport of axial momentum towards the surface. whereas, the contribution of turbulent normal stress is due to the presence of momentum which is transported from turbulent field to the mean field near the impinging surface. This results in the negative production of kinetic energy. The axial momentum transport equation can be expressed as follows in cylindrical coordinates:

$$\langle w\rangle \frac{\partial\langle w\rangle}{\partial z} + \frac{1}{r}\frac{\partial r\langle u'w'\rangle}{\partial r} + \frac{\partial\langle w'\rangle}{\partial z} + \frac{1}{\rho}\frac{\partial\langle p\rangle}{\partial z} = 0 \tag{2.1}$$

In the above equation 2.1, u and w are the radial and axial velocity components respectively. r and z are the radial and axial coordinates respectively. From the experiments of [Nishino *et al.*, 1996], the second term in the equation 2.1 proved to be negligible. This finding supports the reason that the normal stresses are converted into static pressure. The production of kinetic energy can be defined as:

$$P_k = 2(\bar{w}^2 - \bar{u}^2).\frac{\partial U}{\partial r} \tag{2.2}$$

In other words, the rate of production of the turbulent kinetic energy on the axis of symmetry is proportional to the difference of the turbulent normal stresses. The data by [Nishino *et al.*, 1996] show that $2(\bar{w}^2-\bar{u}^2)$ < 0 for small nozzle diameters while $\frac{\partial U}{\partial r} > 0$. Therefore, $P_k < 0$ in this region. The pressure diffusion term should compensate for the loss of turbulent kinetic energy caused by the negative production in this region.

2.1.3. WALL JET REGION

In a circular impinging jet, the velocities, turbulence intensities and wall stresses in the radial wall jet are the most important quantities that should be analyzed. Due to the radial spreading of the wall jet, the jet velocities will decrease with increase in the radial distance from the stagnation point but the height of the wall jet increases. With respect to the boundary layer, the wall jet is characterized by a strong near-wall shear layer where the log-law is applied. There are quite a few works relating to the wall jet performed by various researchers. [Poreh *et al.*, 1967] investigated the above mentioned quantities and concluded that the maximum radial wall jet velocity U_m and wall jet height δ will be:

$$U_m \propto r^{-1.1} \tag{2.3}$$

$$\delta \propto r^{0.9} \tag{2.4}$$

The results of [Poreh *et al.*, 1967] showed that the turbulence level and the Reynolds shear stresses in the wall jet are higher compared to the boundary layers. He also suggested that eddies from the shear layers are infiltrating into the boundary layers causing increase in the skin friction. The measurements of the Reynolds stresses indicate that the turbulent shear stress is not proportional to the local gradient of the mean velocities as assumed by the eddy-viscosity model.

2.1.4. EFFECT OF GEOMETRICAL PARAMETERS ON A SINGLE CIRCULAR JET

EFFECT OF NOZZLE TO PLATE DISTANCE (Z/D)

Many researchers in the past have investigated the heat transfer characteristics of a single circular turbulent jet from a pipe impinging on a flat surface. They studied the effect of the nozzle-to-plate distance (Z/D) on the radial profiles of Nusselt number distribution. In general, the Nusselt number is highest in the stagnation point of the jet, for all values of Z/D, and gradually decreases with increasing radial distance. This is caused by the growth of the thermal boundary layer in the wall jet and the decrease of wall jet velocity with increasing radial distance.

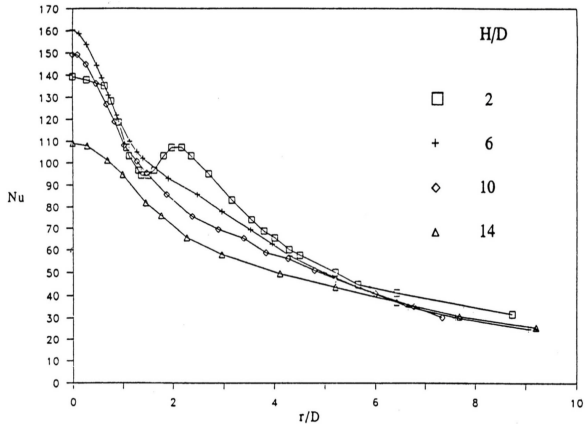

Figure 2.2: Effect of nozzle to plate (Z/D) distance [Baughn and Shimizu, 1989]

From the figure 2.2, it is understood that the highest Nusselt number occurs in the stagnation region at Z/D = 6, which indicates that, the potential core starts to disappear and the developing jet hits the target surface. This transitional jet with high turbulence levels results in enhancing the heat transfer rates at the stagnation region. For low Z/D values, we can see that there exists a second peak between r/D= 1 and 2 and this peak becomes more pronounced with the increase in Reynolds numbers. This non monotonic radial distribution of Nusselt number for smaller Z/D distances is the result of radial wall jet boundary layer transition to turbulent jet or the interaction due to the large scale turbulence in the mixing zone of the core jet. These ring shaped wall eddies are induced consecutively by the large scale eddies hitting the plate and this enhances the local momentum which can also be the reason for the secondary peak.

EFFECT OF NOZZLE SHAPE

Heat transfer characteristics of a single circular jet also depend on the nozzle shape. In fact, [Popiel and Boguslawski, 1986] determined the heat transfer characteristics from a sharp edged orifice and from a bell shaped nozzle at equal Reynolds number. The sharp edged orifice produces a higher center line jet velocity than the bell shaped nozzle due to vena contraction effect. This results in high heat transfer coefficients when compared to the bell shaped nozzles at all radial distances. However, for large nozzle to plate distances, this effect disappears because the flow becomes developed and the axial velocity decays when the distance is high. [Lee and Lee, 2000] presented few correlations for different edges in the orifices. The shape of the edges of orifices also influences the heat transfer to certain extent. The orifice with sharp edge in figure 2.3 produces high heat transfer rates than the other two shapes but it also exhibits quick decay of potential core for increasing nozzle-to-plate distances due to strong instabilities due to the sharp edge.

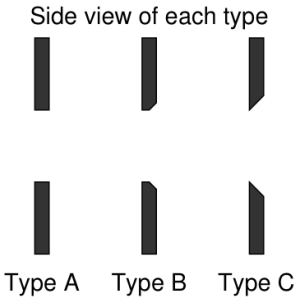

Figure 2.3: Three types of orifice edges tested [Lee and Lee, 2000]

2.2. FLOW STRUCTURE OF MULTIPLE IMPINGING JETS

Multiple impinging jets in an array have the same jet structure as a single impinging jet with the same three flow regions, but there are some differences in the flow physics of multiple jets when compared to the single jets. The individual jets which form multiple jets in an array are influenced by mainly two types of interaction effects that are not observed in single jets. This is mainly due to the presence of neighboring jets. The first interaction is between the adjacent jets prior to the impingement. This is more pronounced and commonly seen with the jets which are closely spaced and sometimes when the nozzle-to-surface distance is relatively large. Second, there can also be interaction effects due to collision of wall jets from the adjacent impinging jets. These effects can also be noticed when the jets are closely spaced or the nozzle-to-surface distance is small with high jet velocity [Viskanta, 1993].

The collision of wall jets causes an interesting flow phenomenon. When the two jets collide, an upwash flow is formed between the two impinging jets because of the interaction between the two wall jets. [Barata, 1996] studied these effects by analyzing three impinging jets. He concluded that there exists an upwash flow between two adjacent impinging jets. It affects the entrainment of the impinging jets and the exhaust air is discharged in two ways. Few traces of air that is formed from the up flow is either entrained into the adjacent jets or it is discharged along the nozzle plate. Furthermore, it is also observed that the exhaust air of the jets in the array flows out forming a cross-flow for the jets. This effect is inevitable and is often observed in the arrays. For low cross-flow velocities, the interaction with the jets forms a vortex around the jets. This is formed due to the cross flow and wall jet interaction. As a result, two counter rotating vortices trail away from that region. If the cross-flow velocities are high, the impinging jets are deflected away from the impinging region which results in the delay in impinging or sometimes impinging is prevented making the jet to get amalgamated in the cross flow. So, the arrangement of the nozzles in the array plays a key and vital role on the flow characteristics of multiple impinging jets. For example, inline, hexagonal or staggered arrangement and several other types. Also, spacing of nozzles play an important role in this case. Figure 2.4 shows the how the upwash flow is generated by collision of wall jets.

2.2.1. EFFECT OF NON-DIMENSIONAL PARAMETERS ON MULTIPLE IMPINGING JETS

As there are lot of different additional quantities which affects the heat transfer of multiple jets compared to single jets, the modeling of multiple jets over single jets is more complicated. The main important parameters that are to be incorporated are the jet to jet spacing, cross-flow, arrangement of nozzles etc. At smaller separation distances, jet interactions from the adjacent jets are reduced to a large extent because the small distance of nozzle-to surface distance prevent the interactions to occur. If the distance is increased, the entrainment and the decay of jet velocity causes interactions to occur at a high probability.

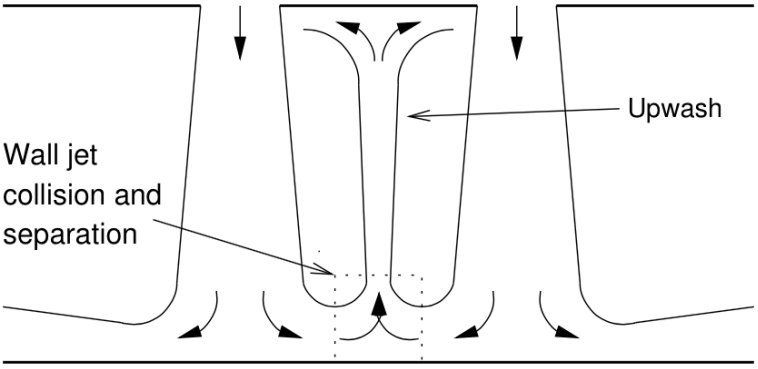

Figure 2.4: The upwash flow formed due to the collision of two wall jets [Lee and Lee, 2000]

The effect of jet-to-jet spacing or pitch also plays a very important role as discussed earlier. Prior research works have proved that for a short pitch length there is a significant interaction between the jets. At the same time, if the pitch is too large, this also affects the area averaged Nusselt number. [Huber and Viskanta, 1994] concluded from their experiments that the local heat transfer produced by a single circular impinging jet is greater than the rates produced by an individual jet in an array. Figure 2.5 shows the optimum jet to jet spacing which provides uniform heat transfer distribution on the impinging plate.

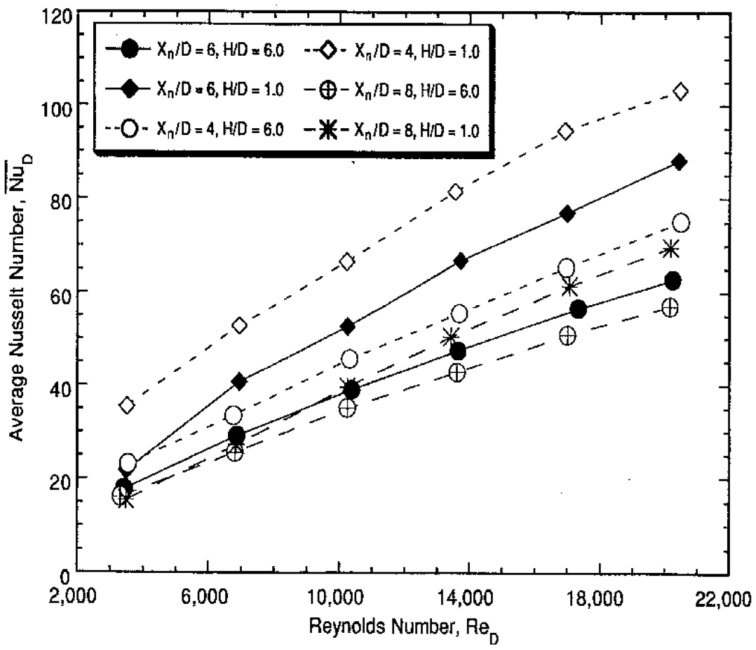

Figure 2.5: Effect of jet to jet spacing [Huber and Viskanta, 1994]

The effect of cross-flow is certainly a parameter that is quite important and plays a dominant role in affecting the heat transfer of an array of impinging jets. In general, there are three types of cross-flow schemes: minimum, intermediate and maximum cross-flow. The investigations will be further discussed in detail in the subsequent chapters. From previous work, it is found that the cross-flow lowers the heat transfer coefficients, as the spent air from the jets which are upstream in an array can sweep away the downstream jets thereby affecting the jet structure. This influence will not only affect the jet structure but also delay the impingement and sometimes, the jet is mixed in the cross-flow which is at greater velocity. The effect is more pronounced at higher nozzle-to-plate distance. Figure 2.6 shows the various schemes of the cross-flow. The first image illus-

trates for minimum cross-flow condition where the heat transfer rates are increased if the flow is minimum. All the four sides of an array are opened in this case. The second image illustrates for intermediate cross-flow where only two sides are open to exhaust the spent air and the final configuration is the maximum cross-flow configuration where the flow is designed to go only one side. If the cross-flow is maximum, the probability of impinging jets getting affected is more. In the next chapter, after an extensive study on impinging jets, a detailed explanation regarding different parameters that affect the heat transfer rates of the jet are discussed. This analysis would help the current project to narrow down the options available.

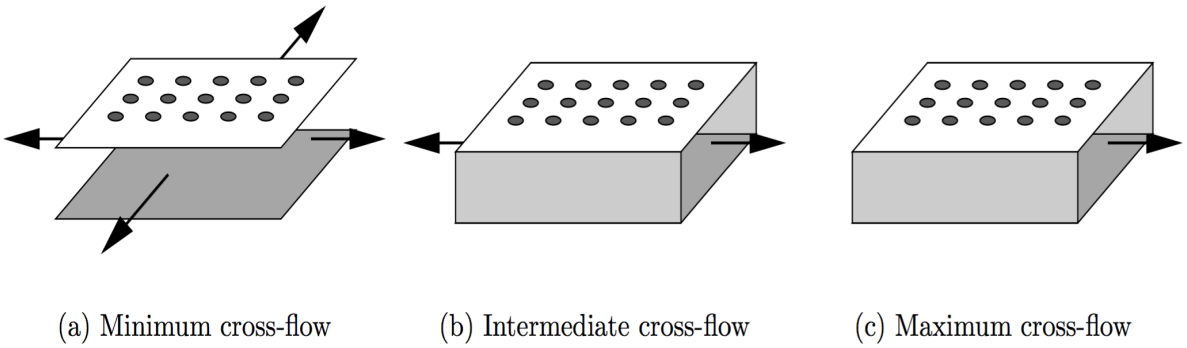

(a) Minimum cross-flow (b) Intermediate cross-flow (c) Maximum cross-flow

Figure 2.6: Different cross-flow schemes [Viskanta, 1993]

2.3. NUMERICAL MODELING

This section presents the theoretical approach required to perform the numerical simulations to model the impinging jets. It provides a brief overview on the concept of turbulence which is an important phenomenon in the multiple jet impingement system and the governing equations for heat and fluid flow.

2.3.1. TURBULENCE

In our everyday surroundings, most of the flows are turbulent. There is no perfect definition that defines the phenomenon of turbulence, but turbulent flows exhibits certain properties that helps to identify the turbulent flow. Few of the characteristic features of turbulent flow are described below [Pope, 2000]:

- Turbulent motions are often irregular, random and chaotic with high signal to noise ratio. Due to the irregular movement of turbulent scales, the structure of the flow is highly unpredictable. Therefore the movements of turbulent scales are difficult to calculate by analytical means.
- Highly dissipative: Turbulent scales dissipates the energy of the mean flow through an energy cascading process. The energy is transferred from larger eddies to the smaller eddies. The energy from this process eventually dissipates as heat or noise. A continuous supply of energy from the mean flow is necessary to maintain the turbulent flow.
- Continuum: Fluids in general are treated as continuums. Hence any disturbances in the flow affects the rest of the flow
- Turbulence is not considered as fluid property as the flow can transition from laminar to turbulent and vice-versa. Hence, turbulence is considered as a flow phenomenon.
- Turbulence is effective in mixing quantities and diffuse quantities and flow properties such as mass, momentum, heat etc. Therefore it is highly diffusive in nature.

- Turbulence is a phenomenon that occurs in three dimensional directions. As the turbulent scales are highly irregular and diffusive, they are spread in all coordinate directions.
- Turbulence occurs at high Reynolds numbers. Reynolds number is the ratio of inertial to viscous forces and when the flow surpasses this critical threshold ratio, the flow is characterized by the turbulence.

2.3.2. NEAR WALL FLOW PHYSICS

The flow close to the walls are important to understand in all fluid mechanics problems. These wall bounded flows can be associated with many phenomena like separation, transition, boundary layer development, wall shear stress etc. For jet impingement problem, it is really important to understand the near wall physics as the flow is impinged on a solid surface to obtain high heat transfer rates. The fact that the jet impingement array includes a combination of both free shear flows and wall bounded flows which makes the flow phenomenon complicated. Hence, the impinging jet flow is viewed as a good platform for testing the computational codes and tools.

In order to explain near wall flow physics, it is important to define scaled quantities. One such quantity is called friction velocity, which is defined as:

$$u_\tau = \left(\frac{\tau_w}{\rho}\right)^{\frac{1}{2}} \tag{2.5}$$

For the flow through pipes, two dimensionless quantities are required: U^+ and Y^+. The first being the velocity relative to the wall and the second being distance to the wall. The dimensionless velocity and length scale is defined as:

$$U^+ = \frac{\overline{u}}{u_\tau} \tag{2.6}$$

$$Y^+ = \frac{y.u_\tau}{\nu} \tag{2.7}$$

If Y^+ is plotted against U^+ on a logarithmic scale for any flow near the wall, the turbulent profiles characterized by the dimensional coordinates (y, u), are integrated into one profile described in non dimensional coordinates (U^+, Y^+). This profile takes the shape of a curve shown in Figure 2.7. For any turbulent flows, the near wall flow can be classified into three main regions:

1. The linear sub layer
2. The log-law region
3. The outer layer

The fluid close to the wall should satisfy the no slip condition and thus the velocity and shear stress of the flow decreases. In the absence of these stresses, the fluid close to the wall is dominated by viscous effects. This region is known as the linear sub layer and it is extremely thin ($Y^+ < 5$).Therefore, it is assumed that the shear stress is approximately equal to the wall shear stress τ_w. As there is a linear relation between U^+ and Y^+, the fluid layers adjacent to the wall is known as the linear sub-layer. Further away from the viscous sub-layer, there exists a region where the effect of viscous and turbulence plays an important role. In this region, the shear stress τ, varies slowly with the distance from the wall. This region is known as log - law region and it extends from $30 < Y^+ < 500$). Between the log-law region and the linear sub-layer, there exists a a region

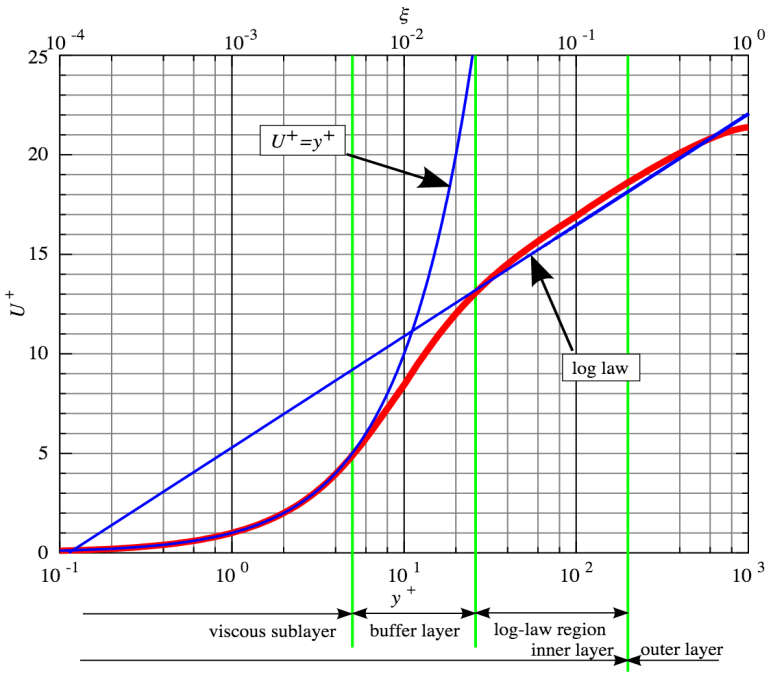

Figure 2.7: Law of the wall [Pope, 2000]

where the profile curve is neither linear not logarithmic. This region is called buffer layer. Further away from the walls of the channel, the flow becomes dominated by inertial forces and becomes turbulent. This region is called the outer layer, where the viscous forces are negligible and the distance to the wall does not dominate anymore.

2.3.3. GOVERNING EQUATIONS FOR FLUID FLOW

The equations which govern the fluid motion and its properties are derived from the conservation laws of physics. They are generally formulated as: conservation of mass, momentum and energy. These three conservation laws are frequently used to solve any fluid dynamic problem and they are often represented in integral or differential form. Before deriving these laws, the fluid is assumed to be Newtonian fluid, which adheres to all Newton laws of motion and also the fluid is incompressible. ρ (density) is constant.

$$\frac{\partial u_i}{\partial x_i} = 0 \tag{2.8}$$

If the divergence of the velocity field is equal to zero, the total mass of the system is conserved. This is known as conservation of mass or continuity equation. In the above equation 2.8 u_i is the velocity component in the x_i direction. For this equation, the Einstein summation convention for repeated indices are applied. if ρ (density) is not constant and varies with time, then the equation is represented as 2.9.

$$\frac{\partial \rho}{\partial t} + \nabla.(\rho U) = 0 \tag{2.9}$$

The law of conservation of energy is defined as:

$$\frac{\partial T}{\partial t} + u_j.\frac{\partial T}{\partial x_j} = k.\frac{\partial^2 T}{\partial x_j^2} \tag{2.10}$$

From the equation 2.10 it is shown T is the temperature of the fluid and 'a' is the thermal diffusivity of the fluid. This equation is simplified such that the momentum dissipation to the thermal energy is neglected. The term on the left hand side represents the change of thermal energy of an element with respect to time, while the second term is the heat advection term. The diffusion term of heat is on the right hand side of the equation. The source term is neglected in this equation but the additional term in equation 2.11 is called the heat flux which is similar to the Reynolds shear stress in momentum equation.

$$\frac{\partial \bar{T}}{\partial t} + \bar{u}_j . \frac{\partial \bar{T}}{\partial x_j} = a . \frac{\partial^2 \bar{T}}{\partial x_j^2} - \frac{\partial (u'_j . T')}{\partial x_j} \tag{2.11}$$

The third governing equation is the conservation of momentum which also represents the Navier - Stokes equation:

$$\frac{\partial u_i}{\partial t} + u_j . \frac{\partial u_i}{\partial x_j} = -\frac{1}{\rho} . \frac{\partial p}{\partial x_i} + \nu . \frac{\partial^2 u_i}{\partial x_j^2} + g_i \tag{2.12}$$

In the above equation 2.12 't' is the time, 'p' is the pressure in the flow. 'ν' is the kinematic viscosity of the fluid and 'g'_i is the gravity vector. The second term is the advection term and the first term is change in momentum of the fluid element with respect to time. On the right hand side of the equation, the first two terms represents the change of momentum by pressure gradients and viscous forces, while the third term is the body force in the form of gravity. The initial and boundary condition of both continuity and momentum equation describe both laminar and turbulent flows. However, for laminar flows, they have exact solutions for these equations whereas, for turbulent flows, there are no exact solutions as the flow is chaotic. The instantaneous velocity and pressure fluctuate with time and can not be predicted, so these quantities are decomposed for mean value and fluctuating component.

$$u_i = \bar{u}_i + u'_i, \tag{2.13}$$

$$p = \bar{p} + p', \tag{2.14}$$

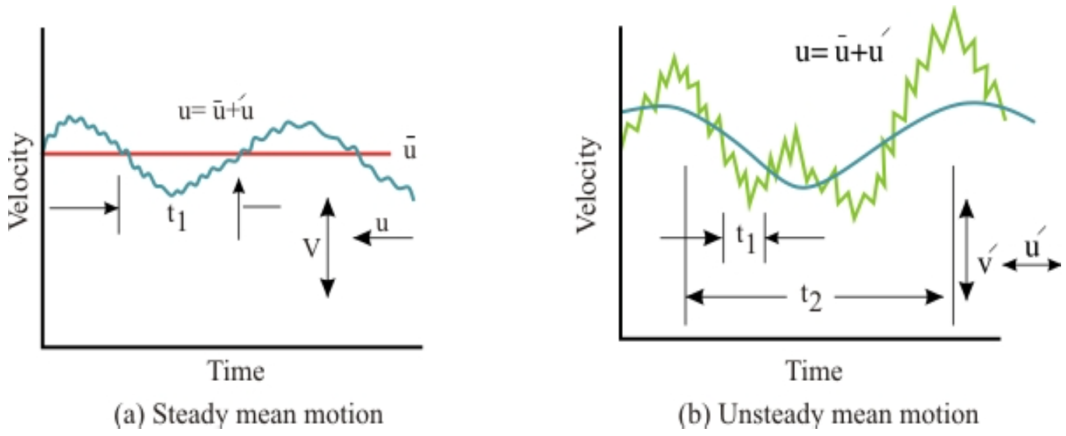

Figure 2.8: Steady and unsteady mean motions in a flow

Where the quantities with the overhead bar sign represents the ensemble mean and the quantities with prime indicates the fluctuating component. Substituting the above equations 2.13 and 2.14 in continuity and momentum equation yields the RANS equations. Figure 2.8 represents statistically steady and unsteady mean motions in a flow.

2.3.4. GOVERNING EQUATIONS FOR HEAT TRANSFER

The convective heat flux from solid boundaries to moving fluids can be described using Newton's law of cooling [Viskanta, 1993]

$$q'' = h(T_\infty - T_w) \tag{2.15}$$

Where q'' is the heat flux, h is the heat transfer coefficient, T_∞ is the bulk temperature of the fluid and T_w is the wall temperature. The difference in the temperature is the important and driving factor for convective heat transfer. Often, the experimental heat transfer coefficient and the wall temperature results are non - dimensionalized using the conductivity of the fluid λ and the length scale $\mathscr{D}$ which results in the Nusselt number.

$$Nu = \frac{h.\mathscr{D}}{k} \tag{2.16}$$

The Nusselt number is always a complex function of geometry, the velocity of the flow and the physical properties of the flow. There are several correlations between Reynolds number, Prandtl number, Nusselt number and a non- dimensional function of the geometry. The Reynolds number is defined as:

$$Re = \frac{\mathscr{U}.\mathscr{D}}{\nu} \tag{2.17}$$

where $\mathscr{U}$ is the velocity scale that characterizes the flow field. The Prandtl number is defined as:

$$Pr = \frac{\nu}{a} \tag{2.18}$$

The Reynolds and the Prandtl number appear in the energy equation which is non - dimensionalized from equation 2.19:

$$\frac{\partial T^*}{\partial t^*} + u_j^* . \frac{\partial T^*}{\partial x_j^*} = \frac{1}{Re.Pr} . \frac{\partial T^*}{\partial x_j^{*2}} . \tag{2.19}$$

The asterisk symbol indicates that all the quantities are non - dimensionalized using the bulk temperature of the fluid, so that $T^* = \mathrm{T}/T_\infty$, $t^* = t.\mathscr{U}/\mathscr{D}$, $x_j^* = x_j/\mathscr{D}$, $u_j^* = u_j/\mathscr{U}$. Also, power law is quite often used to correlate between non - dimensional quantities.

$$Nu = \alpha_1 . Re^{\alpha_2} Pr^{\alpha_3} f(geometry) \tag{2.20}$$

Where α_1, α_2 and α_3 are parameters that are dependent on the flow regime and the function 'f' is geometry dependent. This correlation gives an approximate estimation of heat transfer coefficient for a given flow geometry and this can also be used for scaling purposes but it does not give any explanation or clarification on interactions between flow and heat transfer.

2.4. EXPERIMENTAL BACKGROUND

This section presents the experimental investigations of multiple impinging jet array in laminar regime by [Rao *et al.*, 2010]. As stated earlier, most of the research in past focussed more on turbulent impinging jets whereas in the recent times, laminar jets has been gaining importance in several industrial applications. In spite of its growing applications, there is limited work with respect to laminar impinging jet array. To validate the CFD results obtained from the present study, the only available experimental investigations in the literature is performed by Rao, as all other studies are performed for single impinging jets.

The main aim of this experimental study is to determine the heat transfer and pressure drop characteristics of a multiple jet impingement array in low Reynolds number regime. The schematic of experimental setup used in the current investigations is illustrated in figure 2.9. The setup is designed in such a way that, a three stage air filtering system with two air filters and a dehumidifier is used to supply dry and clean air to the impingement system. The air is metered by using a mass flow meter. The array consists of a jet impingement plate drilled with holes in an inline pattern. The holes are arranged in inline fashion due to their ability to produce better heat transfer rates than staggered holes [Florscheutz *et al.*, 1980]. The experiments are performed for various flow configurations as shown in table 2.1.

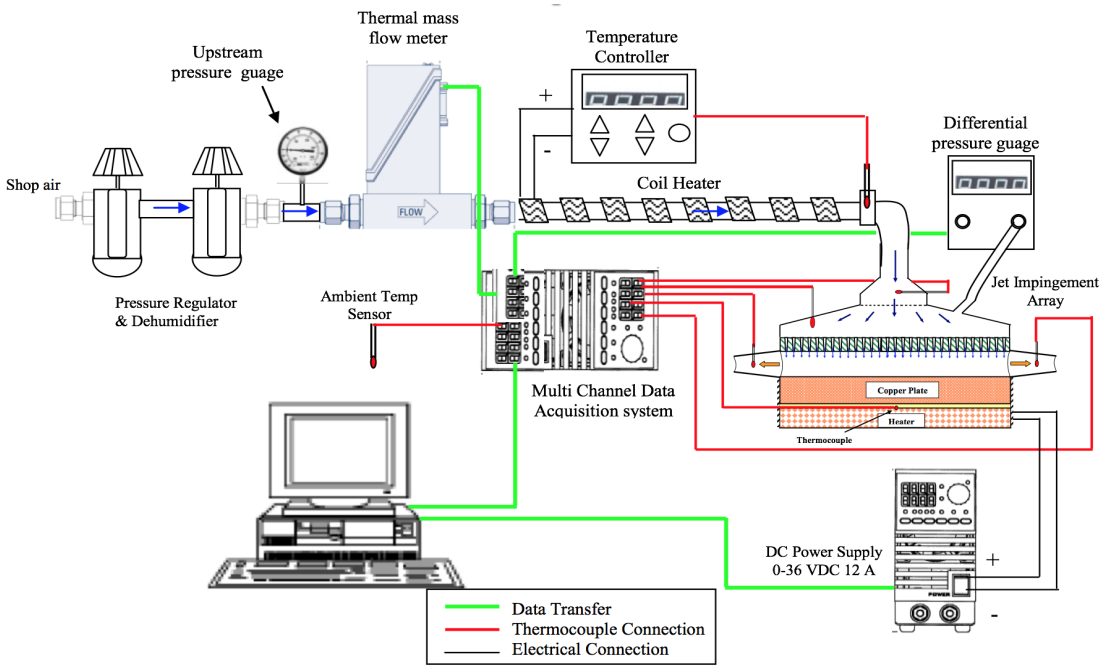

Figure 2.9: Schematic of the experimental setup [Rao *et al.*, 2010]

The streamwise jet to jet spacing (X/D) and the spanwise interjet spacing (Y/D) ratios are kept at 5 for all the simulations. The nozzle-to-plate spacing (Z/D) can be varied with the help of insulated spacers. A resistance type heater with dimensiions of 29 X 29 mm is used as heat source. A high precision DC power supply is used to monitor the power delivered to the heater. The heat density can be varied in the range of 0 - 50 KW/m^2. A copper plate is used on top of the heater to evenly distribute the heat and to remove any localization of heating. A thermal paste with a thermal conductivity of 7 W/m-K is used in between the heater and the copper plate to enhance the conduction from the source. A T- type thermocouple is used to monitor the temperature over the heater and the temperature of spent air. By changing the mass flow rate through the mass flow meter, the Reynolds number of the system can be varied. Quantities such as pressure and temperature at various location can be acquired through multichannel data acquisition system seen in figure 2.9. A schematic of the impinging system can be seen in figure 2.10. The position of thermocouples, pressure probes, impinging plate, heater, thermal paste and copper plate can be seen from the same schematic figure. The air exits from the two opposite sides as seen from the schematic diagram.

Table 2.1: List of the experiments performed by [Rao *et al.*, 2010]

D [mm]	Plate [mm^2]	Array Size	No: of Holes	X/D	Y/D	Z/D	t/D
0.2	29 X 29	29 X 29	841	5	5	5	5
0.2	29 X 29	29 X 29	841	5	5	6	5
0.2	29 X 29	29 X 29	841	5	5	8	5
0.4	29 X 29	15 X 15	225	5	5	2.5	5
0.4	29 X 29	15 X 15	225	5	5	5	5
0.4	29 X 29	15 X 15	225	5	5	7.5	5
0.4	29 X 29	15 X 15	225	5	5	2.5	7.5
0.4	29 X 29	15 X 15	225	5	5	5	7.5
0.4	29 X 29	15 X 15	225	5	5	7.5	7.5
0.6	29 X 29	10 X 10	100	5	5	2.5	3.3
0.6	29 X 29	10 X 10	100	5	5	5	3.3
0.6	29 X 29	10 X 10	100	5	5	7.5	3.3
0.8	29 X 29	8 X 8	64	5	5	2.5	2.5
0.8	29 X 29	8 X 8	64	5	5	5	2.5
0.8	29 X 29	8 X 8	64	5	5	7.5	2.5

Furthermore, to reduce heat transfer to the surroundings, the heater is insulated from the bottom and the all the adjacent sides. The exhaust air from the impingement system is collected in a duct on both the sides to measure the temperature of the spent air in order to estimate the total heat absorbed by the air. The direction along the channel through which the air exits the array is termed as streamwise direction and the direction along the width of the channel is spanwise direction. The flow is restricted in the spanwise direction and therefore the spent air has to leave the system through streamwise direction as shown in the schematic of jet impingement system.

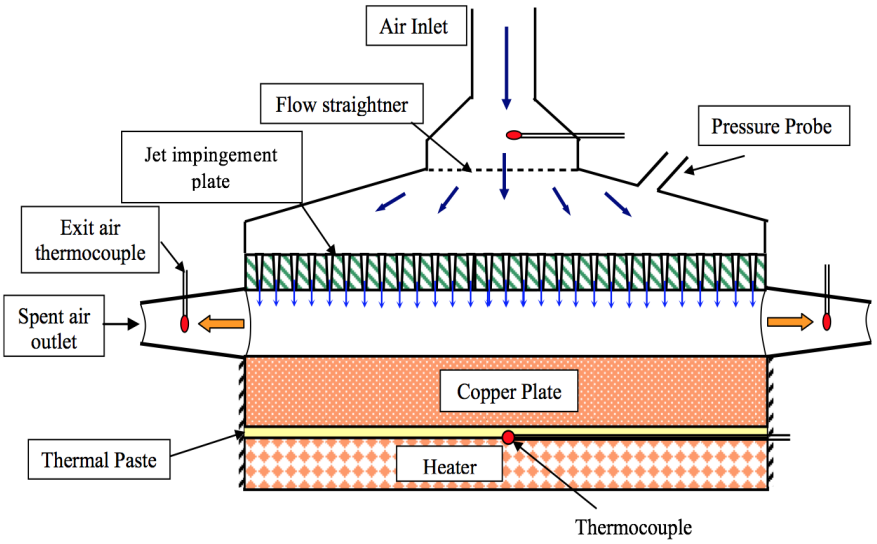

Figure 2.10: Schematic of the jet impingement system [Rao *et al.*, 2010]

3

STEADY AND UNSTEADY REYNOLDS AVERAGED NAVIER - STOKES SIMULAITONS

This chapter presents an overview on the computational methodology employed in steady and unsteady RANS approach. In section 3.1, a hypothesis of eddy viscosity models used in this research are discussed. Section 3.2 presents with a detailed overview on the RANS methodology employed in the current study, to model the impinging jet array in low Reynolds number region. This section also discusses about the computational geometry, discretization of mesh, boundary conditions, solution procedure and the test results. In section 3.3, the unsteady RANS (URANS) approach has been discussed for the same impinging jet array to determine the flow and heat transfer characteristics of the jet impingement system.

3.1. REYNOLDS AVERAGED NAVIER-STOKES (RANS) APPROACH

This section presents a detailed analysis on Reynolds-averaged Navier - Stokes (RANS) equations. In this section, the main focus is to model the eddy-viscosity models which are designed to treat the near wall regions in the flow domain. Direct numerical solution of Navier - Stokes equation provides full solutions for newtonian fluids in both laminar and turbulent regions. In RANS approach, the Navier - Stokes equations are obtained by modeling the Reynolds stress term which is the effect of turbulence. Hence the equations are averaged and closed to obtain the solution. However, the Reynolds stress cannot be solved from the mean velocity and hence it has to be modeled using several approaches. One way of solving is through eddy-viscosity model and therefore the eddy-viscosity models are used in performing the RANS simulations. As an assumption, the Reynolds stress is proportional to the strain rate of mean flow and the proportionality coefficient is derived from length scale and velocity scale $\mathscr{L}$ and $\mathscr{U}$. The RANS approach is based on decomposition of average and fluctuating components which leads to equation 3.1.

$$U(x,t) = \overline{U}(x,t) + u'(x,t), \tag{3.1}$$

Where $\bar{U}(x,t)$ is time (temporal) averaged which is also called mean part and $u'(x,t)$ is the fluctuations part. The mean part is defined by the integral:

$$\overline{U}(x,t) = \frac{1}{\delta t}\int_{t}^{t+\delta t} U(x,t)\,dt, \tag{3.2}$$

In the above equation 3.2, δt is the time interval which is huge compared to the fluctuation period. As

discussed earlier, by taking the mean of both continuity and momentum equations 2.8 and 2.12 the Reynolds averaged continuity and Reynolds averaged Navier-Stokes equations are obtained.

$$\frac{\partial \overline{U}_i}{\partial x_i} = 0 \tag{3.3}$$

$$\frac{\partial \overline{U}_i}{\partial t} + \frac{\partial \overline{U_i U_j}}{\partial x_j} = \nu . \frac{\partial^2 \overline{U}_i}{\partial x_i . x_j} - \frac{1}{\rho} \frac{\partial \overline{p}}{\partial x_j} \tag{3.4}$$

Substituting the Reynolds decomposition for $U_i and U_j$, the non-linear term will become:

$$\overline{U_i U_j} = \overline{U}_i . \overline{U}_j - \overline{u_i u_j}, \tag{3.5}$$

In the above equation 3.5 the stress tensor is called the Reynolds stress and if the solution needs to be closed this term has to be modeled and the equation becomes:

$$\frac{\overline{D} U_i}{\overline{D} t} = \nu . \frac{\partial^2 \overline{U}_i}{\partial x_i . x_j} - \frac{1}{\rho} \frac{\partial \overline{p}}{\partial x_j} - \frac{\partial \overline{u_i . u_j}}{\partial x_j} \tag{3.6}$$

Where $\frac{\overline{D} U_i}{\overline{D} t}$ is the averaged substantial derivative defined as:

$$\frac{\overline{D} U_i}{\overline{D} t} = \frac{\partial}{\partial t} + \overline{U} . \nabla . \tag{3.7}$$

This equation 3.7 is similar to momentum equation other than the additional term which is called Reynolds stress term. This term represents the effect of turbulence in the momentum transport.Similarly, with the relation of stress-strain for laminar flows, the analogy for newtonian fluids becomes:

$$\frac{-(\tau_{ij} + P\delta_{ij})}{\rho} = -2\nu S_{ij}, \tag{3.8}$$

Boussinesq proposed a similar theory for turbulent stress tensor with the proportionality coefficient called "turbulent viscosity":

$$\overline{u_i u_j} - \frac{2}{3} k \delta_{ij} = -\nu_t \left(\frac{\partial \overline{U}_i}{\partial x_j} + \frac{\partial \overline{U}_j}{\partial x_i} \right), \tag{3.9}$$

In the above equation 3.9 the reynolds stress term is decomposed to isotropic and anisotropic parts. The second term on the left hand side is called the isotropic part and on the right hand side, is the anisotropic part. The anisotropic part represents the dissipation rate and the isotropic part is the production of turbulent kinetic energy. In the above equation δ_{ij} is the kronecker delta function and ν_t is the eddy viscosity. This hypothesis is known as Boussinesq hypothesis. The eddy viscosity models try to model these equations to solve for Reynolds stress. Table 3.1 provides an overview of eddy-viscosity models.

Table 3.1: Overview of eddy-viscosity turbulence models based on the number of equations

No: of equations	Models
0	Mixing length model (zero equation model)
1	Spalart-Almaras model Prandtl one equation model
2	standard $k-\epsilon$ model Re-Normalisation Group $k-\epsilon$ model $k-\omega$ model Realizable $k-\omega$ model k-l model
7	Reynolds stress model

3.1.1. THE $k-\epsilon$ METHOD

In standard $k-\epsilon$ model, we generally solve for two turbulence quantities which represents two transport equations. One quantity being the kinetic energy 'k' and the other one being 'ϵ' which is dissipation rate. These quantities are important because of energy cascading mechanism [Pope, 2000]. Using these quantities, the characteristic length scale $\mathscr{L} = k^{3/2}/\epsilon$ and characteristic time scale $\mathscr{T} = k/\epsilon$ can be determined. From these two quantities, the dimensional turbulent kinematic viscosity is calculated.

$$\nu_t = C_\mu f_\mu k^2/\epsilon, \tag{3.10}$$

Where f_μ is the damping function which reduces the value of eddy-viscosity in the near wall region so that it accounts for the non-viscous and viscous effects. C_μ is one of the five model constants. The turbulent kinetic energy and dissipation rate is expressed as:

$$k = \frac{\overline{u}_1'^2 + \overline{u}_2'^2 + \overline{u}_3'^2}{2}, \tag{3.11}$$

$$\epsilon = \nu \overline{\left(\frac{\partial \bar{u}_i}{\partial x_j} + \frac{\partial \bar{u}_j}{\partial x_i}\right)}, \tag{3.12}$$

There are quite different number of low-Reynolds $k-\epsilon$ models. However, the model defined in [Abe *et al.*, 1994] was chosen. The equations are:

$$\frac{Dk}{Dt} = P_k - \epsilon + \nabla.\left(\nabla k.(\nu + \frac{\nu_t}{\sigma_k})\right), \tag{3.13}$$

$$\frac{D\epsilon}{Dt} = P_k C_{\epsilon 1}\frac{\epsilon}{k} - C_{\epsilon 2}\frac{\epsilon^2}{k} f_2 + \nabla.\left(\nabla \epsilon(\nu + \frac{\nu_t}{\sigma_\epsilon})\right), \tag{3.14}$$

In the above equations 3.13 and 3.14, $P_k = 2.\nu_t.S_{ij}.S_{ij}$ is the production of kinetic energy, f_2 is the damping factor and $\sigma_\epsilon and \sigma_k$ are model coefficients. The model coefficients are:

Some of the advantages of $k-\epsilon$ model are its relatively simple implementation and numerically stable calculations. It is also a model which is widely validated. The disadvantages of this model are that it poorly

Table 3.2: Model coefficients for $k-\epsilon$ model

Model constants	Value
C_μ	0.09
$C_{\epsilon 1}$	1.44
$C_{\epsilon 2}$	1.92
σ_k	1.3
σ_ϵ	1.0

predicts swirling and rotating flows, flows with strong separation, unconfined flows and fully developed flows in non-circular ducts. It is valid only for fully developed turbulent flows and performs poorly in prediction transitional and developing flows. Although it is sufficiently accurate for simple flow problems, it is quite inaccurate when it comes to complex flow patterns owing to the turbulent viscosity hypothesis and the inaccuracy of the ϵ equation. However, the accuracy of the model, depending upon the flow problem, can be improved by adjusting the model constants. The standard $k-\epsilon$ model assumes stable conditions and the constants represented in the table 3.2 are calculated for such stable conditions. However, in the case of separating flows, the equilibrium between production and dissipation of turbulence is not well maintained.

3.1.2. SST $k-\omega$ METHOD

The shear stress transport (SST) $k-\omega$ model is a two equation model which is a combination of both $k-\epsilon$ and $k-\omega$ models. It was Menter in 1994 who proposed this model and initially this model had strong sensitivity under strong pressure gradients. In 2003, the model was re-proposed with several changes. It uses the $k-\epsilon$ formulation in the free stream region that is outside the boundary layer and uses the $k-\omega$ formulation inside the boundary layer. This combines the best of two worlds and avoids the $k-\omega$ problem of being too sensitive to the inlet free-stream turbulence properties and the $k-\epsilon$ problem of inability to simulate the turbulent kinetic energy in the near wall region especially in the viscous sub layer. It behaves well in adverse pressure gradients and separating flows. Also, it can be used as a low Reynolds number turbulence model without any extra damping functions. However, it produces excessive turbulence in the regions with normal strain. These regions include stagnation regions and strong acceleration regions.

$$\frac{\partial(\rho k)}{\partial t}+\frac{\partial(\rho u_j k)}{\partial x_j}=P-\beta^*\rho\omega k+\frac{\partial}{\partial x_j}\left[\frac{\partial k}{\partial x_j}(\mu+\sigma_k\mu_t)\right], \tag{3.15}$$

$$\frac{\partial(\rho\omega)}{\partial t}+\frac{\partial(\rho u_j\omega)}{\partial x_j}=\frac{\alpha}{\nu_t}P-\beta^*\rho\omega^2+\frac{\partial}{\partial x_j}\left[\frac{\partial\omega}{\partial x_j}(\mu+\sigma_\omega\mu_t)\right]+2(1-F1)\frac{\rho\sigma_{\omega 2}}{\omega}\frac{\partial k}{\partial x_j}\frac{\partial\omega}{\partial x_j}, \tag{3.16}$$

and the turbulent eddy viscosity μ_t and production P are given by:

$$\mu_t=\frac{\rho a_1 k}{max(a_1\omega,\Omega F_2)} \tag{3.17}$$

$$P=\left[\mu_t\left(2S_{ij}-\frac{2}{3}\frac{\partial u_k}{\partial x_k}\delta_{ij}\right)-\frac{2}{3}\rho k\delta_{ij}\right]\frac{\partial u_i}{\partial x_j} \tag{3.18}$$

$$S_{ij}=\frac{1}{2}\left(\frac{\partial u_i}{\partial x_j}+\frac{\partial u_j}{\partial x_i}\right), \tag{3.19}$$

The function F_2 and another function F_1 are blending functions. The parameter α in the ω equation is expressed as,

$$\alpha = F_1\alpha_1 + (1 - F_1)\alpha_2, \tag{3.20}$$

α_1 and α_2 are constants and other functions are given by:

$$F_1 = tanh(arg_1^4) \tag{3.21}$$

$$F_2 = tanh(arg_2^2) \tag{3.22}$$

$$arg_1 = min\left[max\left(\frac{\sqrt{k}}{\beta^*\omega d}, \frac{500^\mu/\rho}{d^2\omega}\right), \frac{4\rho\sigma_{\omega 2}k}{CD_{k\omega}d^2}\right] \tag{3.23}$$

$$arg_2 = max\left(2\frac{\sqrt{k}}{\beta^*\omega d}, \frac{500^\mu/\rho}{d^2\omega}\right), \tag{3.24}$$

$$\Omega = \sqrt{2.\Omega_{ij}.\Omega_{ij}} \tag{3.25}$$

Where Ω_{ij} is defined as :

$$\Omega_{ij} = \frac{1}{2}\left(\frac{\partial u_i}{\partial x_j} - \frac{\partial u_j}{\partial x_i}\right), \tag{3.26}$$

The constants in these equations are given by,

Table 3.3: Model coefficients for SST $k-\omega$ model

Model constants	**Value**
σ_{k1}	0.85
σ_{k2}	1.0
$\sigma_{\omega 1}$	0.5
$\sigma_{\omega 2}$	0.856
β_1	0.075
β_2	0.0828
β^*	0.0828
k	0.41
a_1	0.31

The SST model puts a limitation on the shear stress when under adverse pressure gradients. It accounts for the turbulent shear stress transport and predicts accurately the onset and extent of separation. Also, since it is highly dependent on the wall distance, it poorly predicts free shear flows. In the literature, the state-of-the-art turbulence models that are commonly used for modeling the impingement flow are the two-equation

model such as standard $k-\epsilon$ model, RNG $k-\epsilon$ model, standard $k-\omega$ model, SST model and Reynolds stress model. The turbulence models with their advantages and disadvantages are listed in table 3.4.

Table 3.4: Overview of advantages and disadvantages of eddy-viscosity turbulence models

Model	**Advantages**	**Disadvantages**
Standard $k-\epsilon$	• Simple implementation	• Requires wall functions
	• Computationally in-expensive	• Viscous layer instabilities
	• Performs better in the mean flow	• Poorly predicts flows with streamline curvatures
	• Widely applied	• Inaccurate prediction of Reynolds stress anisotropies
Wilcox $k-\omega$	• Improved predictions for free shear flows and low-Re flows	• Predicts early transition in transitional flows
	• Valid for complex boundary layer flows with strong pressure gradients	• Requires high mesh resolution near the wall
	• High performance for wall bounded flows	• In flows with separation, the separation is early predicted
SST Model	• It is a combination of $k-\epsilon$ and $k-\omega$ models	• Does not include compressibility
	• Applies a limit on the shear stress in the occurrence of large pressure gradients	• Predicts inaccurately if the strain rate of the flow is changed suddenly
	• Accurately predicts the onset and extent of flow separation under adverse pressure gradients	• Shares some disadvantages of $k-\epsilon$ and $k-\omega$ models
Reynolds Stress model	• Physically, the most complete model	• High computation costs
	• Resolves the Reynolds stress anisotropies	• Momentum and turbulence equations are tightly coupled
	• Initial and final boundary conditions are required	• Implementation is highly complex
	• Capable of predicting swirling flows, flows with separation and flows in turbomachinery	• Modeling of ϵ is a problem for some type of problems.

From the advantages and disadvantages, an approximate trade-off table can be created for the turbulence models to model the impingement flow. The primary requirement of a turbulence model is to model a physically representative impinging flow in a multiple jet array. The model should be computationally stable, feasible and relatively simple to implement. The choice of the model is highly dependent on the level of accuracy that is required to model the flow. Therefore, a detailed analysis is performed to model the jet impingement flow with two different types of eddy-viscosity models based on their advantages and disadvantages. Furthermore, as the jet array is operating in laminar regime, a laminar model is also used to investigate the jet impingement flow.

3.2. NUMERICAL SIMULATIONS USING RANS

A detailed analysis on the Reynolds-averaged Navier - Stokes (RANS) simulations performed to model the impinging jet array is presented in this section. The problem set uses eddy viscosity type of turbulence model to treat the near wall regions and in this case, two types of turbulence models such as $k-\epsilon$ model, SST model and a laminar model is used to analyze the capabilities of turbulence models in predicting the heat transfer and pressure drop characteristics of jet impingement array. These turbulence models replaces the Navier - Stokes equations by averaging the quantities which reduce the time for calculation, but still possess the ability to predict the effect of turbulence. The advantage of $k-\omega$ model over the standard classical $k-\epsilon$ model is due to their improved performance at the wall and can withstand high pressure gradients in the boundary layers which makes it to stand out of all other two equation models. However, in the free-stream the ω values become very sensitive due to the inlet boundary conditions. So, to compensate these disadvantages, a new model was proposed by implementing few additional corrections to the standard $k-\omega$ model and the new model is termed as SST model. The three types of corrections are: correction to the sensitivity in the free stream or inlet conditions, a correction to the shear flow and a low Reynolds number correction for low Reynolds number flows and transitional flows. For these flows, there is no need to incorporate any damping functions. In the present study, CFD simulations were performed with three types of RANS models and the results obtained from the CFD simulations are validated with the experimental results to predict the flow characteristics of the jet impingement system.

3.2.1. GEOMETRY AND BOUNDARY CONDITIONS

The three dimensional model of jet impingement system is a complex array and requires high computation power. The array consists of 15 X 15 holes arranged in inline fashion. So, a streamline array is considered by applying symmetry conditions to the geometry. The computational domain of this array can be simplified into a single streamline array containing 7.5 jets. A schematic of jet impingement plate can be seen in figure 3.1. The diameter of the nozzles is set as 0.4mm because, from the experiments of [Rao *et al.*, 2009], it was found out that the jets with 0.4 mm diameter produces high heat transfer rates. The jet-to-jet spacing (X/D) and nozzle-to-plate spacing (Z/D) is kept as 5 diameters each. Simulations were conducted for a range of Reynolds numbers in laminar regime ranging from 400 - 2000. The impinging plate is made of copper and a constant heat flux is supplied to the target plate. The air enters from the inlet, flows through all nozzles and impinges on the heated target plate. After the impingement, the fluid forms a wall jet and leaves the domain through the outlet. "Velocity- Inlet" is used as the boundary condition for inlet, while "Pressure-Outlet" is used as the outlet boundary condition. For the walls on sides and at the center, "Symmetry" boundary condition has been used to discretize the array of 225 holes into a single row of 7.5 jets. Simulations were carried out using ANSYS Fluent which uses finite volume method and the convergence tolerance of 0.001 was set to carry on the simulations. Figure 3.2 represents the geometry of the flow in an array.

3.2.2. GRID AND SOLUTION PROCEDURE

Computational grids for the CFD analysis are generated with ANSYS meshing tool. Structured grid with hexahedral elements are used for all RANS simulations. The grid is constructed to be very dense to capture the flow features inside the array. A sensitivity analysis was performed with different grid sizes from half million to three million cells to check the grid independence of the simulation. It was found that for grid sizes between half a million to three million elements, the results deviate less than 2% from the average value. Therefore, the mesh used for the simulations consists of 1.5 million elements. The Y^+ values are found to be well within the viscous sub-layer region. For estimating the numerical stability of each simulation, various surface and point monitors such as average plate temperature, total pressure at the inlet and outlet and local point temperatures at the stagnation region of the each jet were monitored for all the simulations.The individual grids that were used to perform the sensitivity analysis had the following mesh resolution.

- 500,000 elements (referred as 0.5 Mn)

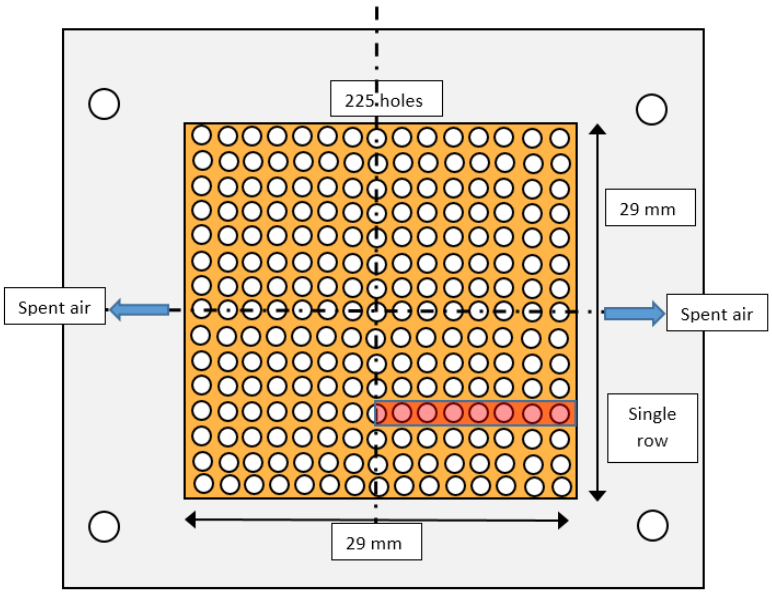

Figure 3.1: Jet impingement array for RANS simulations

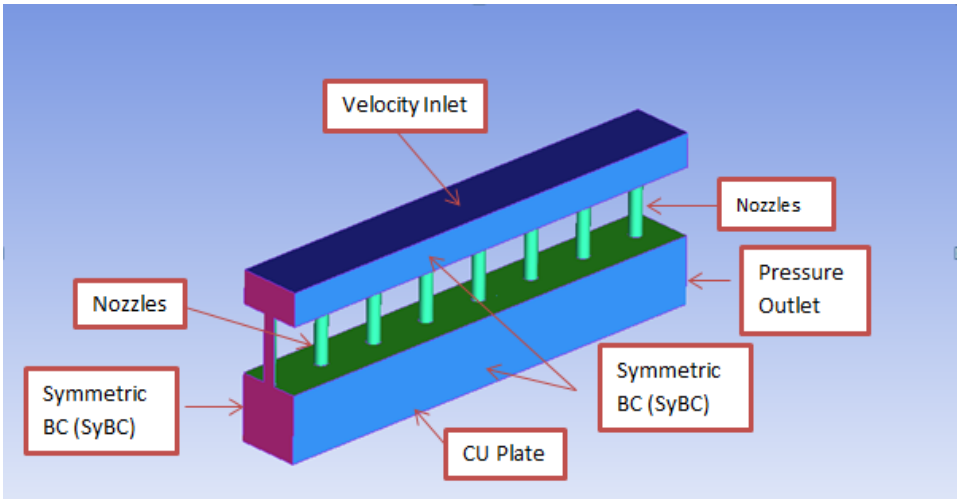

Figure 3.2: Jet impingement array for RANS simulations

- 1,000,000 elements (referred as 1 Mn)
- 2,000,000 elements (referred as 2 Mn)
- 3,000,000 elements (referred as 3 Mn)

The 3D simulations were performed on the same geometry with two different turbulence models and a laminar model. Table 3.5 shows the specifications of various simulations performed through RANS approach.

Table 3.5: Setup specifications for 3D RANS simulations

Simulation type	**Laminar model**	**$k-\epsilon$ model**	**SST $k-\omega$ model**
Mesh type	Quad/Hex	Quad/Hex	Quad/Hex
No: of elements	1.5 Mn	1.5 Mn	1.5 Mn
Convergence criteria	10^{-3}	10^{-3}	10^{-3}
Total physical simulation run-time	< 3h	< 3h	< 3h
Solver Algorithm	SIMPLE	SIMPLE	SIMPLE
Numerical scheme - momentum	Second order upwind	Second order upwind	Second order upwind
Numerical scheme - pressure	Second order	Second order	Second order

3.2.3. RESULTS

As discussed earlier, predicting flow within a jet impingement system is a complex phenomenon due to the occurrence of various flow interactions inside the array. Hence, it becomes a challenging task for the turbulence models to determine the flow physics as they are formulated for wall bounding flows. The results obtained from CFD simulations are validated with the experimental data of [Rao *et al.*, 2010] to determine the heat transfer characteristics and the behavior of laminar impinging jets in an array. Various turbulence models such as $k-\epsilon$, SST $k-\omega$ and laminar models are tested. It was found that the SST $k-\omega$ model predicted the heat transfer characteristics better than the other turbulence models. Figure 3.3 shows the comparison of the average Nusselt number from CFD simulations and experiments at various Reynolds number for arrays containing 0.4 mm jets.

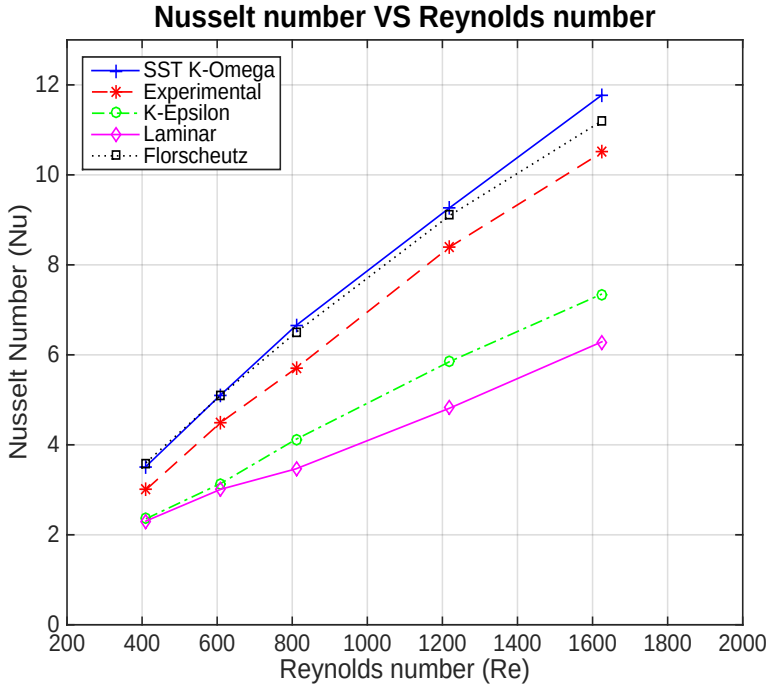

Figure 3.3: Comparison of different steady state RANS models – Variation of average Nusselt number with Reynolds number

The main objective to select 0.4 mm nozzle diameter is due to the fact that, from experimental results it was observed that 0.4 mm nozzles produce higher heat transfer coefficients than the other jet diameters. It was understood that 0.2 mm jets generate higher cross flow rates from the upstream jets due to the increase in

number of jets for a given area. Therefore, in 0.2 mm jet array, the cross flow in the channel has a significant effect on average heat transfer coefficient of the target plate. For 0.6 mm and 0.8 mm jet diameters, the heat transfer coefficients on the impinging plate results in a non uniform distribution of Nusselt numbers. Therefore, simulations were performed for 0.4 mm jet array due to their uniform heat transfer distribution. From the figure 3.3 it can be inferred that the results obtained from SST $k-\omega$ model simulations over predicts the average heat transfer coefficient by around 15%. while, the results from $k-\epsilon$ and laminar models are significantly under predicted. This under prediction might be due to the inaccurate prediction of turbulent kinetic energy in the nozzles and in core region due to the complex streamline curvatures near the stagnation region. These inaccuracies could be due to the improper distribution of dissipation and diffusion rates of turbulent kinetic energy in the standard $k-\epsilon$ model. It was also observed that, the results from SST $k-\omega$ model are in good agreement with the correlations of [Florscheutz *et al.*, 1981].

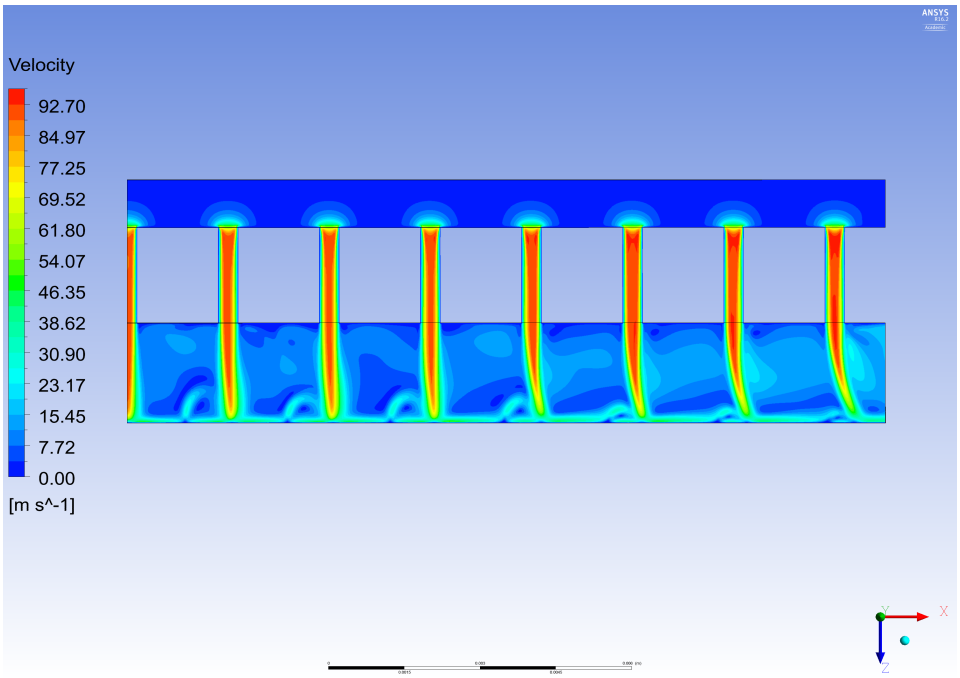

Figure 3.4: Velocity profile within the 0.4 mm jet diameter array

Figure 3.4 shows the velocity field contour map in the streamwise direction. From the contour map it can be seen that the velocity distribution from the first jet to the last jet changes significantly. This behavior is attributed to the cross flow effects. Cross flow in an array is defined as the spent air from the jets that flows along the streamwise direction in the channel. As there is no cross flow for the first jet, the jet impinges on the plate without shifting its actual stagnation point ,but the jets which are located further downstream, the impingement region is shifted from the actual region due to the increased effect of cross flow from the upstream jets. This effect can be identified in the figure 3.4 that, the last three jets suffers maximum cross flow effects from the upstream jets. It was observed that there is an increase in the cross-flow velocity from the first jet to the last jet as expected, but due to this increase in cross flow velocity,the pressure distribution in the array becomes non-uniform. The static pressure contour from the the simulations is shown in figure 3.5.

From the static pressure contour, it can be observed that, due to the increase in downstream jet velocities, the pressure gradients from the nozzles are extended towards the outlet. The effect of cross flow is also coupled to this phenomenon because, the spent air forces the pressure gradients towards the exit. Furthermore, the increase in static pressure at the stagnation point is also noticed in the pressure map as expected. Due to the contraction effect at the jet inlet, the variation of pressure in the nozzles is seen. Comparison of pressure drop results show that none of the three models were able to predict the pressure drop characteristics accurately. The values obtained from the CFD simulations are significantly higher than the experimental results. The results shows that, SST $k-\omega$ model predicted better than $k-\epsilon$ and laminar models due to its ability to perform better in the regions where pressure gradients are high. The deviation of CFD results with experi-

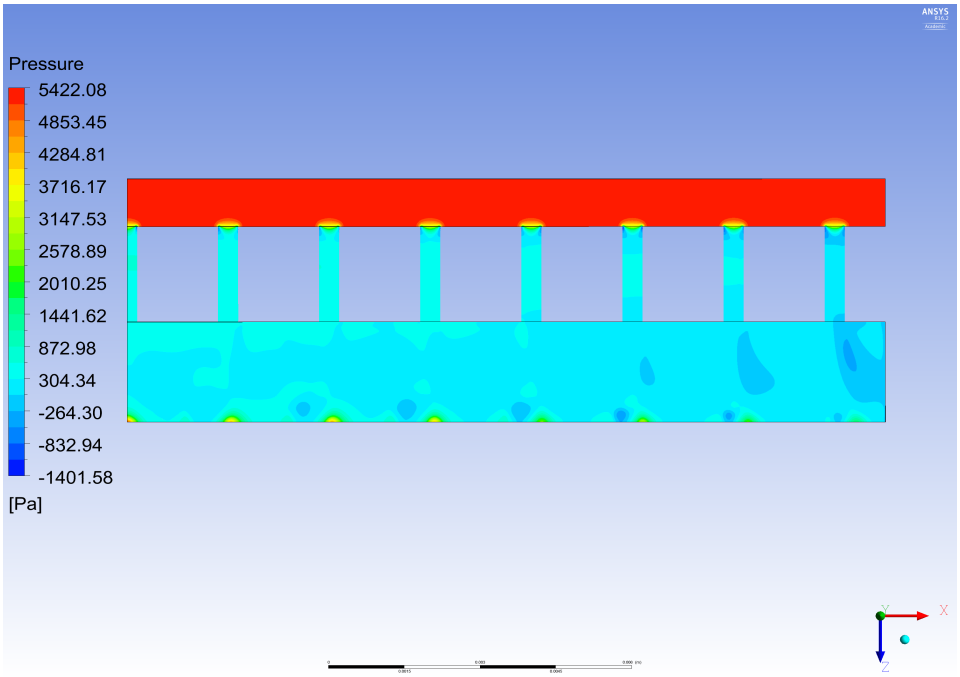

Figure 3.5: Static pressure map within the 0.4 mm jet diameter array

mental data is about 50 % and this difference increases with increase in Reynolds number as shown in figure 3.6.

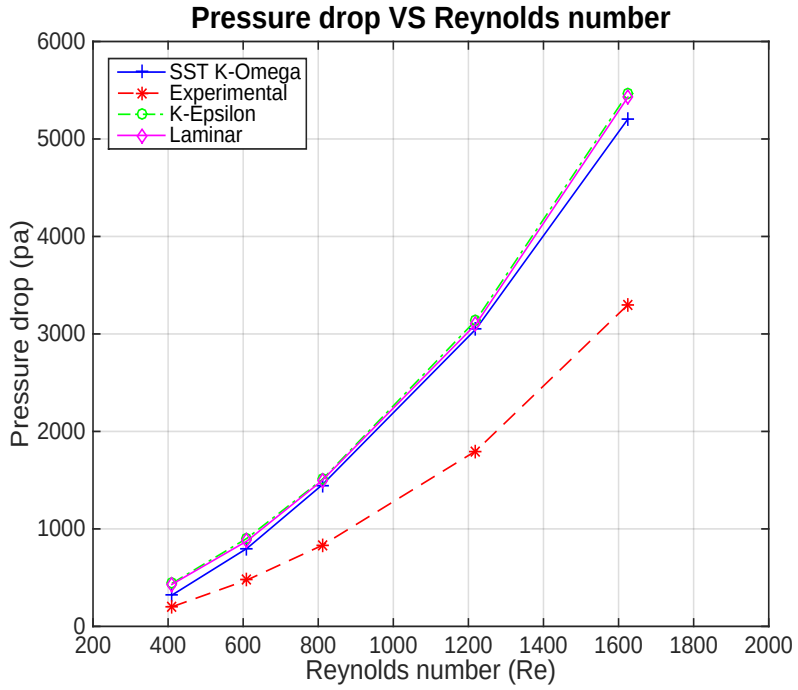

Figure 3.6: Comparison of different steady state RANS models – Variation of total pressure drop with Reynolds number

The total pressure distribution in the jet impinging array is shown in figure 3.7. It can be seen that the pressure drop in the potential core of the jet is negligible but when the potential core starts to disappear, the axial momentum and the normal stresses are converted to static pressure at the impinging region due to the loss of kinetic energy. This negative production of turbulent kinetic energy in the stagnation region was also

confirmed by many experimental and numerical studies in the past.

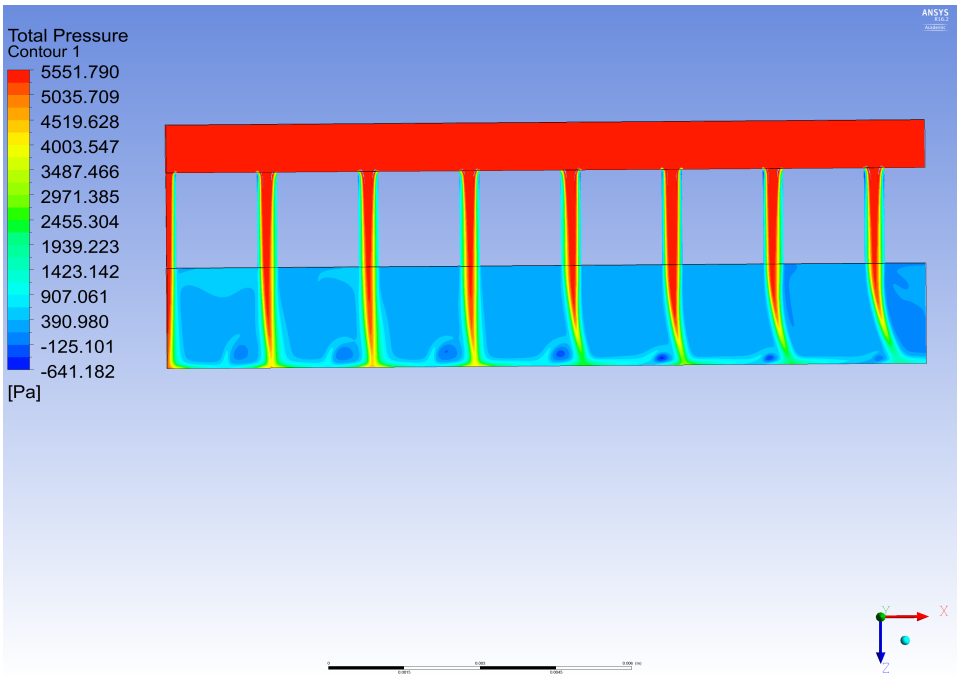

Figure 3.7: Total pressure map within the 0.4 mm jet diameter array

The production of the turbulent kinetic energy in the nozzles and jet shear layer is shown in figure 3.8. The increase in the turbulent kinetic energy in the shear layer region is caused due to the continuous acceleration and deceleration of the flow with high shear. The turbulent kinetic energy in the shear layer reaches its maximum around $Z/D = 3$. The interactions between the primary vortex created by the upwash flow and the upstream branch of the jet results in higher turbulence levels. This can be clearly seen from the contour. It is also observed that the production of kinetic energy starts inside the nozzles. The possible difference between laminar model and $k-\omega$ model is that the laminar model failed to predict the turbulence inside the nozzle, there by under predicting the heat transfer characteristics.

The temperature profile of the jets within the array is shown in figure 3.9. It is observed that only a thin layer of fluid is responsible for the actual heat transfer process while, most of the fluid remains at a temperature with which it was impinged on to the the surface. It is also observed that there is an increase in the wall jet temperature and there is a development of the thermal boundary layer close to the upwash flow.

The temperature distribution on the impinging plate is shown in figure 3.10. The temperature profile determines the local Nusselt number which is a measure of heat transfer coefficient. The temperature is lowest in the impinging region which implies high local heat transfer coefficients. For the first few jets, the profile resembles a circular shape similar to the single jet but, further downstream due to the cross flow effects, the effectiveness of the impinging jets gradually reduces. Also, it can be seen that the impinging region is shifted further downstream due to the increase in the velocity of spent air. A better insight on the local heat transfer in the array can be achieved by analyzing the variation of Nusselt number on the impinging plate. Figure 3.11 represents the variation of local Nusselts number in the stagnation region for each jet. It is observed that the Nusselt number variation is not monotonic along the channel. The highest local Nusselt number occurs for the 3rd jet after which it decreases towards the downstream of the channel. This phenomenon can be attributed to the cross flow effect. However, from the experiments of [Goldstein and Behbahani, 1982], it was determined that some amount of cross flow will enhance the heat transfer rates by convecting heat along the channel, but if the cross flow velocity increases further, then the cross flow deteriorates the heat transfer rates. From the present simulations, it is believed that, the spent air from the first two jets contributes for enhancing the heat transfer of the third jet but further downstream, the spent air from upstream jets becomes dominant which affects the heat transfer rates of the last few jets in spite of their increased jet velocity. Since the stream-

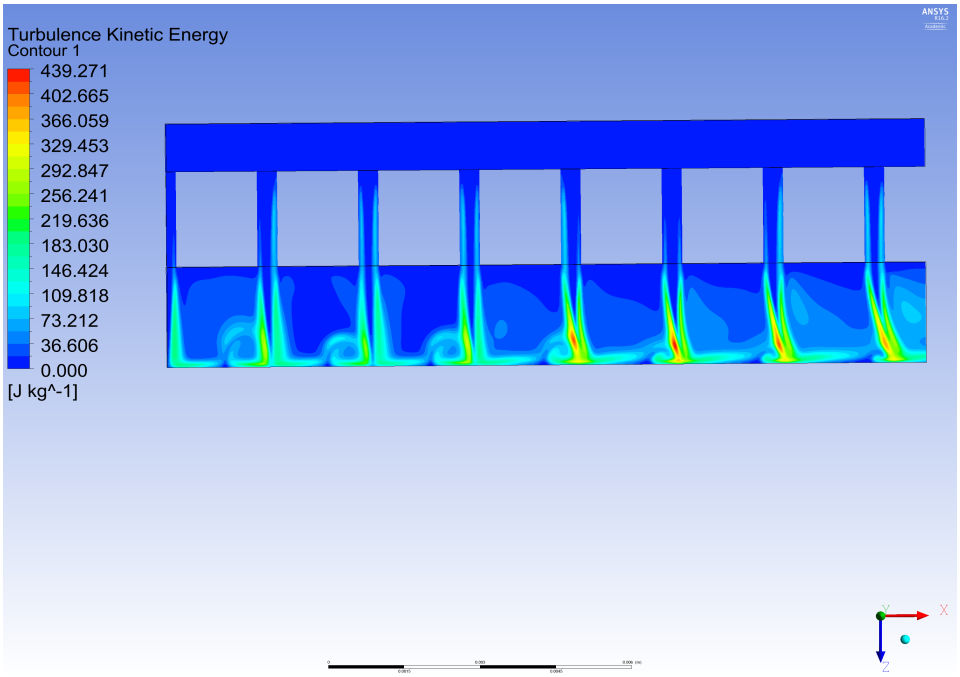

Figure 3.8: Turbulent kinetic energy profile within the 0.4 mm jet diameter array

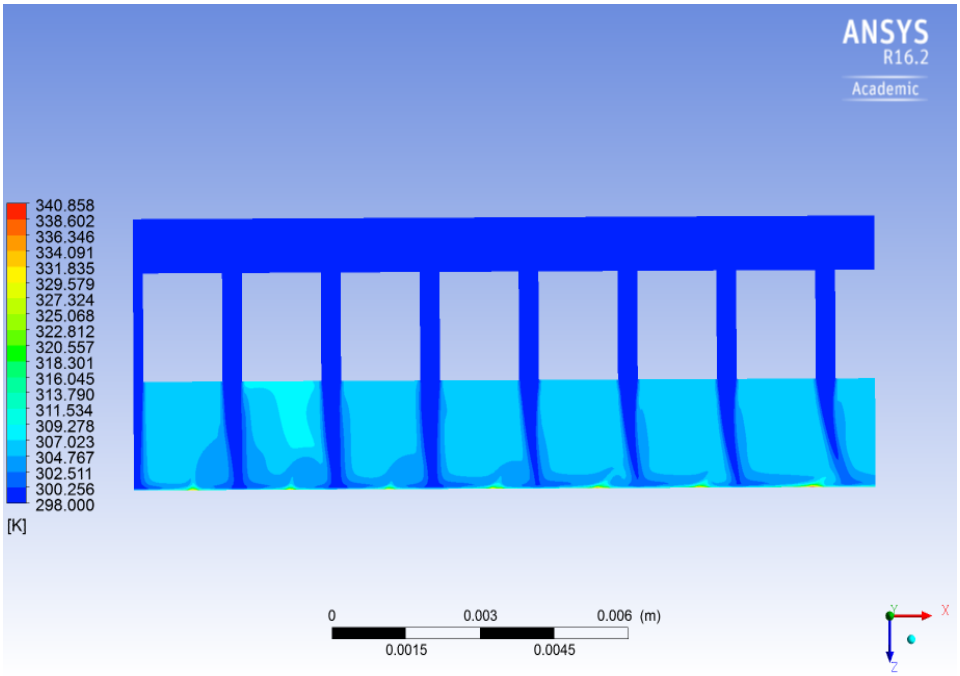

Figure 3.9: Temperature profiles of the jets in the channel

wise variation in the Nusselt number was not determined in the past experiments, this phenomenon can not be validated with any experimental results but, from the literature it was understood that a certain amount of cross flow enhances the heat transfer rates of the impinging systems.

The RANS simulations for multiple impinging jet array were carried out to assess the capability of eddy-viscosity RANS models to accurately determine the heat transfer rates and flow characteristics. Based on the advantages and disadvantages of different eddy-viscosity RANS models, three models were used perform

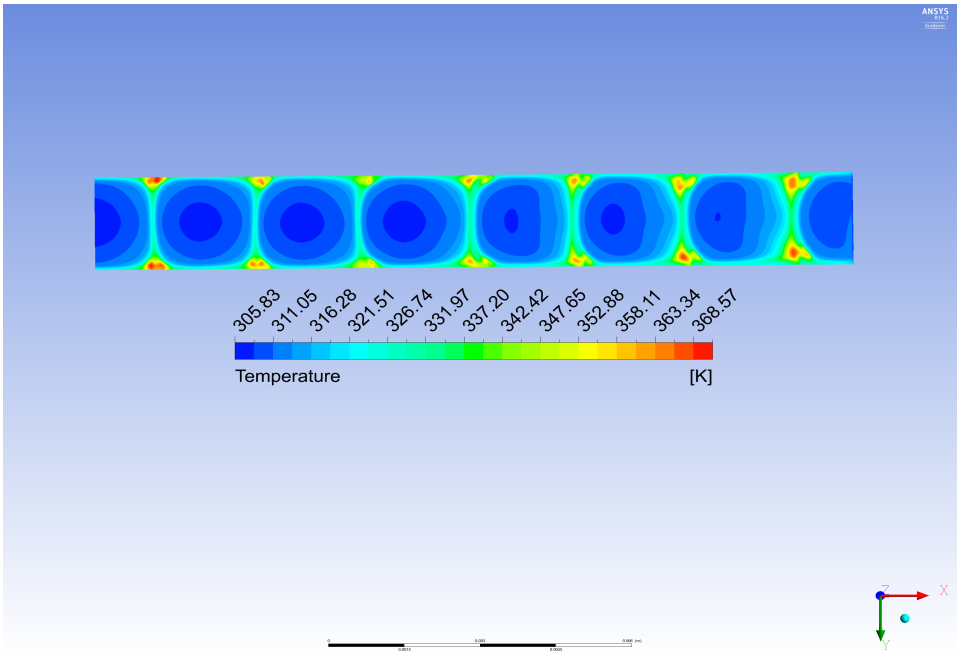

Figure 3.10: Temperature profile map on the impinging plate

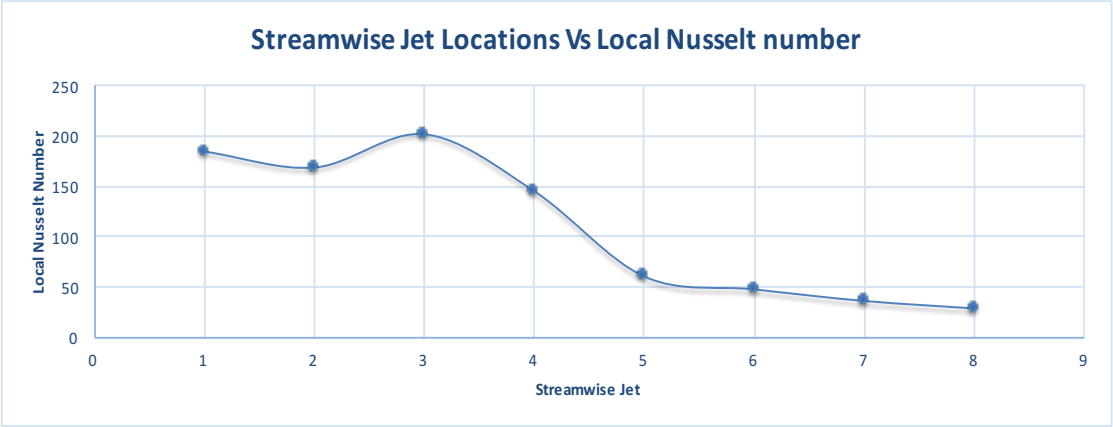

Figure 3.11: Streamwise variation of local Nusselt number for each 0.4 mm jet

the simulations. Due to the high computation time required for Reynolds stress model, this model was not used though it has the ability to accurately predict the flow characteristics near the wall region. However, a single case was tested to see the difference between RSM model and other models. It was observed that the heat transfer and pressure drop characteristics determined by RSM model did not vary much with SST $k-\omega$ model. Therefore, to conserve the computation time, the simulations were performed with SST $k-\omega$ model. It was observed from the above results that the SST $k-\omega$ model predicts better than the other two RANS models. The over prediction of the heat transfer characteristics by SST $k-\omega$ model could be due to the early prediction of kinetic energy or due to the improper prediction of stress anisotropy near the stagnation region. However, these results are in good agreement with the correlations of [Florscheutz *et al.*, 1981]. Flows which differ significantly from the wall parallel flows, such as impinging jets can only be tested with little success with RANS models. The limitations of these models is due to their physical assumptions and not due to the model constants. The strong anisotropies and complex mechanism of stress production near the impinging region can be modeled with high fidelity turbulence models. However, these RANS models would definitely act as a preliminary tool to understand the flow physics at a more basic level.

3.3. NUMERICAL SIMULATIONS FROM UNSTEADY RANS

Unsteady RANS equations are the general Navier - Stokes equations which retains the transient term during the computations unlike RANS and solves the equations for every time step. From the literature it was understood that, the unsteady RANS simulations provides detailed information about the flow physics as they are computed over a range of time steps. Therefore, they are being solved in diverse applications to capture the large scale unsteadiness in the flows. In the impinging flows, it has been observed that, the flow becomes complex near the wall region with strong anisotropy and high turbulent stresses. Due to the limitations of RANS models, the flow physics such as pressure drop characteristics were not able to predict accurately. Therefore, to capture the large scale unsteadiness in the flow at a minimal computation cost compared to LES and DNS, the unsteady RANS simulations have to be performed to analyze the flow characteristics of multiple jet impingement system.

3.3.1. COMPUTATION METHODOLOGY

In the steady state RANS simulations, the Navier - Stokes equations are time averaged in the simulations but the unsteady RANS simulations retains the time derivative to solve the flow equations. An overview on the RANS equations is given in 3.1. The simulations were performed on finite volume based commercial CFD package FLUENT and the mesh was generated using the meshing tool in ANSYS Workbench. The geometry and the boundary conditions remained the same as RANS case. The computational grid generated from the meshing tool is also similar to the RANS case with hexahedral elements and wall layers. Figure 3.12 represents the grid used for steady and unsteady RANS simulations. The wall layers are shown in figure 3.13. To perform the the simulations, SST $k-\omega$ model is used as it produced better results in the steady state simulations over the other turbulence models.

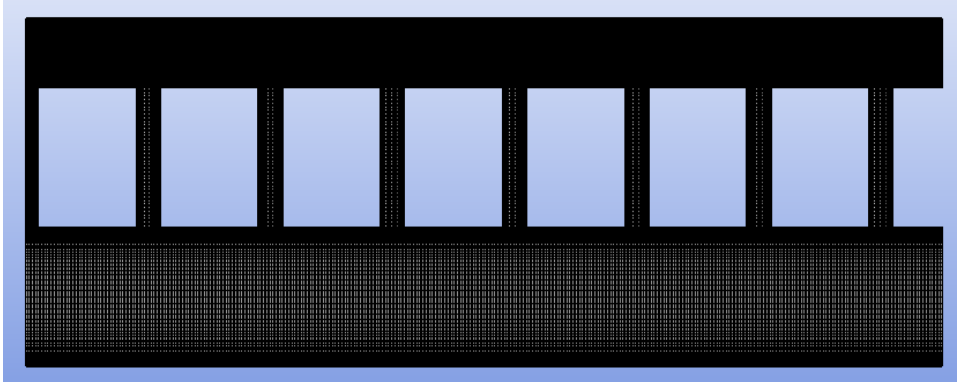

Figure 3.12: Structured mesh for RANS simulations

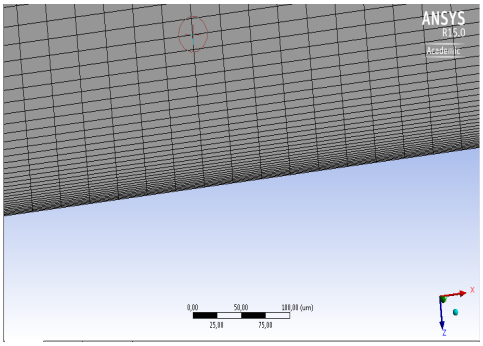

Figure 3.13: Wall layers in the mesh

For the unsteady RANS simulations, all the equations were discretized using the second order upwind for convective terms and for time marching, second order implicit scheme is used. For the pressure - velocity coupling, SIMPLE algorithm is selected. The simulations are performed for four flow through times. A time step of 1 X 10^{-4} is chosen and all the equations converged within 50 iterations per time step. In terms of the computation cost, a single URANS simulation took approximately 40 hours to simulate the four flow through times. The time step calculation is taken from the available literature. A total of five simulations were carried out at various Reynolds numbers between 400 < Re < 2000.

3.3.2. RESULTS

The impingement of vortex trains from the shear layer makes the flow unsteady. Though, the steady state RANS simulations have the capability to capture the flow field, the results did not provide detailed information about the unsteadiness of the jet due to the time averaging of quantities, but with the transient analysis, the analysis is much deeper as the computations are performed at every time step till the solution reaches a statistically stable state.

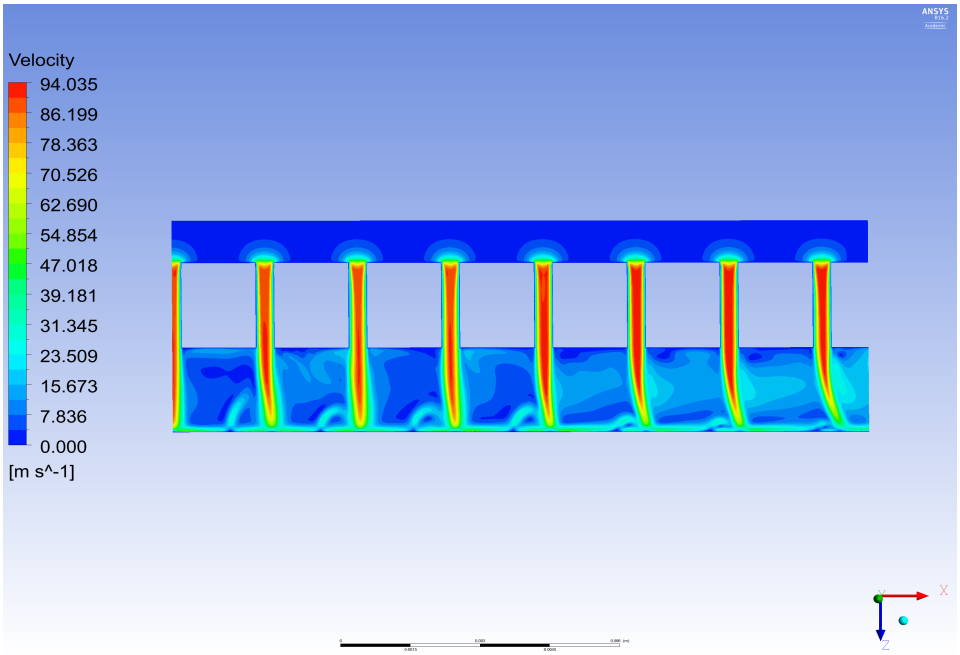

Figure 3.14: Velocity field before formation of vortex in the channel

Figure 3.14 and 3.15 represents the velocity distribution of jets in the array at two instances. The first one just represents the formation of upwash flow from the collision of wall jets and the other being the formation of vortex from the fountain flow. It was observed that, after the upwash is formed, the cross flow from the upstream jets forces the upwash flow to bend towards the flow direction there by forming a primary vortex. From the point monitors inside the nozzles, the unsteady RANS simulations shows an improvement over the steady state RANS simulations in predicting the mean normal velocities along the jet axis line. As mentioned in section 3.2.3, the velocity profile of the jet changes from the first jet to the last jet and due to the cross flow effect, the downstream jets starts to shift from their actual impinging region.

Figure 3.16 and 3.17 shows the local Nusselt number plot of the first and last jet. It is seen that, the jet profile follows a symmetrical profile along the positive and negative radial direction from the stagnation point but due to the spent air interaction with the upstream part of the jet, the heat transfer coefficients are relatively low when compared to the downstream part of the jet. For the last jet, it can be seen that the stagnation region is shifted to X/D=1. It was also noticed that the wall jet from the upstream jet decays near X/D=-2 and therefore there is a substantial drop in Nusselt number at X/D=-1.

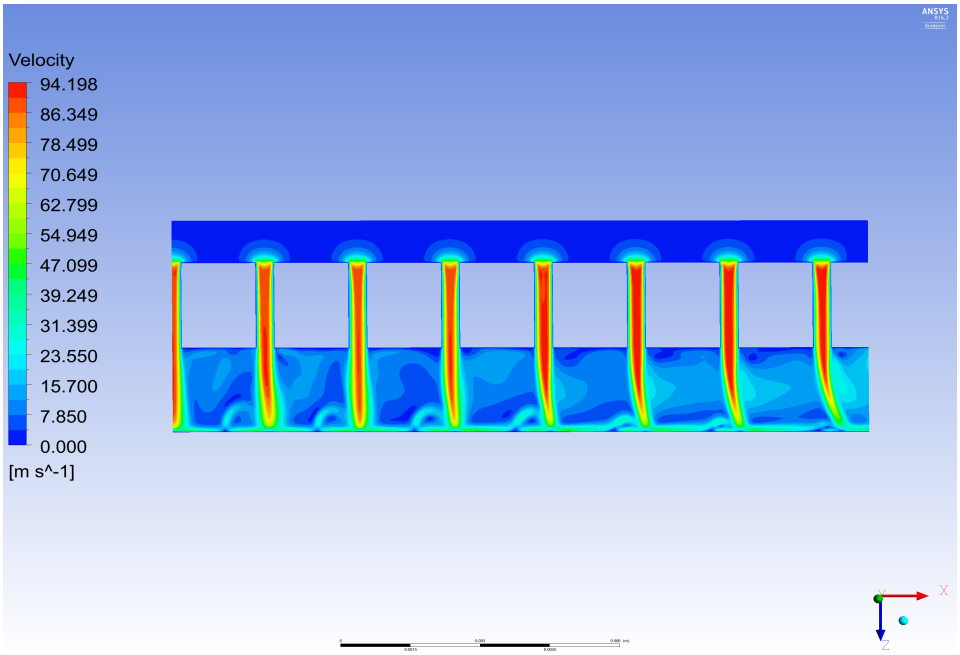

Figure 3.15: Velocity field after the formation of vortex

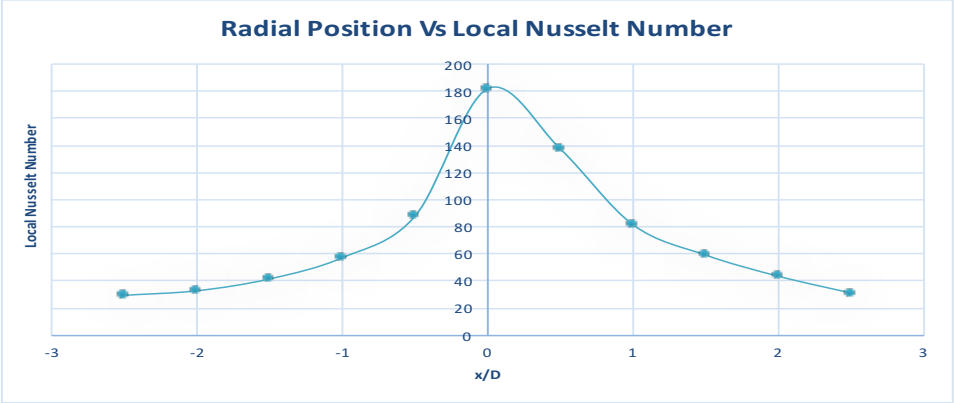

Figure 3.16: Distribution of local Nusselt number along the radial direction of the first jet

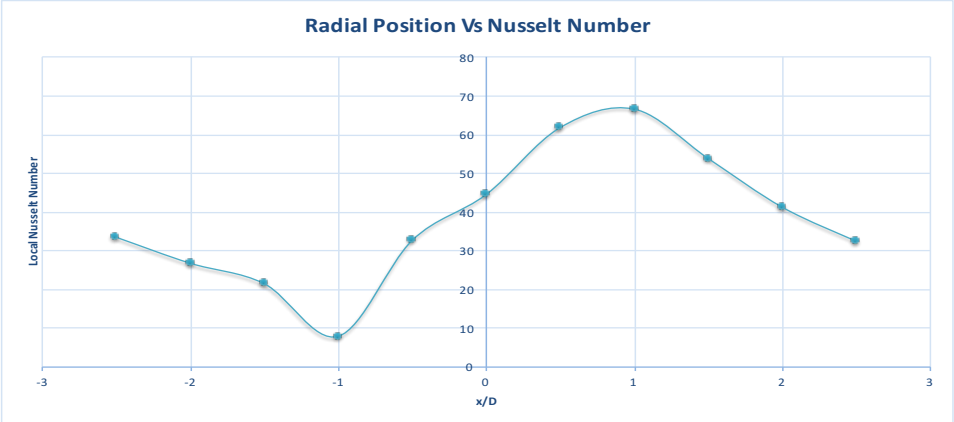

Figure 3.17: Distribution of local Nusselt number along the radial direction of the last jet

As mentioned earlier, the effect of primary vortex on the jet can be visualized through the turbulent kinetic energy contour maps. Figures 3.18 and 3.19 represents the turbulent kinetic energy profiles of the jets in the channel. It can be clearly seen from the figure 3.18 that, before the formation of vortex from the upwash flow, the magnitude of turbulent kinetic energy on the upstream part of the jet is relatively low but when the upwash flow is bent by the cross flow, the fountain flow starts to interact with the jet near the stagnation region by forming a vortex.

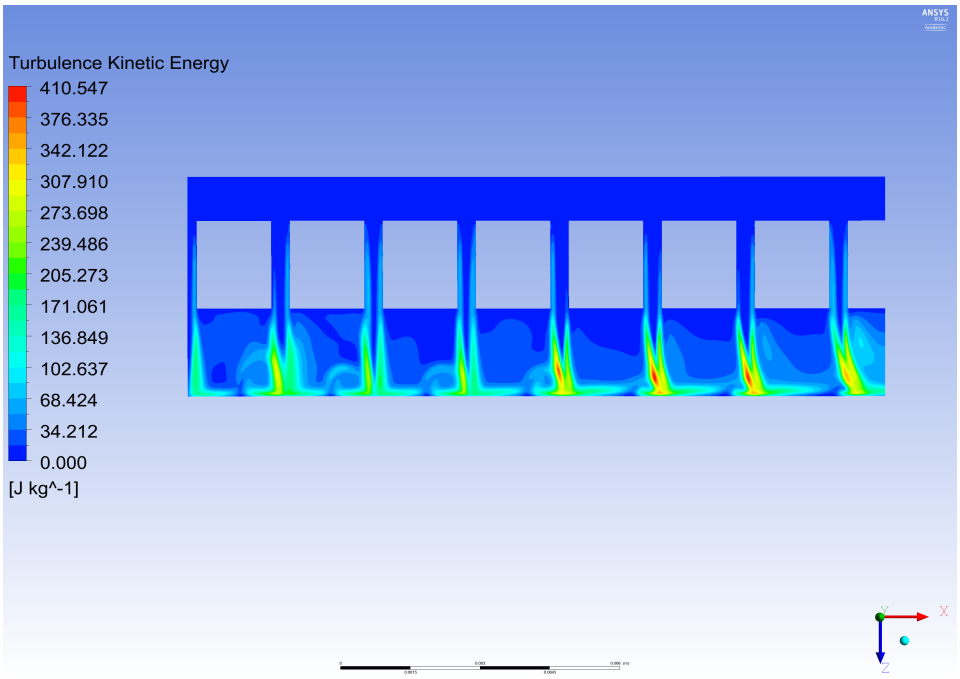

Figure 3.18: Turbulent kinetic energy profile before the vortex formation

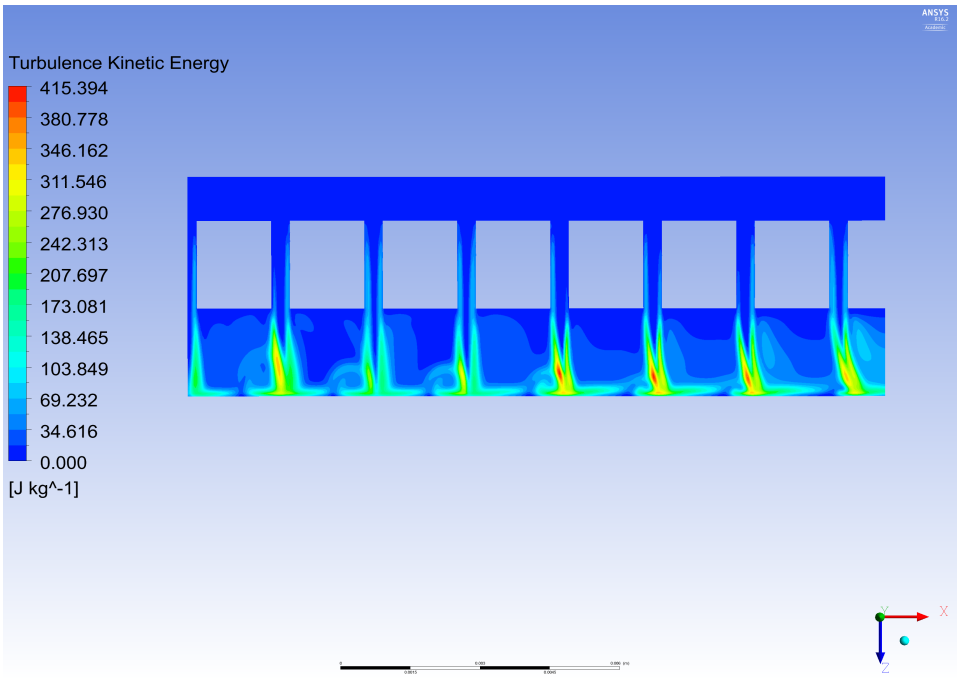

Figure 3.19: Turbulent kinetic energy profile after the vortex formation

The results obtained from URANS simulations are validated with the steady state RANS simulations and experimental results of [Rao *et al.*, 2010] to predict the heat transfer characteristics. Figure 3.20 shows the comparison of average Nusselt number with varying Reynolds numbers.The results from URANS simulations shows a substantial improvement over the steady state RANS simulations in predicting the average heat transfer coefficients. This improvement in the results might be due to the ability of URANS equations in predicting the jet mean velocities along the core region.

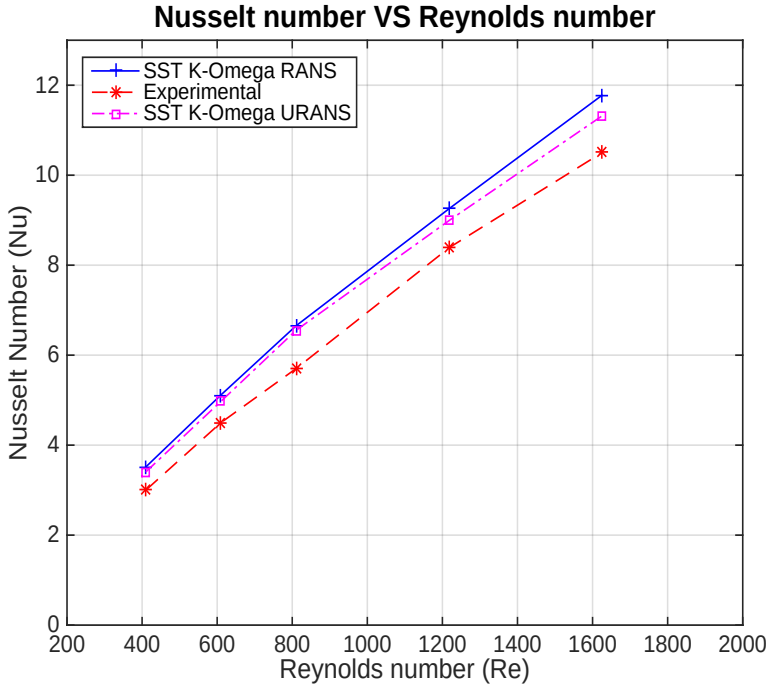

Figure 3.20: Validation of steady and unsteady RANS models – Variation of average Nusselt number with Reynolds number

Comparison of pressure drop results show that both steady and unsteady RANS models were not able to predict the results accurately. The values obtained from the CFD simulations are significantly higher than the experimental results. The deviation of CFD results with experimental data is about 50 % and this difference increases with increase in Reynolds number as shown in figure 3.21. The static pressure contour from the the simulations is shown in figure 3.22. Similar to the static pressure map as seen in the RANS simulations, it can also be seen here that the pressure drop inside the nozzle is uniform but because of the cross flow at the exit some non-uniformity appears. Furthermore, due to the increase in air velocity, the increased pressure gradients from the nozzles are extended to the outlet.

To have a better understanding on the pressure drop inside the jet array, an additional investigation is performed using particle tracking technique. With this technique, the particles can be traced to study their pressure dissipation at various locations inside the array. Using the discrete phase modeling technique in Fluent, few particles were injected from the inlet. The trajectory of these particles are computed over the number of time steps through out the flow domain. Boundary conditions have to be defined so that the injected particles follow where to start, reflect and escape. Figure 3.23 shows the results obtained from particle tracking for Re = 1220.

From the obtained results, it can be inferred that the pressure drop with in the array is contrasting for different particles. It was understood that most of the pressure drop occurs because of vena contraction effect for the particles near the wall and further downstream of the flow, the pressure drop for these particles occurs due to friction losses. Where as, the particles in the mean flow is not affected due to frictional losses. However, the pressure drop for these particles occurs after the nozzle exit due to the loss of kinetic energy in the jets. The conclusions drawn from the particle tracking approach can be validated with a semi analytical approach.

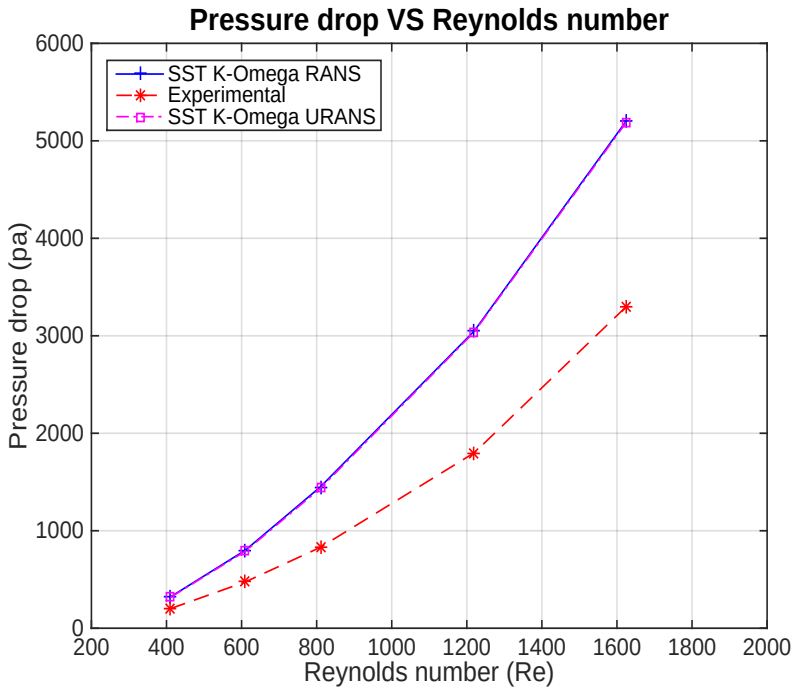

Figure 3.21: Validation of steady and unsteady RANS models – Variation of total pressure drop with Reynolds number

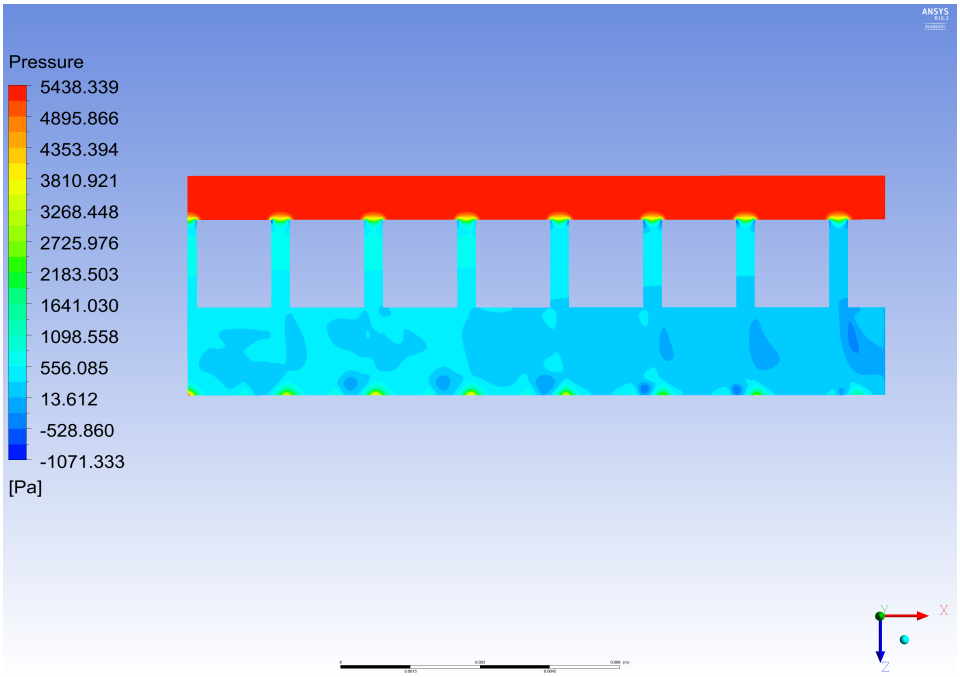

Figure 3.22: Static pressure map from the URANS simulation

A semi analytical method is an inexpensive empirical approach which is used to predict the pressure losses in a system. Though CFD simulations provide a better understanding of the variation of pressure and pressure drop within the systems, these results are not always trustworthy. Therefore, the results have to be validated with experimental and analytical approaches to come to a conclusion. The sum of local resistances approach is an analytical approach provided by [Idel'chik and Isaak, 1996] to determine the pressure drop in systems through various schemes. For the impinging jet system, the total pressure loss is defined as the sum

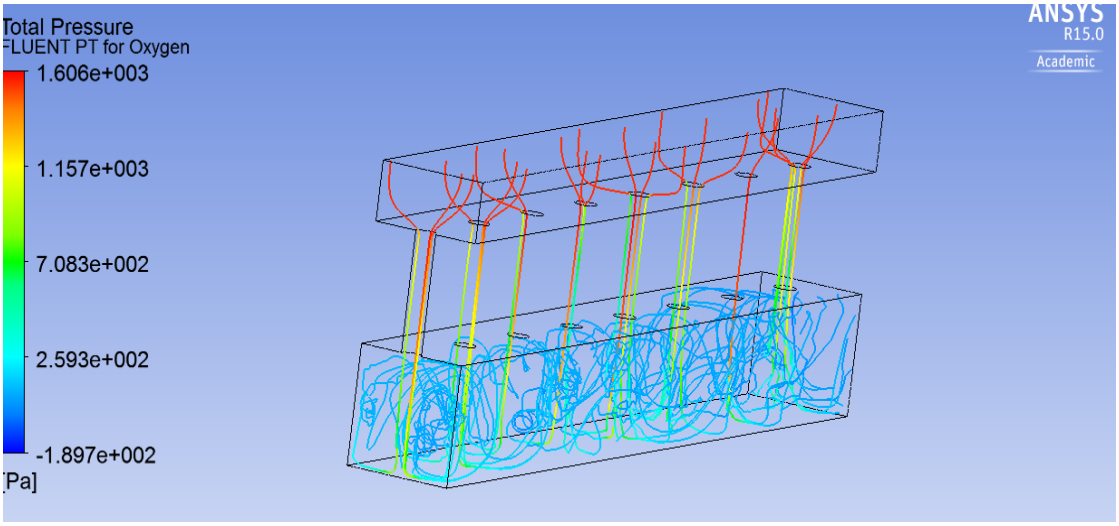

Figure 3.23: Particle tracking of total pressure drop from 0.4 mm jets at Re = 1220

of pressure losses that occurs in nozzle inlet, nozzle exit, frictional loses in the nozzle and losses in the cross flow channel as represented in equation 3.27.

$$\Delta P = \Delta P_{n_{in}} + \Delta P_{n_{out}} + \Delta P_{n_{fr}} + \Delta P_{ch_{out}}, \tag{3.27}$$

At the nozzle inlet and outlet, the pressure loss can be calculated from a pressure resistance coefficient as given in [Idel'chik and Isaak, 1996]. Results obtained from the semi analytical approach and CFD results are compared with the experimental results in figure 3.25. The CFD simulations are fairly in good agreement with the semi empirical relations. Hence, the results from semi analytical approach can be used for preliminary estimation for designing the jet impingement systems. With this approach, the local pressure drop values obtained from particle tracing technique can be validated with the analytical results to have an insight into the regions where most of the pressure drop occurs. From both the approaches it was understood that the most of the pressure drop happens in the vicinity of nozzles inlet region and at the nozzle exit region as seen in figure 3.23.

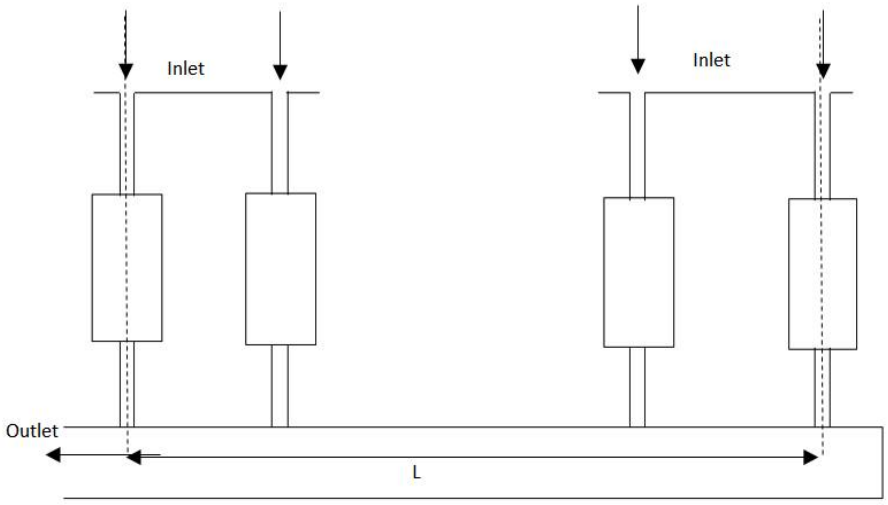

Figure 3.24: Scheme for pressure drop calculation [Idel'chik and Isaak, 1996]

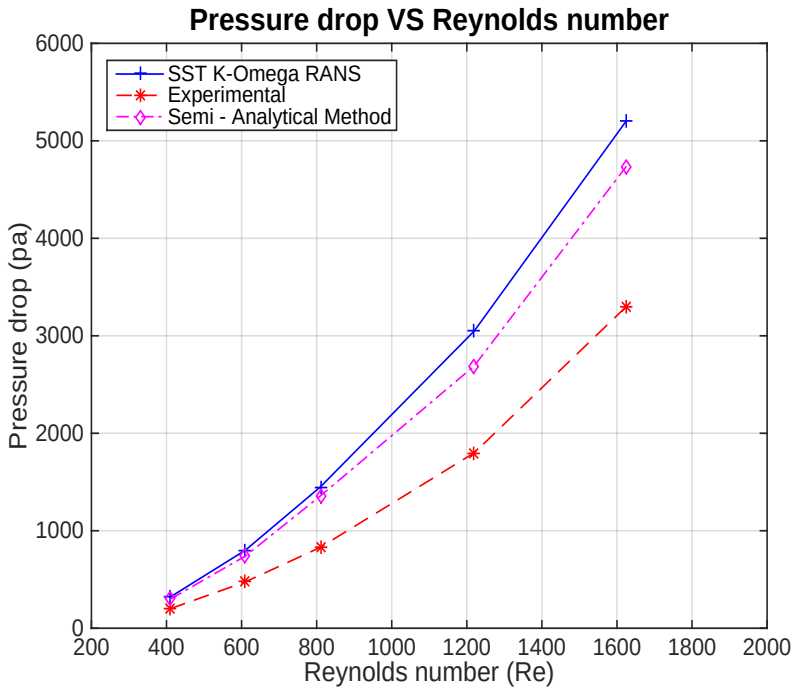

Figure 3.25: Validation of CFD results with analytical approach – Variation of total pressure drop with Reynolds number

The main objective to perform the URANS simulations is to understand the flow physics inside the multiple jet impinging array. Several simulations were performed with varying Reynolds numbers to determine the heat transfer and pressure drop characteristics of multiple impinging jets. Simulations were performed for every time step until the flow reaches statistically stable state. From the simulations, it was understood that, the upwash formed by the two successive wall jets bends in the downstream direction to form a primary vortex. This is due to the interaction between the upwash flow and the cross flow. As the cross flow from the upstream jets starts to flow downstream, the upwash flow interacts with the spent air to form a vortex. Furthermore, these vortices interacts with the shear layer of the jet to produce high velocity fluctuations thereby increasing the turbulence levels. By validating the CFD results with the experimental results, the unsteady RANS results predicted better than the RANS results. This is due to the better prediction of jet centerline velocities with the URANS approach. However, there was no substantial improvement in determining the pressure drop characteristics. Therefore, to understand the pressure drop characteristics in the array, an additional study was performed using particle tracing technique. The local pressure drop values obtained from particle tracing method are validated with the results obtained from analytical approach. It was found that the pressure drop values are in good agreement with the analytical results. Thus, it can be inferred that, the unsteady RANS approach is capable to predict the heat transfer characteristics and flow physics in a qualitative way compared to RANS models. Therefore, this approach can be used to perform a qualitative analysis on complicated flows.

4

LARGE - EDDY SIMULATIONS

This chapter provides an overview on the theoretical approach required to model the multiple impinging jets through large - eddy simulations. In section 4.1, an overview of the available LES models are discussed. Section 4.2 presents with a detailed overview on the computational methodology employed in the current study to model the impinging jet array in low Reynolds number region. This section also discusses about the computational geometry, discretization of mesh, boundary conditions and the solution procedure. The results from the LES are discussed in section 4.3. The main objective of this analysis is to investigate the capability of the LES models to accurately predict the flow phenomenon and heat transfer of multiple impinging jets.

4.1. INTRODUCTION

This section provides a short overview of the basic principles and functionalities of large-eddy simulation method. In large-eddy simulations, the larger turbulent scales are directly represented but the effects of smaller-scales are modeled. To run large-eddy simulations, high computation power is required than RANS models but when compared to DNS, it is less. Since, the large-scale motions are represented explicitly, LES is expected to be reliable and more accurate than RANS models for flows such as unsteady flows, vortex shredding flows. The main purpose of implementing the LES approach to the present problem is to investigate the performance of LES and its potential to calculate the budgets of transport equations for various quantities.

The fluid motion is described by continuity and Navier - Stokes equations of motion and complemented by the energy equation. To describe the flow mathematically, three basic flow equations are necessary. These conservation laws are already represented in the section 2.3. However, it is important to recall them to represent the LES formulation. The three conservation laws are represented as:

$$\frac{\partial U_i}{\partial x_i} = 0 \tag{4.1}$$

$$\frac{\partial U_i}{\partial t} + U_j . \frac{\partial U_i}{\partial x_j} = -\frac{1}{\rho} . \frac{\partial p}{\partial x_i} + \nu . \frac{\partial^2 U_i}{\partial x_j^2} \tag{4.2}$$

$$\frac{\partial T}{\partial t} + U_j . \frac{\partial T}{\partial x_j} = a . \frac{\partial^2 T}{\partial x_j^2} \tag{4.3}$$

In the above equation 4.3, the fluid is assumed to be thermally perfect, where enthalpy depends on just temperature and not on both temperature and pressure. Here 'T' is the temperature of the fluid and 'a' is the heat diffusivity.

To understand the concept of large - eddy simulations (LES), the best starting point is to understand the direct numerical solutions (DNS). In the DNS approach, the solution represents all scales of motion, i.e, from the largest turbulence scales to the smallest dissipative scales. Therefore, all these turbulence scales also called as kolmogorov scales are resolved and computed. Since DNS resolves all kolmogorov scales, the computational cost increases rapidly with the Reynolds number. Due to the high computation time and cost, the DNS simulations are confined to low Reynolds applications with simple geometries. These kolmogorov micro scales are defined as:

$$\eta = \left(\frac{\nu^3}{\epsilon}\right)^{\frac{1}{4}} [m] \tag{4.4}$$

$$\tau = \left(\frac{\nu}{\epsilon}\right)^{\frac{1}{2}} [s] \tag{4.5}$$

$$v = (\nu\epsilon)^{\frac{1}{4}} [m/s] \tag{4.6}$$

Where η, τ and v are the length, time and velocity scales that are associated with the smallest eddies that occur in a given flow. Figure 4.1 illustrates how the energy is transferred from large eddy scales to micro scale eddies. These kolmogorov micro scales are destroyed by the viscosity and therefore these smaller eddy scales dissipates the obtained energy as heat.

The data obtained from the results of a DNS simulations are also huge, and often requires a lot of post-processing. The time required to start a simulation and process the results during post processing is often referred to as the"Turnaround time" and the DNS simulations are considered as the most demanding approach with respect to computational expense and turnaround time. At the other end of this range, the RANS approach is regarded as the least amount of turnaround time due to the averaging of the transport quantities.This does not imply that all RANS simulations are quick and require little computational cost but in real time scenarios, RANS simulations are often applied to problems with complex geometries and high Reynolds numbers. However, these RANS simulations gives time averaged solutions and some of the unsteady physics in the flow is inaccurately predicted.

An alternative solution to model the complex flows is by performing a simulation which resolves only the large, energy-containing eddies and model the rest of the energy spectrum which contains smaller scales. This approach is called Large Eddy Simulation (LES). LES is based on an assumption that large, energy-containing eddies determine the main flow dynamics. The small eddies that lie in the inertial and dissipative sub-ranges of the energy spectra are assumed to be isotropic and not to influence flow properties significantly, but nevertheless they have to be modeled to come to a qualitative solution. The modeling of smaller scales by LES is shown in the energy spectrum figure 4.2. Figure 4.3 represents the size of large eddies and small eddies as a function of grid size.

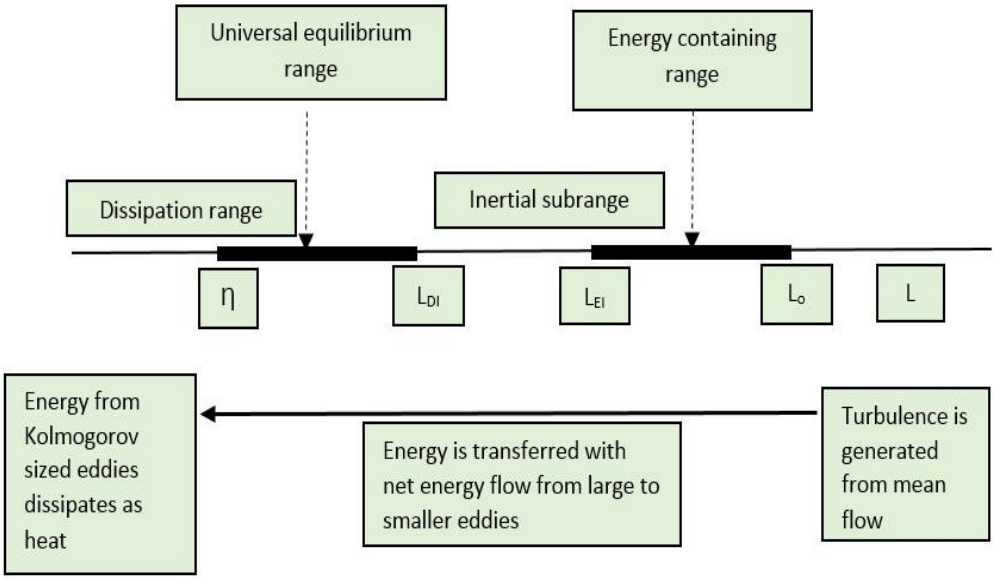

Figure 4.1: Energy transfer from larger eddies to smaller eddies [Pope, 2000]

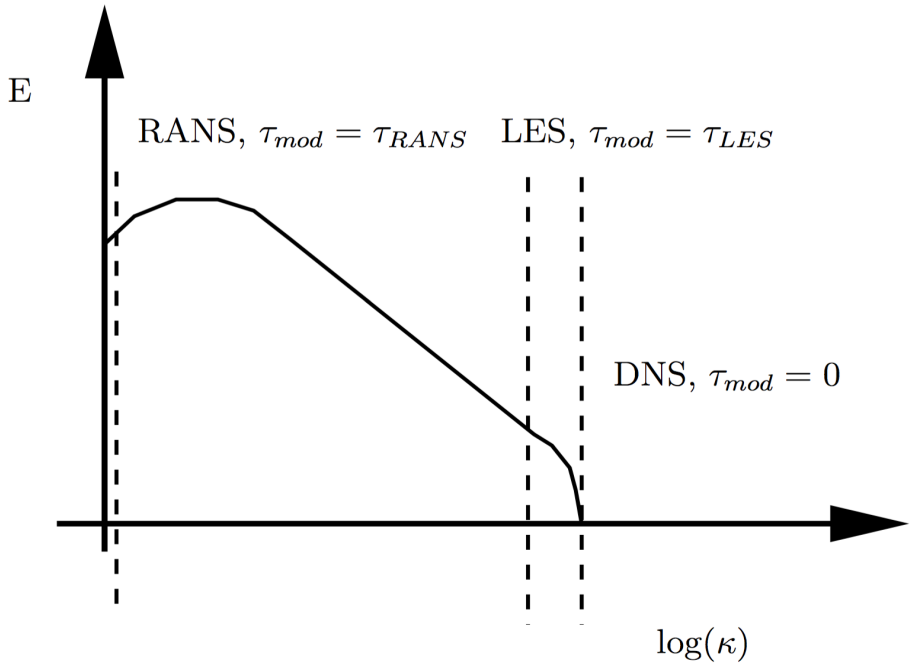

Figure 4.2: Modeling of LES approach in Energy Spectrum [Pope, 2000]

In order to model these micro scales, they have to be separated from the large scales. To separate the small scales from the large scales of motions, a filtering operation should be done for the Navier - Stokes equations. The velocity U (x, t) is decomposed into the sum of filters component $\overline{U}(x,t)$ and sub grid scale component u (x, t). The filtered velocity component represents the motion of large eddies. Likewise, the temperature component is also decomposed into sum of filtered components and surged scale components. Figure 4.4 shows LES filtering approach.

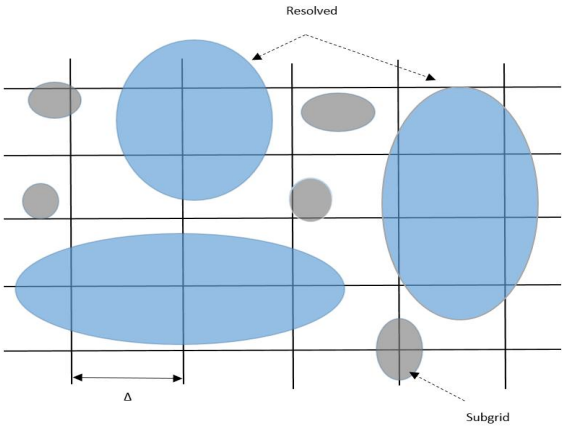

Figure 4.3: Eddy size as function of grid size

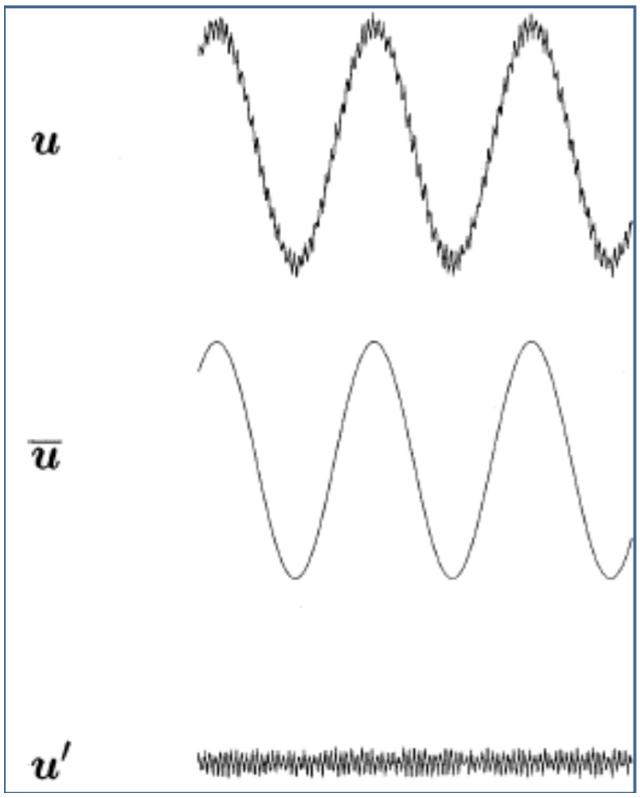

Figure 4.4: Filtering operation in LES

$$U(x,t) = \overline{U}(x,t) + u(x,t), \tag{4.7}$$

$$T(x,t) = \overline{T}(x,t) + t(x,t), \tag{4.8}$$

Leonard [Leonard, 1974] proposed to model $\overline{U}(x,t)$ by the equation 4.9, where G (r, x) is a filter function that satisfies the normalization condition and the integral is called convolution.

$$\overline{U}(x,t) = \int_{-\infty}^{\infty} G(r,x)U(x-r,t)dr, \tag{4.9}$$

$$\int_{-\infty}^{\infty} G(r,x)dr = 1, \tag{4.10}$$

The Gaussian filter can be mathematically represented as:

$$G(r) = \sqrt{\frac{6}{\pi\Delta^2}} exp\left(-\frac{6r^2}{\Delta^2}\right), \tag{4.11}$$

The box filter is represented as

$$G(r) = \begin{cases} 1/\Delta & if|r| < \Delta/2 \\ 0 & otherwise \end{cases} \tag{4.12}$$

$$G(r) = \begin{cases} 1/\Delta & if k < \pi/2 \\ 0 & otherwise \end{cases} \tag{4.13}$$

The above equation 4.13 represents the Fourier cut-off filter. Generally, if the discretization is by finite volume method, it is quite preferable to use box filter and in the Fluent solver, the filtering is done automatically by means of the filter length L_s which is dependent on the grid resolution. filter G does not occur as it is but the way it works, it will discard the smaller scales which are small then the grid size. When the filter is applied to Navier-Stokes equations, then the equations will be represented as 4.14, 4.15 and 4.16. Equation 4.15 is little different from Navier-Stokes equation as the advection term in the current equation has unresolved eddies on the velocity field. This term is modeled by residual stress tensor which is analogous to Reynolds-stress tensor.

$$\frac{\partial \overline{U}_i}{\partial x_i} = 0 \tag{4.14}$$

$$\frac{\partial \overline{U}_i}{\partial t} + \frac{\partial \overline{U_i U_j}}{\partial x_j} = \nu . \frac{\partial^2 \overline{U}_i}{\partial x_i . x_j} - \frac{1}{\rho}\frac{\partial \overline{p}}{\partial x_j} \tag{4.15}$$

$$\frac{\partial T}{\partial t} + \overline{U}_j . \frac{\partial T}{\partial x_j} = \frac{\partial}{\partial x_j}\left(k . \frac{\partial T}{\partial x_j} - \overline{u_j t}\right) \tag{4.16}$$

$$\tau_{ij}^R = \overline{U_i U_j} - \overline{U}_i \overline{U}_j, \tag{4.17}$$

This term τ_{ij}^R is the nonlinear advection term. This term has to be modeled to close the equations. The advection term is decomposed into three terms: Term 1, $(\overline{\bar{u}_i \bar{u}_i} - \bar{u}_i \bar{u}_i)$ describes the interaction between two resolved scales which produces unresolved turbulence. These scales transfer from large to smaller flow structures. Term 2, $(\overline{\bar{u}_i u_j} + \overline{\bar{u}_j u'_j})$describes the interaction between resolved and unresolved scales which produces the unresolved turbulence. These scales transfer the energy either way. i.e, both from small to large scales and vice-versa but the net transport of average energy is transferred from larger to smaller scales. Term

3, $(\overline{u'_j u'_j})$ describes the interaction between two unresolved eddies contributing to the unresolved turbulence including a large scale eddy. therefore, it becomes evident that the subgrid scale Reynolds stress term provides more detailed physics in terms of energy transport than the Reynolds stresses from the RANS approach. It is also understood that as the filter width gets smaller, the solution is similar to DNS approach. Furthermore, the heat flux in the energy equation 4.16 should also be modeled for heat transfer problems. In the equation 4.18 $P_r t$ is a constant value.

$$\overline{u_j t} = -\frac{\nu_t}{P_{rt}} \frac{\partial T}{\partial x_j}, \tag{4.18}$$

4.1.1. SMAGORINSKY SUBGRID- SCALE MODEL

It is one of the first models to be proposed and it is still widely used as it is based on the hypothesis of Boussinesq eddy-viscosity concept. The correlation occurs between the SGS stress component τ^R_{ij}, to the strain rate of the velocity field $\overline{S}_{ij}$.

$$\tau^R_{ij} - \frac{1}{3}\tau_{kk}\delta_{ij} = -2\overline{S}ij\nu_t, \tag{4.19}$$

From the above equation 4.19, ν_t has to be determined.

$$\nu_t \propto l_s u_{sgs}, \tag{4.20}$$

$$l_s = \Delta = (\Delta V)^{1/3}, \tag{4.21}$$

Where l_s and u_{sags} is the length scale and velocity scale. The length scale is determined from mesh size but if the mesh size is not uniform, then to define the length scale becomes complex task. The most common definition is given in the equation 4.21 by taking into picture, the volume of the cell. On the other hand, velocity scale is related to the gradients of $\overline{U}_i$ and it can be represented as:

$$u_{sgs} = l_s|\overline{S}|, \tag{4.22}$$

Where $|\overline{S}| = \sqrt{2\overline{S}_{ij}\overline{S}_{ij}}$ is the magnitude of strain rate.

$$\overline{S}_{ij} = 0.5\left(\frac{\partial \overline{U}_i}{\partial x_j} + \frac{\partial \overline{U}_j}{\partial x_i}\right), \tag{4.23}$$

and finally eddy-viscosity is defined as:

$$\nu_t = (C_s\Delta)^2|\overline{S}|, \tag{4.24}$$

There are several drawbacks with the Smagorinsky model. The non-universality of the constant C_s is one of them. Different types of flows have different optimal value of C_s . The values vary from 0.065 to 0.2. In order to obtain the correct distribution of the values in near-wall region, we use van Driest damping function:

$$C_s = C_{s0}\left(1 - e^{-y^+/25}\right)^2, \tag{4.25}$$

In the above equation 4.25 y^+ is the distance from the wall in the viscous layers and C_{s0} is the Smagaronsky constant away from the wall boundaries. This model is also highly dissipative which causes some back scatter if not correctly modelled but the model is simple and for this reason it is quite popular.

4.1.2. GERMANO DYNAMIC MODEL

The dynamic model or Germano dynamic model was develop by Germano in 1991. In this model, the main drawback of the standard Smagaronsky model is solved. The model also uses the same hypothesis obtained from Boussinesq definition but the constant is derived from a dynamic procedure. The dynamic procedure is evolved from the concept that the resolved scales which are close to cut-off scale are similar to the modelled ones. The sub-grid scale is not only applied on the scaled grid but also on the coarse grid. So the coarse grid is the test filter. The stresses over these two grids can be defined as:

$$\tau_{ij} = \overline{U_i U_j} - \overline{U}_i \overline{U}_j \approx \tau_{ij}^{mod}(C, \Delta, \overline{U}), \tag{4.26}$$

$$T_{ij} = \widehat{\overline{U_i U_j}} - \widehat{\overline{U}_i}\,\widehat{\overline{U}_j} \approx T_{ij}^{mod}(C, \widehat{\Delta}, \widehat{\overline{U}}), \tag{4.27}$$

These test scale stresses T_{ij} are obtained when the second filter is applied on the Navier-Stokes equations. From the above two equations 4.26 and 4.27, the total stresses $\overline{U_i U_j}$ can be written as the sum of the resolved stresses on the grid $\Delta, \overline{U}_i, \overline{U}_j$ and the remainder τ_{ij}. As a result, the equaltion of T_{ij} becomes,

$$T_{ij} = (\widehat{\overline{U}_i \overline{U}_j} - \widehat{\overline{U}_i}\,\widehat{\overline{U}_j}) + \widehat{\tau}_{ij} \tag{4.28}$$

This equation 4.28 is called Germano identity.L_{ij} represents the resolved stresses of the scales as there length is between the test and grid filter.L_{ij} is there first term on the right hand side of equation 4.28.

$$L_{ij}^{mod} = -2C\widehat{\Delta^2}|\widehat{\overline{S}}|\widehat{\overline{S}}_{ij} + 2C\widehat{\Delta^2|\overline{S}|\overline{S}_{ij}} \tag{4.29}$$

In ideal case, L_{ij}^{mod} should be equal to L_{ij} and from this condition C_s can be formulated. Finally C_s is obtained as:

$$C_s = -\frac{1}{2}\frac{L_{ij}M_{ij}}{M_{ij}M_{ij}} \tag{4.30}$$

Where M_{ij} is defined from the equation 4.31 below:

$$L_{ij}^{mod} = -2C\widehat{\Delta^2}|\widehat{\overline{S}}|\widehat{\overline{S}}_{ij} - 2C\widehat{\Delta^2|\overline{S}|\overline{S}_{ij}} \tag{4.31}$$

The advantage of the Germano dynamic model over the standard Smagorinsky model is that the coefficient C_s is not predefined, but infact it is determined by the equation itself. So, it has a correct near wall behavior which doesn't require damping functions and most importantly, the coefficient can be negative during back scatter which is good.

4.1.3. WALL MODELED LES (WMLES)

Wall Modeled LES (WMLES) is an alternative method to classical LES approach. It reduces the demanding mesh resolution requirements of classical wall resolved LES. It is observed from the literature that, with the increase in wall distance, the near-wall turbulence length scales are increased linearly which results in smaller eddies as the surface (wall) is approached. This effect is limited by molecular viscosity and the eddies are damped out inside the viscous sublayer. These eddies becomes smaller and smaller with increase in Reynolds number by forming thinner viscous layer. Therefore, it becomes a challenging task for LES to resolve these smaller scales. Hence, a combination of LES and RANS models enables the flow problem to solve effectively. In the near-wall region, the problem switches to RANS modeling and if the grid size becomes sufficient to solve larger scales, the solution switches to LES formulation.

The WMLES formulation in ANSYS Fluent is based on the formulation of Shur et al. (2008):

$$\nu_t = f_D.S.min\{(\kappa y)^2, (C_{SMAG}\Delta)^2\} \tag{4.32}$$

where 'y' is the wall distance, κ is the von Karman constant, 'S' is the strain rate and f_D is a near-wall damping function. This is a general purpose formulation used in Fluent. Near the wall, the minimization function selects the Prandtl mixing length model, whereas away from the wall it switches over to the Smagorinsky model.

4.2. COMPUTATION METHODOLOGY

Large Eddy Simulations approach is a powerful tool for applications like heat transfer and turbulence. The LES results are time-dependent, which makes the problem convenient to study the instantaneous flow patterns and their evolution with time. Also, this high fidelity solver mechanism makes the problem easier to study the eddy structures and their dynamics that evolves with time. Furthermore, LES is capable of providing information that is inaccessible to experiments. This might be due to the inability to measure the flow quantities or because of insufficient resolution in all flow areas. Therefore, It is important to measure the flow quantities near the wall region as they are crucial for determining the heat transfer characteristics of the system but it is quite hard to measure the velocities and turbulence quantities in the near wall region and they are often subjected to numerical errors. Performing eddy simulations in these scenarios can provide deeper insight into the main physical mechanisms behind the multiple impinging jet array.

4.2.1. COMPUTATIONAL DOMAIN AND GRID

The geometry for performing LES simulations is similar to the one consider for RANS approach as shown in figure 3.2. A series of circular jet enters through the nozzles, flows through all the nozzles and hits the impingement plate. The spent air leaves the channel exit which is situated at a distance of 15 mm from the center jet. The diameter of the jet is set at 0.4 mm.

Computational grid for the LES simulation is generated from the ANSYS meshing tool. Structured grid with hexahedral elements are used for simulation and the grid is constructed to be very dense to capture the flow features inside the array. The mesh consists of $7.4 \text{ X } 10^6$ cells and the mesh resolution is close to LES criteria. The quality of the mesh resolution can be approximated by comparing the mesh size Δ to an Kolmogorov length scale η. The Kolmogorov length scale describes the smallest dissipative eddies. The η is defined in equation 4.33. In the equation η is the molecular viscosity and ϵ is the dissipation rate. It can be seen that, for the current mesh, the ratio $\frac{\Delta}{\eta} < 2$. The calculation of length scale and grid spacing is defined in appendix A.

$$\eta = \left(\frac{\nu^3}{\epsilon}\right) \tag{4.33}$$

4.2.2. BOUNDARY CONDTIONS AND SOLUTION PROCEDURE

The definition of the boundary conditions should be given carefully in order to successfully compare with the experimental results. “Velocity- Inlet" is used as the boundary condition for inlet, while “Pressure-Outlet" is used as the outlet boundary condition. For the walls on sides and at the center, "Symmetry" boundary condition has been used to discretize the array of 225 holes into a single row of 7.5 jets. Simulations were carried out using ANSYS Fluent which uses finite volume method and the convergence tolerance of 0.001 was set to carry on the simulations.

LES simulations are performed on Fluent solver using wall modelled LES model (WMLES) due to its better capability of solving near wall flows over the other conventional LES models. All governing equations are time marched using a second order implicit time step scheme. For discretizing the momentum equations, bounded central differencing scheme is used and for pressure velocity coupling SIMPLE algorithm is used. Time step is chosen to be 4 X 10^{-6} s and the solution converged with in 30 – 40 iterations per time step. The computational time required to run the LES simulations in a system with 8 processors and 16 GB RAM on parallel processing took approximately 10 days. The calculation for time step is shown in appendix A. Simulation was carried out till the solver reaches a convergence criteria of < 10^{-3}. The continuity, momentum and other parameters convergence was set to 10^{-3}, while the convergence of the energy equation was set to 10^{-6}. In most cases, the momentum and other residuals were less than 10^{-5} and the highest residual was 7 X 10^{-4}. The main criteria for stopping the simulation are the simultaneous occurrence of flattening of residual plots and flattening of the average heated plate temperature with respect to the iteration number.

4.3. RESULTS

One of the characteristics of the jet configuration currently implemented is that the potential core starts to decay as the target plate is kept five diameters away from the nozzle exit and therefore, the shear layer instabilities dominates to enhance the heat transfer rates on the impinging plate [Kataoka, 1990].

The instantaneous velocity field map of the impinging jets in the array is shown in figure 4.5. The incoming jet interacts with the ambient fluid by spreading the jet radially through which the shear layer is generated. This shear layer towards the end leads to the jet core being consumed. The process of the potential core disappearing is explained by [Yule, 1978]. A comparison of instantaneous velocity contours between URANS and LES computations shows that the velocity contours from the LES simulations provide much more detailed information about the flow structures compared to the URANS contours. Furthermore, it is evident that the LES computations have qualitatively resolved the different scales of turbulence where as, the URANS simulations were not able to predict the same range of eddy structures. Furthermore, it was observed from the results that, initially when the jets stars to impinge on the target surface, all the jets in the array impinges on the plate without any deviations or distortions as the cross flow is not affecting the downstream jets. Figure 4.6 shows the velocity fields of all jets impinging on the surface for the first time.

In the jet centreline, the mean-axial velocity remains nearly constant but after Z/D = 2.0 the flow decelerates either due to the cross flow effect or because of the presence of the impingement wall. It is also believed that this effect could be due to the combined effect of cross flow and the potential core decay. However, further away from the stagnation region, at r/D = 0.5, it was observed that there exists a region of strong anisotropy of turbulence because, this position coincides with the centre of jet shear layer.

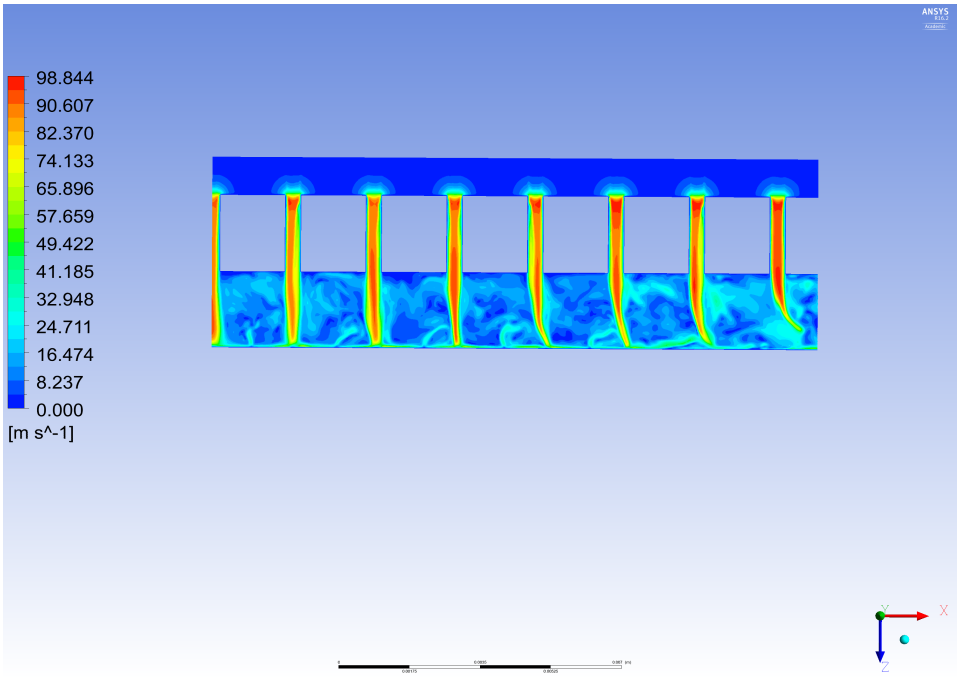

Figure 4.5: Instantaneous velocity field in the jet array

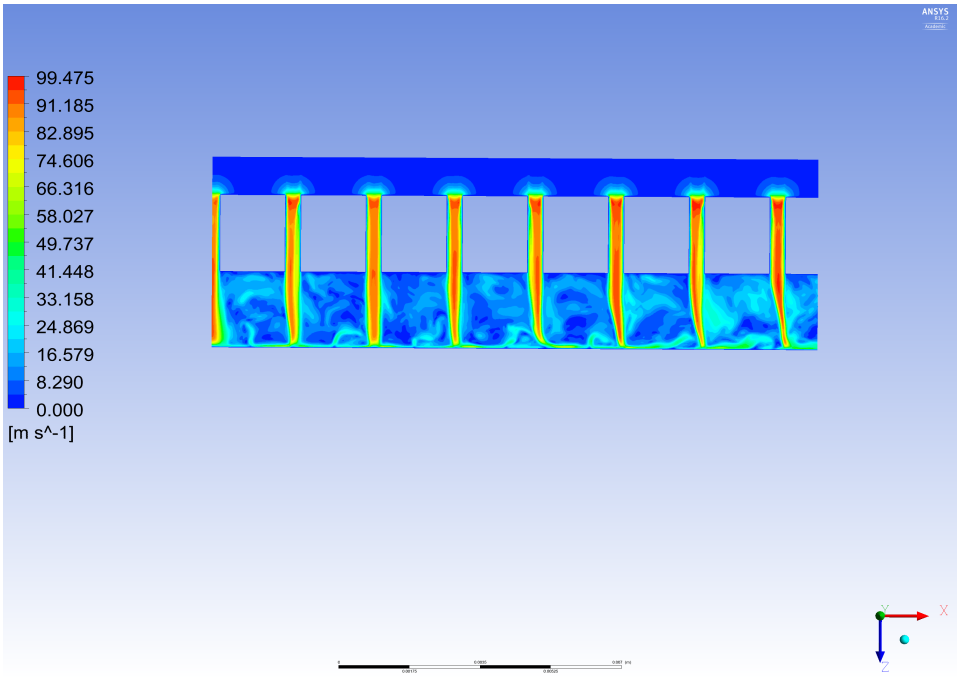

Figure 4.6: Instantaneous velocity field of the jets impinging for the first time

Natural instabilities such as Kelvin- Helmholtz type of instabilities starts to develop in the initial shear layer forming trains of vortex rings. They coalesce with neighboring rings which leads to the formation of large-scale structures as cited in [Yule, 1978]. Figure 4.7 shows the coalescence of vortex rings in the shear layer of a jet. The distance between them increases with increase in the distance from the nozzle exit. The low- pressure regions in the instantaneous pressure field, visible in figure 4.8, indicate the eddy positions in the initial shear layer. Further downstream, there is growth in low-pressure regions, combined with an increase of the scales of the ring vortices.

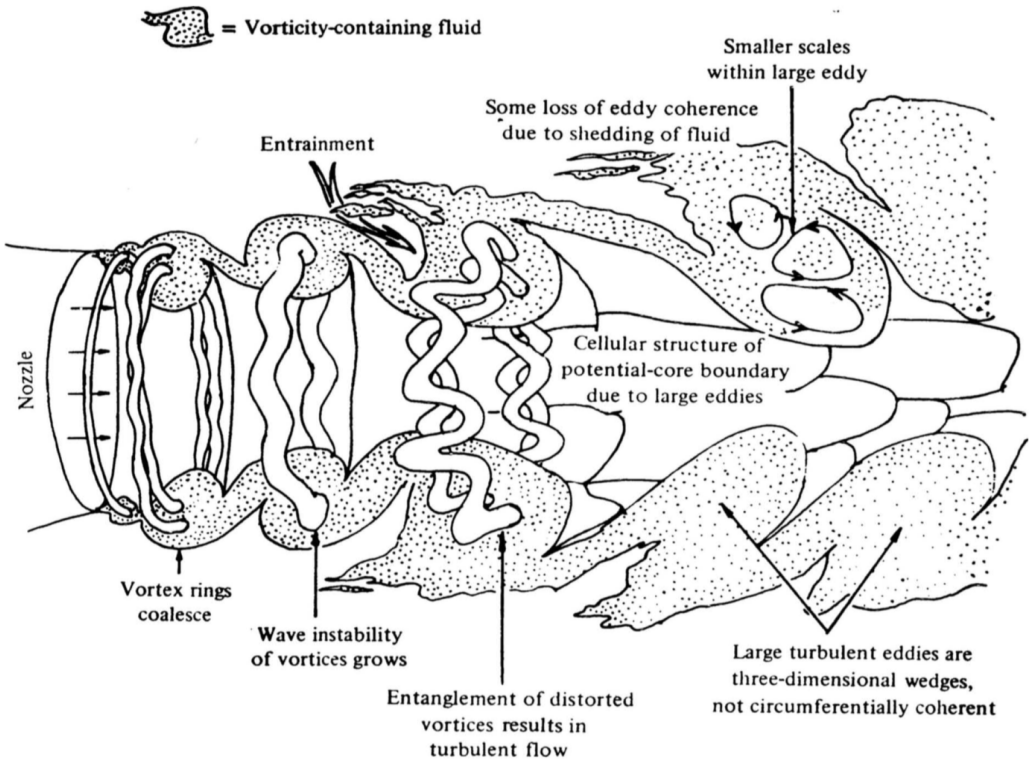

Figure 4.7: Coalescence of vortex rings in the shear layer of a jet [Yule, 1978]

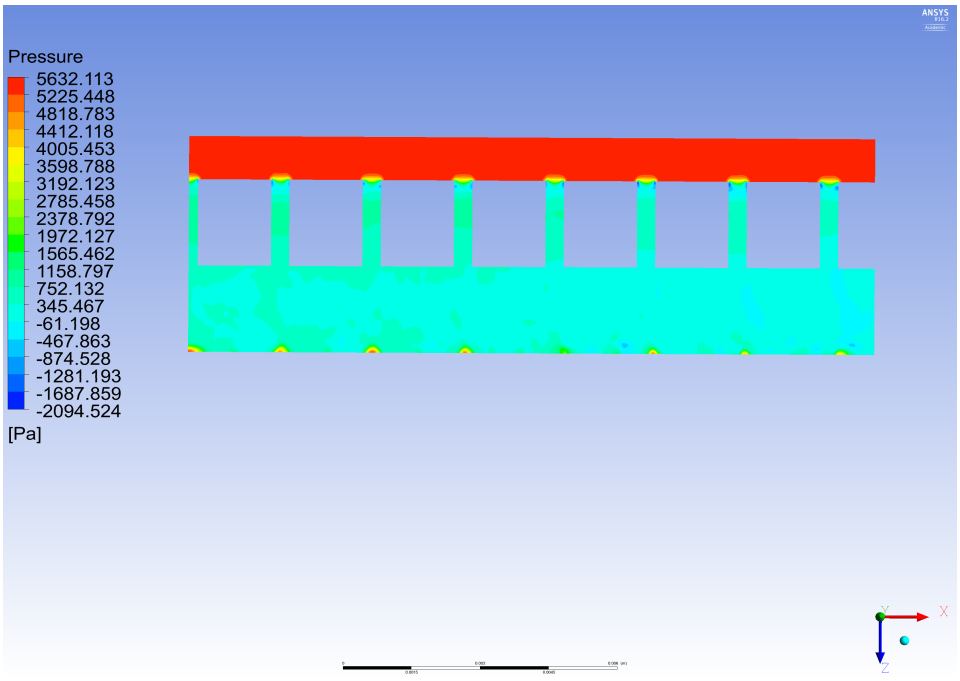

Figure 4.8: Pressure field with in the channel

Figure 4.8, shows the instantaneous pressure field characterized by the increase in static pressure at the stagnation region. It is also observed that the upper layers of wall jet starts to interact with the cross flow by forming vortices. Further downstream, due to the increase in fluid velocity in the nozzles and increased interactions of spent air with the jets forms a low pressure region inside the channel. Figure 4.9 shows the

iso-surfaces of low pressure regions colored by Normalized Q criterion.

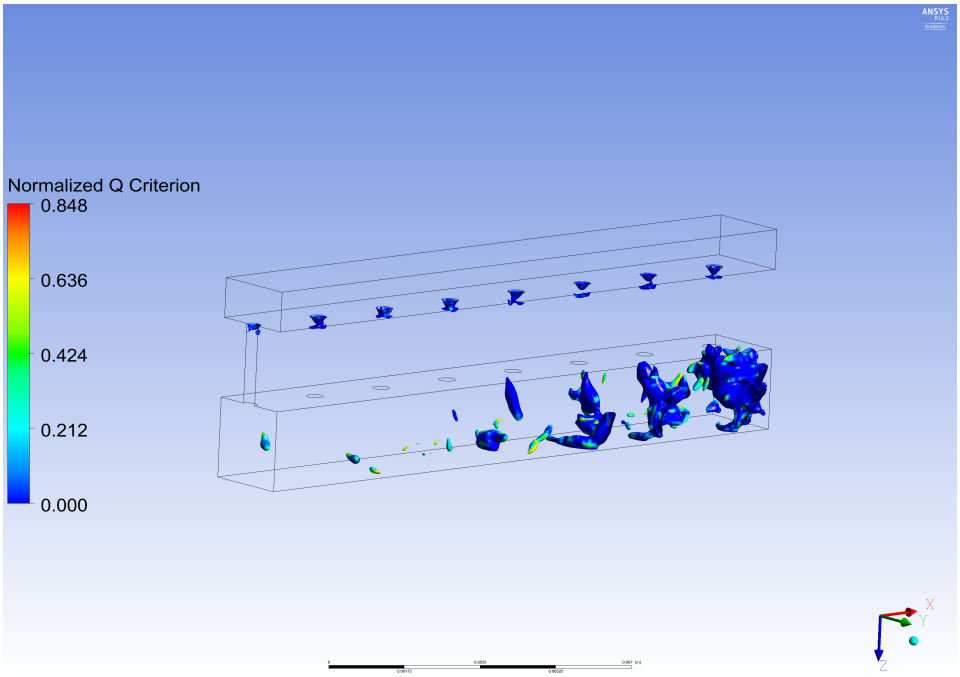

Figure 4.9: Iso-surfaces of pressure colored by normalized Q criterion

The stress fields start losing its similarity within the channel due to the instabilities. It was observed that, due to instabilities in the shear layer, the total vorticity magnitude of the first three jets exhibits a curly structure but for the last few jets, due to the cross flow effects, the symmetrical curly structure is not seen anymore. Figure 4.10 and 4.11 shows the vorticity structure of first and last jet. This phenomenon of wavy vortical structure is previously observed in a single round jet by [Uddin *et al.*, 2013]. In the near wall region, it was detected that the stagnation region is characterized by positive and negative Q - criterion values which indicates that the flow is dominated by rotational effects if Q is positive, while the negative values indicate low rotational effects. This abnormality makes the flow complex and difficult to predict at the stagnation region. Nearby the nozzle exit, at $Z/D = 1.5$, the instantaneous vorticity magnitude field shows that instabilities are present in small regions, but further downstream, near to the stagnation region, at $Z/D = 3.5$, the vortex rings are subjected to high deformation causing the instabilities to hit the target plate.Figure 4.12 represents the iso-surfaces of normalized Q criterion colored by vorticity inside the cross flow domain.

With the impingement of instabilities on the target plate, the radial velocity increases locally. The interaction of the spent air with the jet, amplifies instabilities in the shear layer and increases the momentum transfer from the mean flow into the turbulent stresses. In the impinging region, the presence of high static pressure and wall-blocking effect produces high turbulent stresses which makes the flow structures difficult to understand. Also, the stagnation region is influenced by large coherent structures from the shear layers. The primary vortices generated from the upwash flow in the wall-jet region, combined with the impact of eddy structures from the jet could be the reason for the deformation of these instabilities.

With the impingement of instabilities on the target plate, the radial velocity increases locally. The interaction of the spent air with the jet, amplifies instabilities in the shear layer and increases the momentum transfer from the mean flow into the turbulent stresses. In the impinging region, the presence of high static pressure and wall-blocking effect produces high turbulent stresses which makes the flow structures difficult to understand. Also, the stagnation region is influenced by large coherent structures from the shear layers. The primary vortices generated from the upwash flow in the wall-jet region, combined with the impact of eddy structures from the jet could be the reason for the deformation of these instabilities.

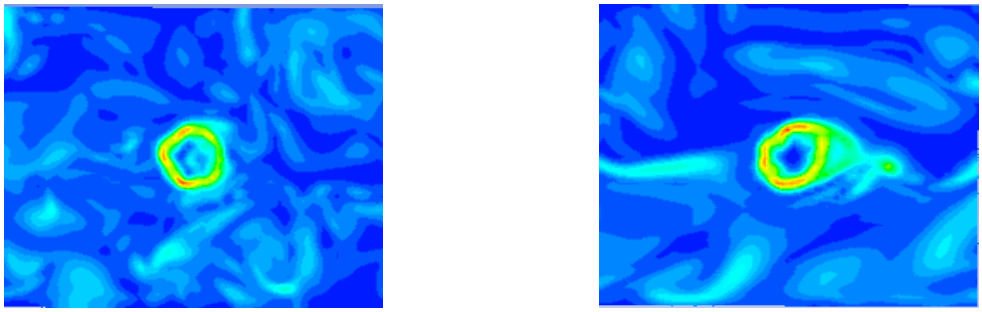

Figure 4.10: Vortex instabilities structure at $Z/D = 1.5$

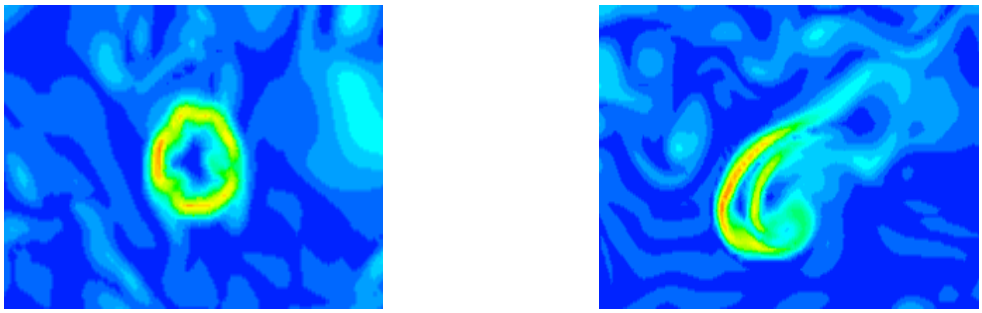

Figure 4.11: Vortex instabilities structure at $Z/D = 3.5$

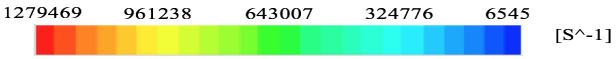

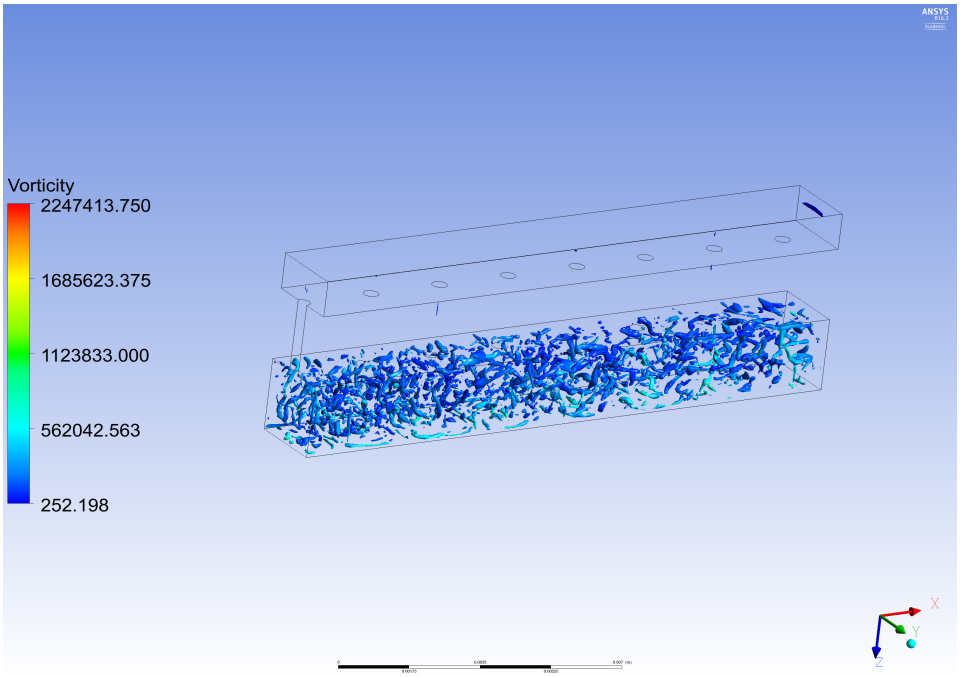

Figure 4.12: Iso-surfaces of normalized Q criterion colored by vorticity.

At the position of Z/D = 1, due to the presence of the wall, the mean flow experiences a strong deflection in the flow. At this stage, the axial velocity at the wall becomes zero where as, the radial velocity starts to increase until it reaches the position where boundary layer is formed. The velocity fluctuations, due to the

blockage effect starts to decrease at the wall. With the interactions between the cross flow, wall jets and the shear layer being strong at certain radial distance from the stagnation point, a strong turbulence anisotropy is identified in the near wall region at a radial distance of $0.5 < r/D < 1$.

As the jet approaches the target surface, the jets starts to decelerate. The stagnation region is formed where the jet centre impacts the target surface and this region is characterized by high values of the static pressure with strong curvature of streamlines and rotational effects caused by the wall. The high static pressure increases as the turbulent normal stress and axial momentum decreases. It is observed from the turbulent kinetic energy field, that the maximum 'k' occurs in the wall-jet region and the jet shear layer. After the turbulence level becomes low in the stagnation region, it recovers in the wall-jet region. The increase of the turbulence level is most likely connected to the acceleration and deceleration of the flow and the interaction with the large coherent structures in the boundary layer.

The budgets of turbulent kinetic energy and normal stresses in stagnation region were also analyzed. it was observed that the turbulent kinetic energy production term is negative close to the wall due to the pressure diffusion. Near the wall, the budget for $\overline{ww}$ is dominated by the pressure diffusion. This pressure is given to $\overline{ww}$ and subsequently changes sign and transfers to $\overline{uu}$ and $\overline{vv}$. The level of dissipation in the budgets reveals a strong anisotropy of the stagnation-region turbulence. At the position $r/D = 0.5$, the turbulent kinetic energy budget is again dominated by a negative production that is balanced by the pressure diffusion. It can be concluded that due to pressure diffusion, turbulent kinetic energy is transported from the stagnation region to the outside. The high levels of pressure-strain and pressure diffusion reflects the presence of strong pressure fluctuations and their interaction with the velocity field. Figure 4.13 and 4.14 shows the strain rate of the fluid in the shear flow and on the impinging plate. It is observed that the fluid undergoes high strain rate at the nozzle inlet due to contraction effect. It is also seen that the strain rate appears in the shear flow due to the deformation of the fluid. On the target surface due to strong pressure fluctuations, the strain rate dominance can be clearly seen.

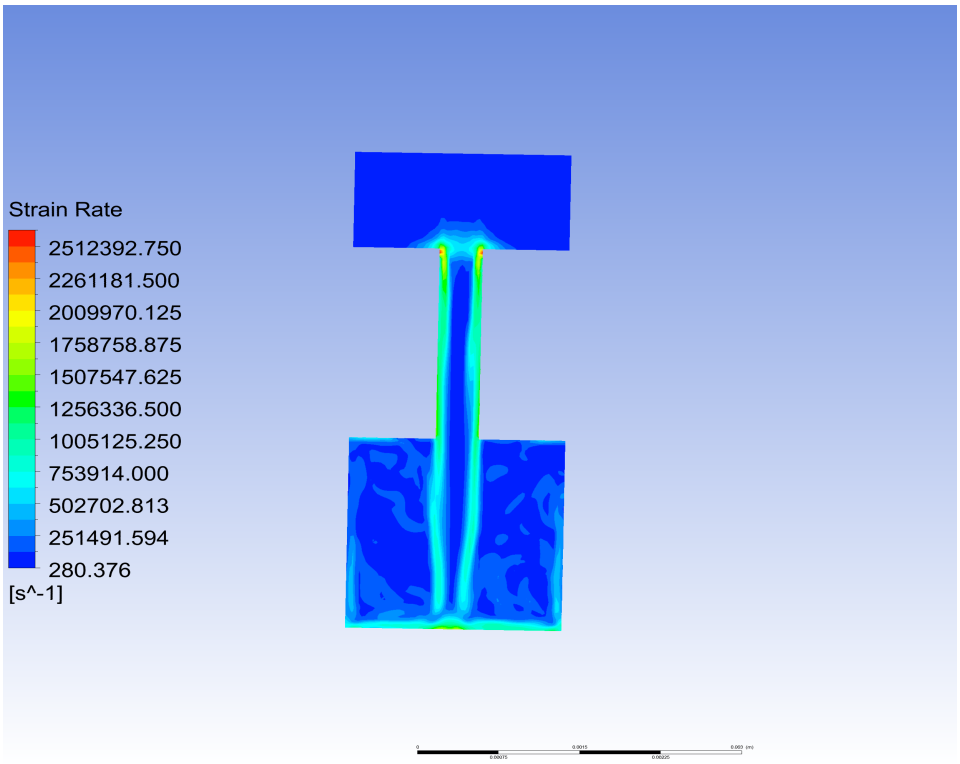

Figure 4.13: Strain rate in the impinging flow

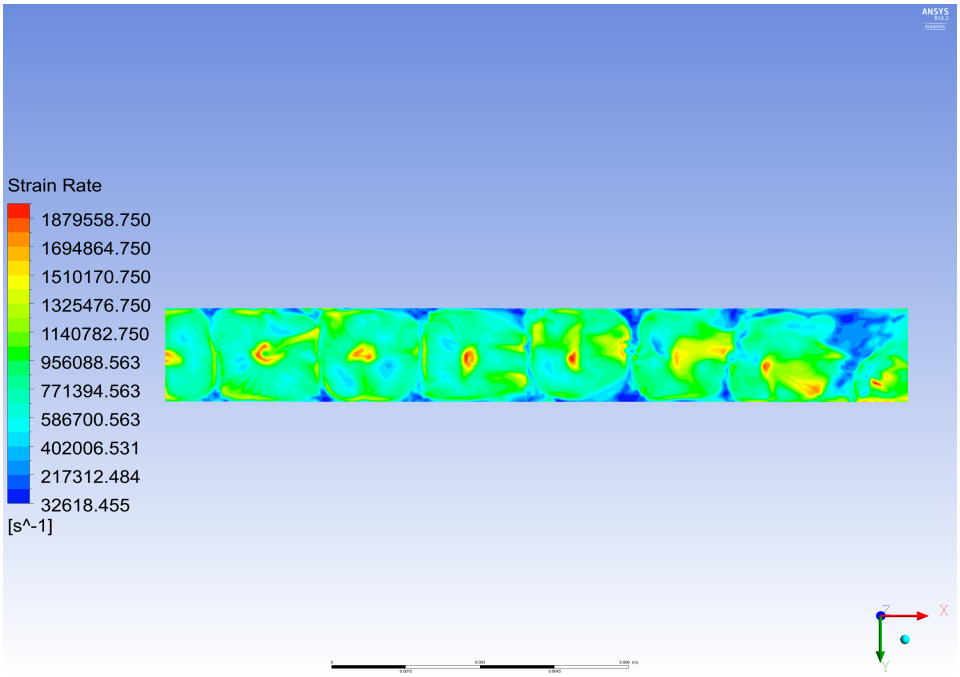

Figure 4.14: Strain rate on the impinging plate

In the wall-jet region, at the position $r/D = 1.0$, the turbulent kinetic energy is characterized by a peak in production term in the boundary layer. In this region, almost all of the produced kinetic energy is convected downstream. Further downstream, at the position $r/D = 2.0$, the turbulent kinetic energy production term is reduced reflecting the deceleration of the wall-jet. This positive contribution of turbulent energy is also due to the pressure diffusion and turbulent transport. These positive terms are balanced entirely by the dissipation. Figure 4.15 shows the wall shear stress distribution on the impinging plate. It is observed that at the stagnation point the wall shear stress is close to zero which is expected as the shear stress distribution should gradually increase with increase in radial distance. At $r/D = 1.0$, the wall shear distribution reaches a peak value and then gradually reduces with increase in the radial distance. Due to the interaction between the accelerated wall jet and mixing shear layer, the wall shear stress produces a high value at $r/D = 1.0$.

The distribution of instantaneous surface temperature is shown in figure 4.16 below. Due to the high heat transfer rate at the stagnation point, the temperature is low at the stagnation point. The heat transfer distribution is also similar to the temperature profile, but the only difference is the contour profile. As the Nusselt number is inversely proportional to the temperature difference, the contours look the opposite but the distribution looks the same. The region of high heat-transfer coefficient is not circular, but looks stretched in few directions. These oval shapes indicate stretching of the flow structures in the direction of large coherent structures. This proves the assumption that the temperature fluctuations in the stagnation region are determined by the impingement of the large coherent structures from shear layer. However, this effect can not be concluded by considering just the effect of flow stretching due to shear layer. As the channel also is characterized by the cross flow and due to the continuous interaction of the cross flow with the jets, this flow stretching can also be due to the interactions of cross flow with the mixing layer of the jet.

An interesting flow phenomenon of this particular jet configuration is the osscilation of downstream jets due to the effect of cross flow. due to the increase in cross flow, the last three jets begin to oscillate which results in shifting of the actual impinging region. This anomaly is shown in figure 4.17 and 4.18 and this phenomenon is cyclic in nature through out the flow time. The jets, when initially impinged follows a symmetrical profile as shown in figure 4.16 but, when the cross flow velocity becomes dominant, the spent air from the upstream jets starts to affect the downstream jets. This effect causes the downstream jets to oscillate from their actual impinging region. As shown from the figures 4.17 and 4.18, the downstream jets shifts their stagnation region towards top and bottom side of the channel.

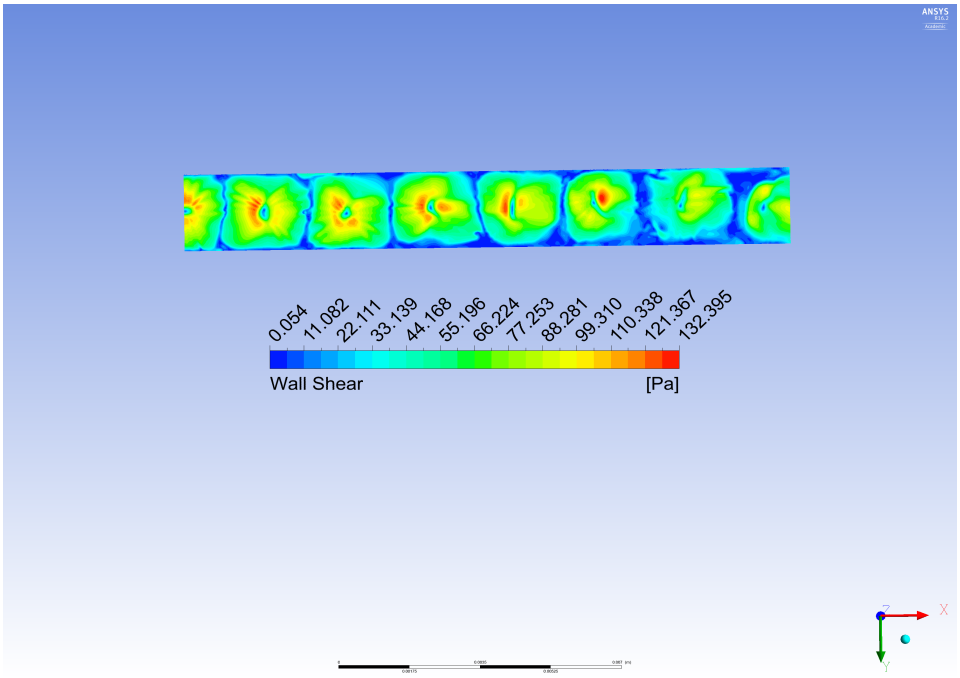

Figure 4.15: Wall shear stress contour on the impinging plate

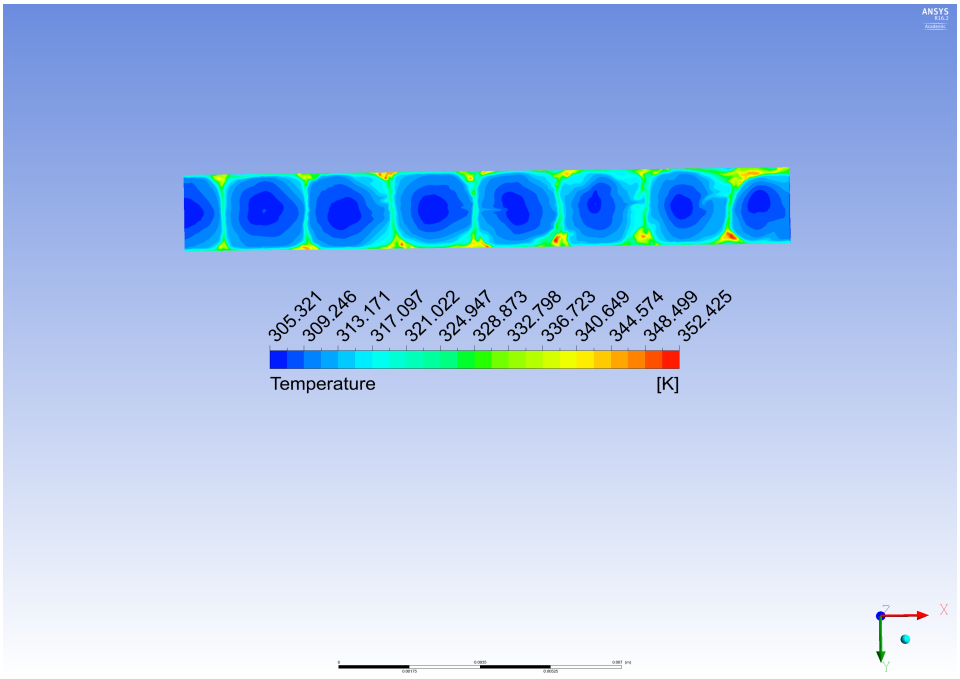

Figure 4.16: Instantaneous temperature contour on the impinging plate

Figure 4.19 shows the radial distribution of Nusselt number for the upstream jets. It can be seen from the figure that the distribution is not symmetrical and this tendency is observed for all upstream jets. At X/D = -0.75 to -1.25. Most of the upstream jets exhibits a kink in their distribution. This is due to the fact that the primary vortices and the upwash from the upstream jets produce a surface renewal effect which results in enhancing the heat transfer rate. This effect was explained by [Kataoka, 1990] and this effect has been observed in previous studies. However, it is also evident that this effect is still valid in laminar regime. Figure 4.20 represents the radial distribution of Nusselt number for the last jet, it can be seen that the stagnation region is shifted to X/D = 0.5. It was also noticed that the wall jet from the upstream jet decays near X/D= -2

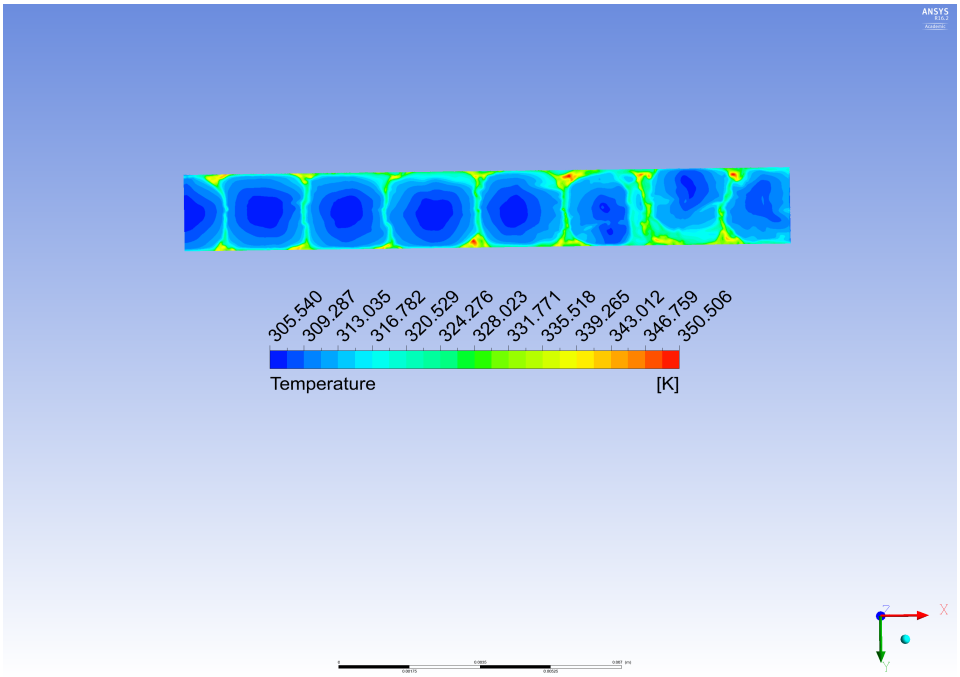

Figure 4.17: Instantaneous temperature contour on the impinging plate showing jet oscillations

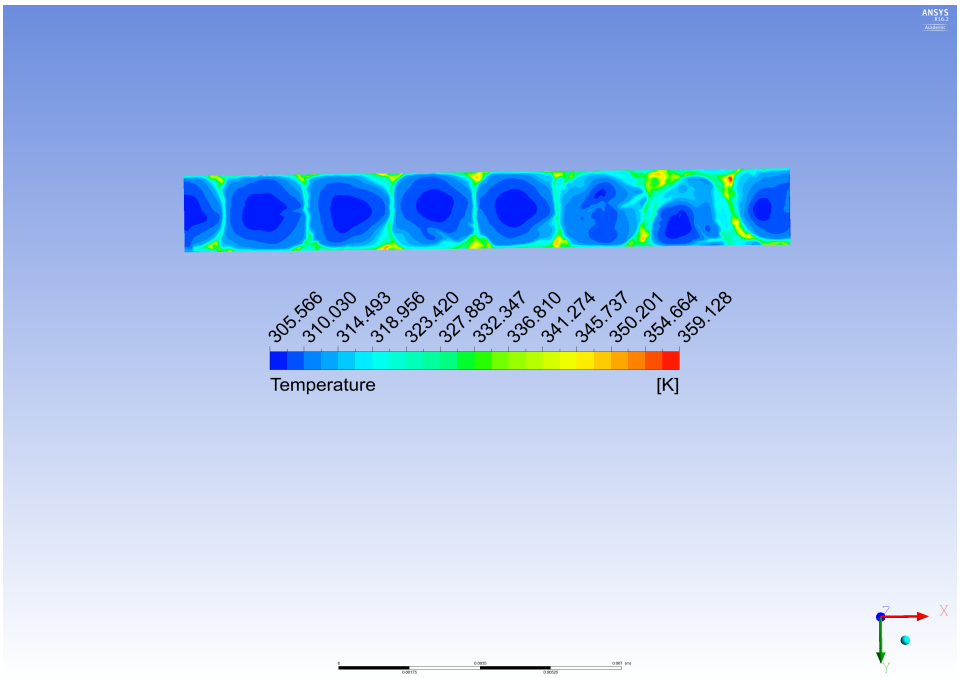

Figure 4.18: Instantaneous temperature contour on the impinging plate showing jet oscillations

and therefore there is a substantial drop in Nusselt number at X/D = -1.5.

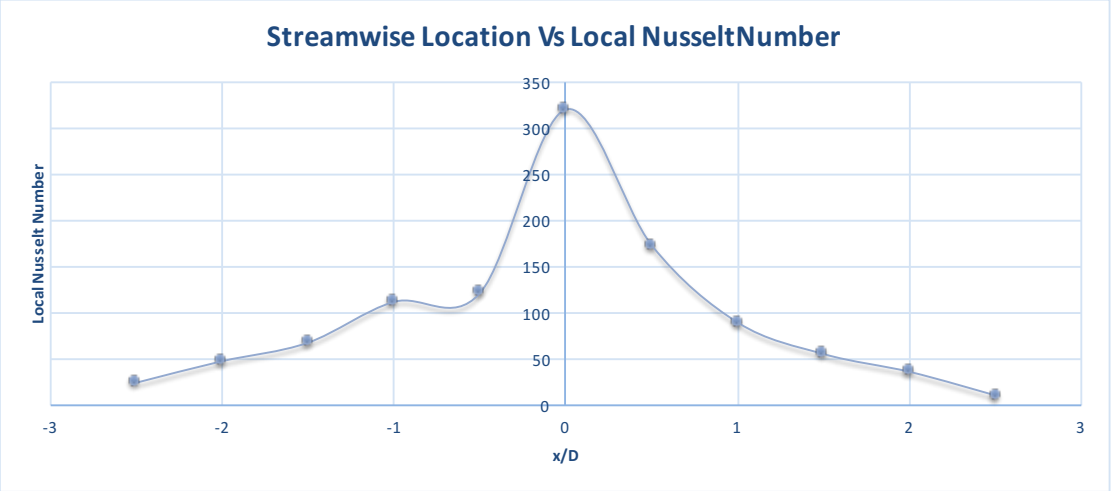

Figure 4.19: Radial distribution of Nusselt number for the first jet from LES

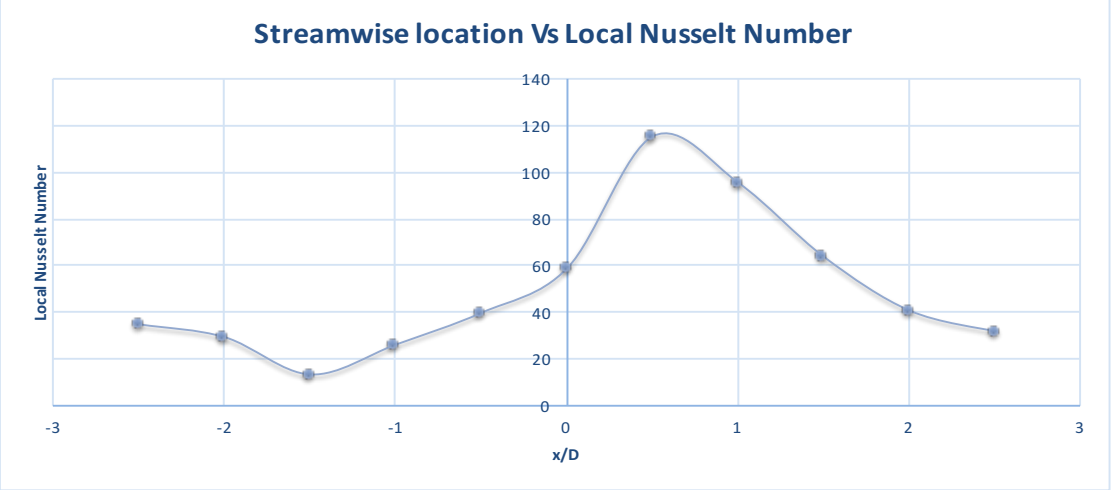

Figure 4.20: Radial distribution of Nusselt number for the last jet from LES

Figure 4.21 shows the comparison of local Nusselt number of the jets in a streamwise array. It is observed that the curve follows a similar profile for the both cases but prediction of Nusselt numbers through LES approach is more accurate than RANS simulations. However, the average Nusselt number for both cases remains approximately same. The possible reason for this difference could be due to the prediction of jet centre line velocities in both the cases. Furthermore, both LES and RANS simulations predicted that the third jet produces highest local heat transfer coefficient. Furthermore, it is also noticed that the instantaneous and mean fields are predicted better in LES, while in RANS the Navier – Stokes equations are time averaged.

LES simulations of the multiple impinging jets for $Re = 1625$ and nozzle-to- plate-distance $Z/D = 5$ provided detailed information on the flow field and heat transfer characteristics of a multiple jet array. This information is used to study the velocity, temperature, turbulence fields, dynamics of coherent vortical structures and their relationship to the thermal field on the impingement surface. As the jet leaves the nozzle exit, it is affected by the entrainment, cross flow and the newly formed jet-shear layer grows and spreads instabilities to the centre, followed by the increase of the turbulent kinetic energy in the shear layer. Further downstream, the wall impermeability starts to affect the velocity and stress fields causing them to decrease which results in the increase of the static pressure. In the wall vicinity, part of the turbulent kinetic energy is transported back to the mean flow. The occurrence of negative production of the turbulence energy in the stagnation region, earlier detected by experiments, is confirmed by the present LES. Due to the wall obstacle, the flow

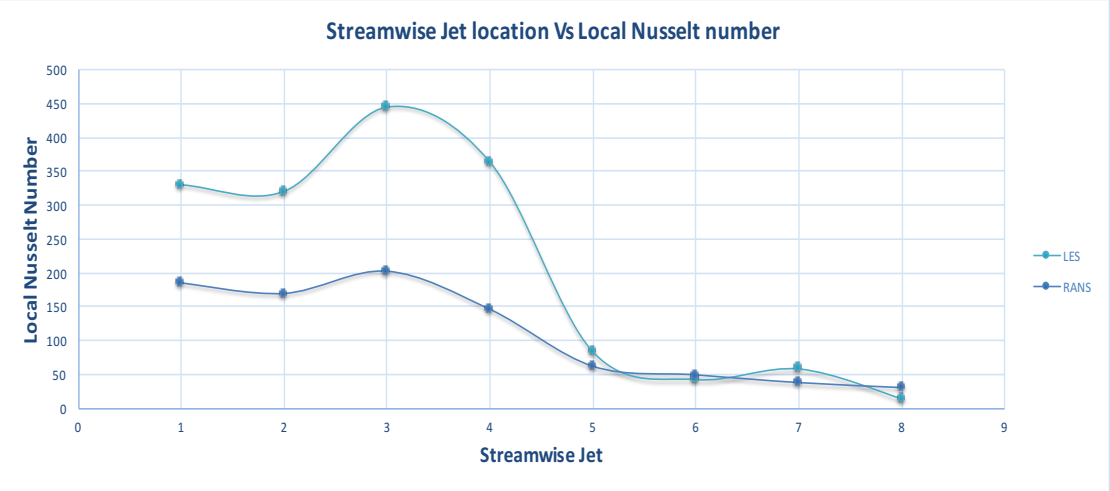

Figure 4.21: Comparison of local Nusselt number - LES Vs RANS

deflects forming a wall-jet. The wall-jet first strongly accelerates and then starts to collide with neighboring wall jets which results in the formation of primary vortices due to the forceful bending created by the cross flow producing and higher level of turbulence. It was observed that the third jet produced higher local heat transfer rates than the other jets due to the effect of cross flow. The enhancement of heat transfer rates at a certain amount of cross flow is earlier investigated in few experimental studies and it can be confirmed from the present simulations. After the flow reached statistically stable state, it was observed that the downstream jets oscillates due to the cross flow effect. This results in an improper distribution of Nusselt number on the impinging plate.

5

SENSITIVITY ANALYSIS ON THE GEOMETRICAL PARAMETERS

The current chapter presents an overview on the sensitivity analysis performed on the multiple jet impingement array to analyze the effect of manufacturing tolerances. It is important to understand the effect of geometrical parameters on the system design and how they influences the heat transfer and pressure drop characteristics of the multiple impinging jet array. In section 1.1, the effect of nozzle to plate distance is analyzed by varying the height between the nozzle exit and the target surface, followed by section 1.2 which discusses the effect of nozzle diameter on the impinging system. In this section, few interesting findings are achieved with respect to the flow phenomenon. In section 1.3, the effect of clogged jet on the impingement system is analyzed by clogging the jet which produces highest local heat transfer rates.

Manufacturing jet impingement system is a complex task. It requires a lot of precision to drill the holes and join the impinging plate at the correct location. Therefore, it is quite important to study these effects on the system design and investigate how various geometrical parameters can influence the heat transfer and pressure drop characteristics of the multiple jet impingement system.

The main important geometrical parameters that affect the heat transfer coefficients is jet impingement are:

- Impinging plate distance to the hole diameter (Z/D)
- Array configuration
- Reynolds number
- Hole geometry
- Inter-jet spacing
- Target surface geometry and
- Jet angle

In the present work, since the array configuration is already chosen as inline configuration, the dependency of this parameter on the system design is not considered. Also, numerical investigations in the current study has been done for a range of Reynolds numbers in the laminar regime and hence, the effect of Reynolds number has been already dealt in the previous chapters. It is also highly impossible that the nozzles are inclined. By eliminating various parameters, the design parameters are narrowed down to three parameters. They are: distance between the nozzle exit and impinging plate (Z/D), hole geometry and target surface geometry.

It was observed from the literature, many works have been performed on analyzing the effect of target plate distance, hole diameter and target surface geometry, but there is a scarcity of information regarding the effect of these parameters on the manufacturing tolerances of impinging system.

5.1. EFFECT OF NOZZLE-TO-PLATE DISTANCE

To investigate the discrepancy in the results, a detailed study has been performed to determine the effect of target plate distance on the heat transfer and pressure drop characteristics of the jet impingement system. Five cases were analyzed by changing the Z/D ratio to ± 0.5 from the reference value of 5. Figure 5.1 shows the velocity field for the Z/D ratio of 4.5.

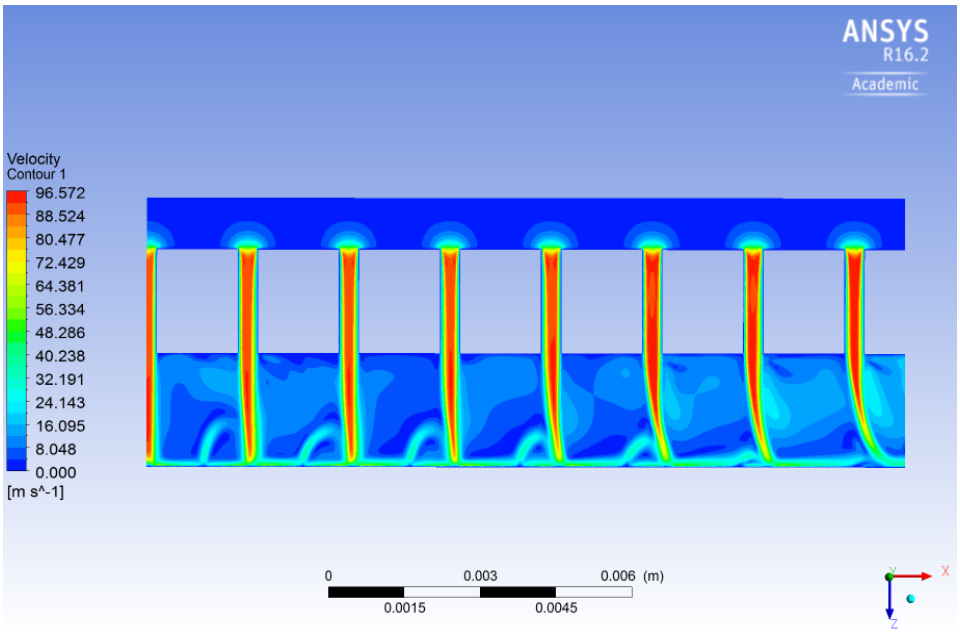

Figure 5.1: Velocity field for Z/D = 4.5

It can be seen from the figure that velocity magnitude in the downstream jets has increased when compared to the reference case. This increase in velocity can be attributed to the drop of static pressure inside the nozzles. Furthermore, it is also observed that the cross flow in the channel has increased which results in increased pressure drop inside the channel. when both the cases are compared in terms of static pressure drop, figure 5.2 shows that, for Z/D = 4.5, the pressure drop inside the channel is relatively more than the reference case as shown in figure 3.5. However, it was observed that there is no change in total pressure drop from both the cases. For Z/D = 5.5, it was found that, due to the increase in the channels cross section area, the cross flow velocity is decreased and therefore the static pressure map inside the channel is similar to the reference case. Furthermore, no significant changes were found in terms of total pressure drop. Therefore, it is believed that, with the change in target plate distance from the nozzle exit, the pressure drop characteristics are insensitive to the minor change in the Z/D ratio and remain the same as the reference case.

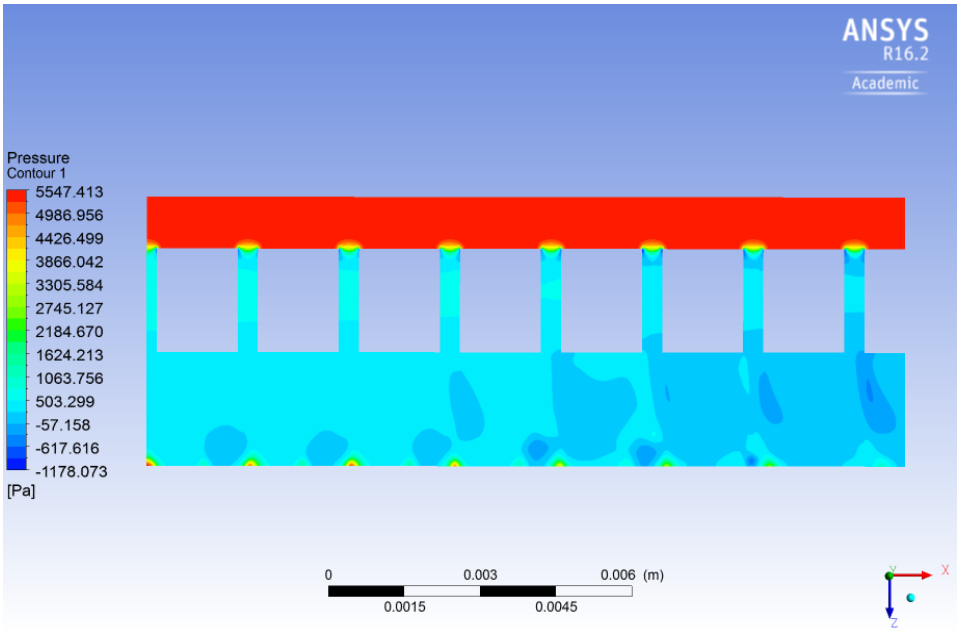

Figure 5.2: Pressure map for Z/D = 4.5

However, in terms of heat transfer characteristics, a minor change was observed with respect to the average Nusselt number. It was found out that the average Nusselt number is increased with the decrease in Z/D ratio by 3.8% where as, the heat transfer rate drops when the distance is increased to Z/D = 5.5 by 3.5%. Table 5.1 shows the variation of plate temperature and total pressure at the inlet and outlet.

Table 5.1: Effect of Z/D on the 0.4 mm jet array

Z/D	**Plate Temperature** [K]	**Change in Nusselt number** [%]	**Inlet Pressure** [Pa]	**Outlet Pressure** [pa]	**Change in Pressure drop** [%]
4.5	315.20	+ 3.8	5485.60	277.50	+ 0.15
4.75	315.65	+ 2.1	5460.25	260.33	+ 0.003
5	316.20	-	5435.18	233.32	-
5.25	316.42	- 1.5	5418.69	215.53	- 0.01
5.5	316.85	- 3.5	5395.96	199.66	- 0.08

Figure 5.3 shows the distribution of temperature profile on the impingement plate. From the figure it was observed that no significant change in the distribution of temperature profile. However, due to the increased cross flow velocity, the down stream jets shows few minor changes in the profile which shows the increased effect of cross flow.

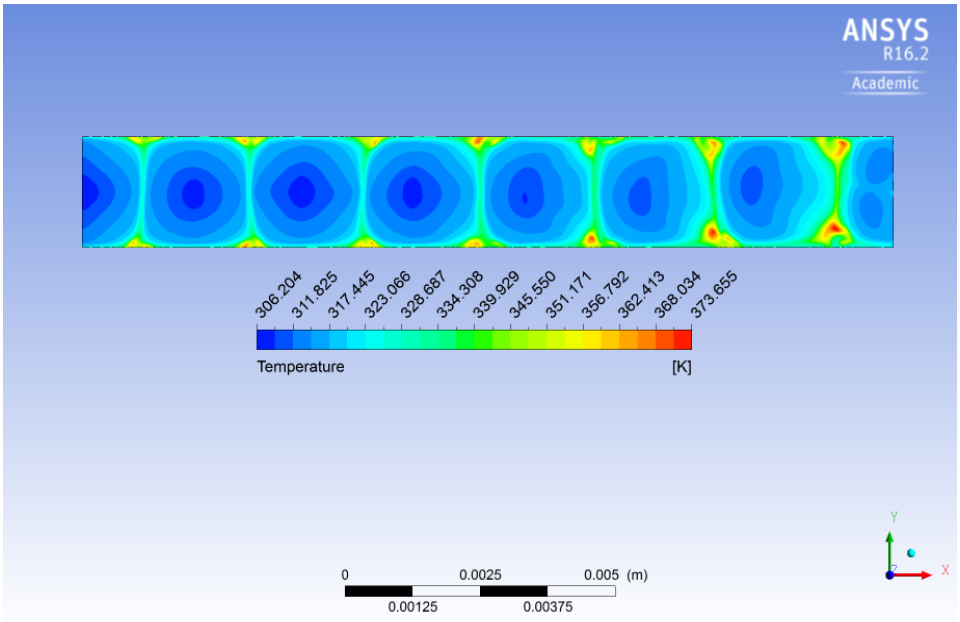

Figure 5.3: Temperature profile map for Z/D = 4.5

5.2. EFFECT OF HOLE DIAMETER

As discussed earlier, the other important geometrical parameter is the effect of hole diameter on the impingement system. It is quite a challenging task to manufacture 0.4mm jet array as it involves lot of precision. Many researches in the past have studied the effects of hole geometry on the impinging system.[Whelan and Robinson, 2008] investigated Various inlet and outlet geometries of the jet nozzles to determining an optimal configuration in which heat transfer to the impinging jets is maximized for a minimal pumping power requirement. [Florscheutz and Tseng, 1985] studied the effect of non-uniform geometries on the jet impingement system. However, it was found that there is inadequate information on the effect of manufacturing tolerances of the hole diameter.

Hence, the current study involves detailed investigation to study the effects of hole diameter. Several simulations were performed by changing the nozzle diameter of third and fourth jet in the array. The reason for selecting third jet is because of its high local heat transfer rate than the other jets in the array. So disturbing this jet would affect the system performance. By keeping the manufacturing tolerance as the criteria, the nozzle diameters are changed by ± 0.01 mm. It was observed that such a small change in the diameter of the jet affects the pressure drop of the system. Changing the diameter of the jet by ± 0.01 mm shows a difference of 8% in the pressure drop of the system. However, the average heat transfer coefficient of the system is insensitive to the change in diameter. Furthermore, a simulation was performed by changing the jet diameter of all jets by ± 0.01 mm. It was observed that the change in pressure drop is significantly high which implies that ΔP is extremely sensitive to the change in nozzle diameter.

Figures 5.4 and 5.5 shows the variation of local Nusselt number by changing the hole diameter by D + 0.01 mm and D - 0.01 mm respectively. It was observed that, by increasing the jet diameter, the velocities in the jet axis line are relatively low than the reference case, but when the diameter is decreased, due to the smaller diameter, the velocities in the jet centre line are increased. This phenomenon resulted in the lower heat transfer coefficients of the third jet for D + 0.01 mm case.

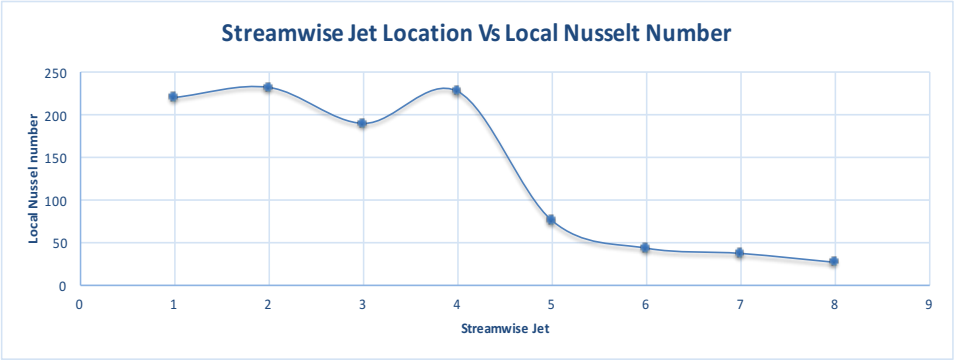

Figure 5.4: Variation of local Nusselt number along the streamwise direction for D + 0.01 mm

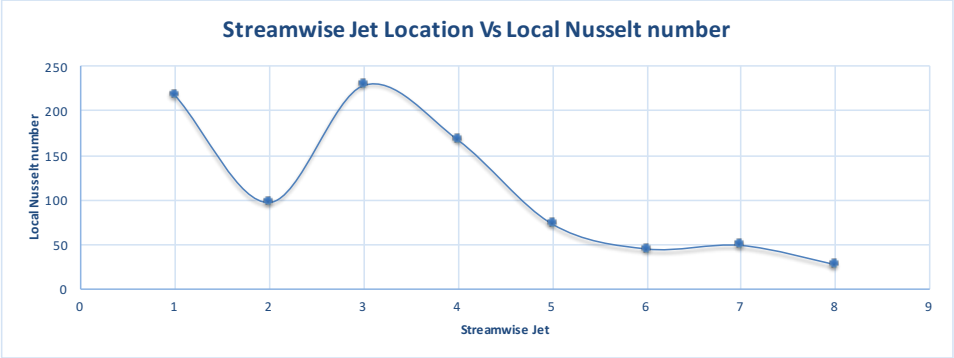

Figure 5.5: Variation of local Nusselt number along the streamwise direction for D - 0.01 mm

The velocity fields for D±0.01 mm case is shown in figures 5.6 and 5.7. From the figures, it is evident that the jet profiles in the third and fourth jet exhibits minor difference with respect to the velocity magnitude inside the jets.

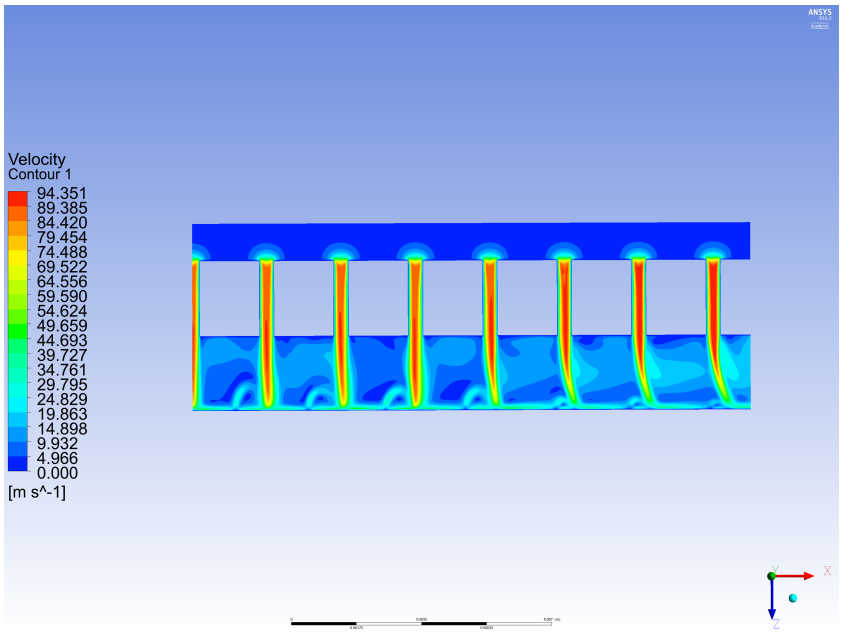

Figure 5.6: Velocity field contour for D + 0.01 mm

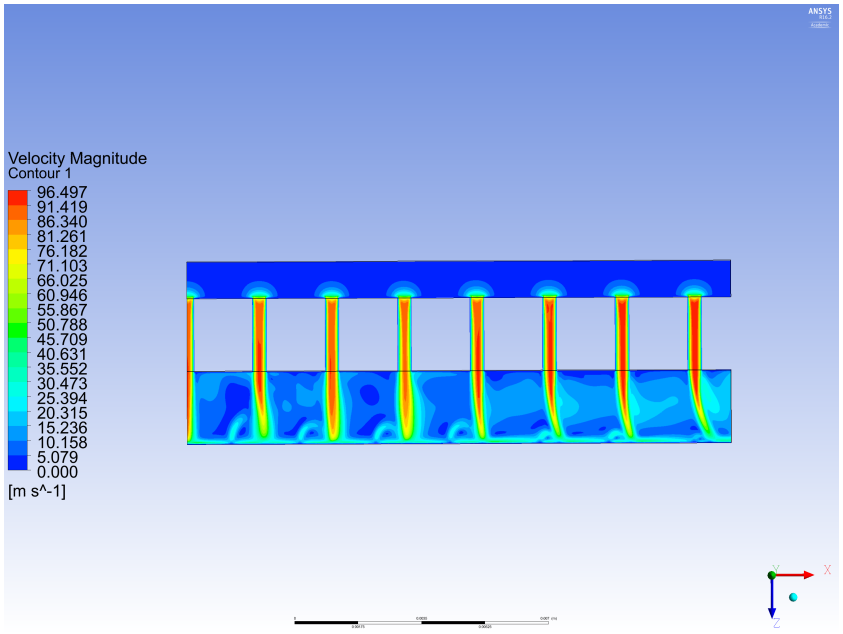

Figure 5.7: Velocity field contour for D - 0.01 mm

From the temperature contour of D - 0.01 mm case, it is observed that due to the increased velocity in the third and fourth jet, the spreading of the jet from the third jet is more than the normal reference case. Figure 5.8 shows the higher spreading of the third jet due to the increased velocities. It is also observed that due to the more spreading of the third jet, the second jet is affected and there is a shift in impingement region of the second jet. This could have been the reason for lower local Nusselt number for the second jet in Figure 5.5.

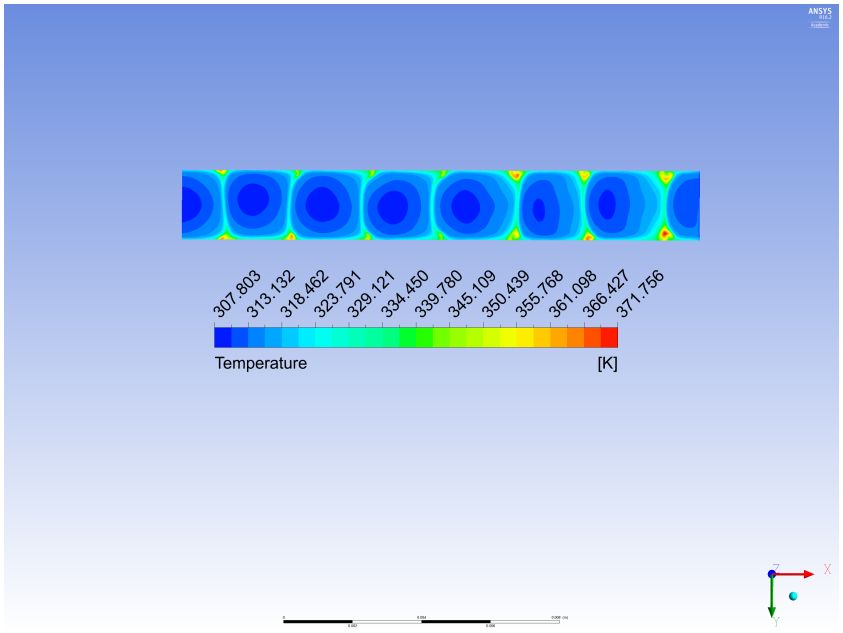

Figure 5.8: Temperature distribution for D - 0.01 mm

Furthermore, a simulation was performed by changing the jet diameter of all jets by ± 0.01 mm. It was observed that the change in pressure drop varies significantly when compared to the reference case. Table 5.2 shows the results of jet diameter effect on the pressure drop and heat transfer characteristics of the impinging array. The results from CFD simulations is taken as reference value for validating the results from the sensitivity analysis.

Table 5.2: Effect of hole diameter on the 0.4 mm jet array

Nozzle diameter [mm]	**Jet number**	**Change in pressure drop** [%]	**Change in Nusselt number** [%]
D + 0.01	All jets	- 35	+ - 2
D + 0.01	3rd and 4th jet	- 8	- 0.5
D - 0.01	3rd and 4th jet	+ 8	+ 0.5
D + 0.1	3rd and 4th jet	- 38	- 6
D - 0.1	3rd and 4th jet	+ 38	+ 6

5.3. CLOGGED JET

This section presents with a computational investigation performed to study the effect of clogged jet on the multiple impinging jet array. In the manufacturing process, there is a probability that one of the jets can be clogged. Therefore, to investigate the effect of clogging on the impinging array, a single jet was clogged out of 7.5 jets. To investigate the maximum effect, the third jet in the array is made to clog because, the third jet in the computational domain produces high local heat transfer coefficient. Figure 5.9 shows the velocity field in the array when a jet is clogged.

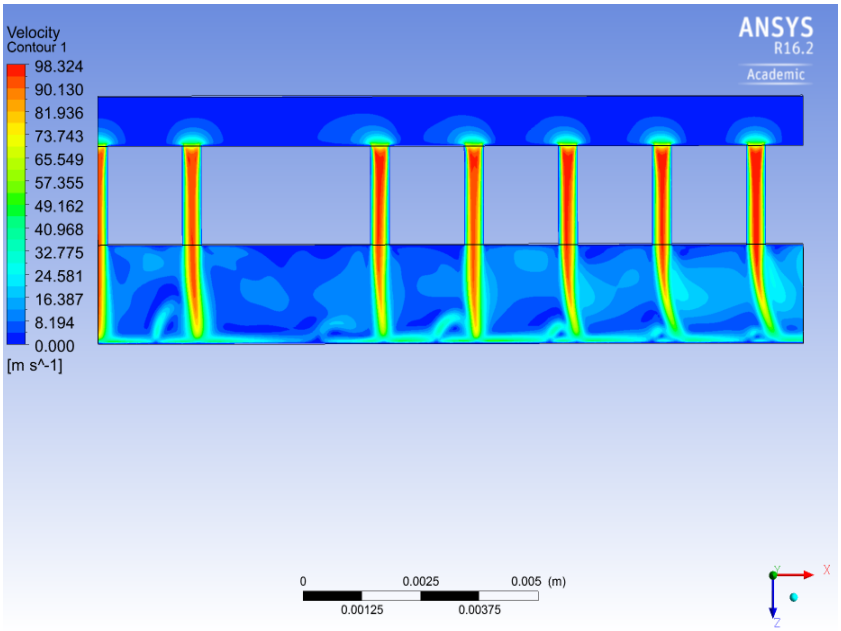

Figure 5.9: Velocity field map for a clogged jet

From the figure 5.9, it is observed that due to the absence of third jet, both the wall jets from second and fourth jets are extended before they collide to form an upwash flow. It is also evident that the wall jet of second jet decays at $r/D = 5$. The temperature distribution on the impinging plate is shown in figure 5.10.

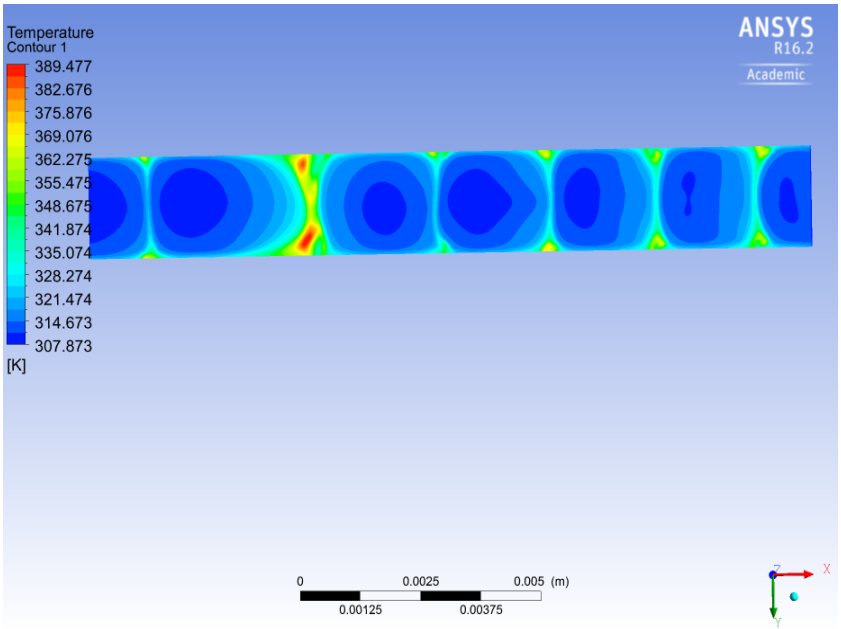

Figure 5.10: Temperature distribution on the impinging plate for a clogged jet

From the figure 5.10, it can be seen that, if a jet is clogged, the temperature distribution of an impinging array is significantly affected. As the wall jet starts to decay after certain radial distance, the temperature on the impinging surface increases rapidly affecting the uniform heat transfer distribution. This results in the formation of a thick thermal boundary layer between the second and fourth jet as shown in figure 5.11. The heat transfer and pressure drop results obtained from this simulation is validated with the results of 0.4 mm jet array which contains all jets. It was observed that by clogging the third jet, the average heat transfer coefficient drops by 6% and pressure drop is increase by 15%. Due to the non-uniform distribution of temperature on the impinging plate, the heat transfer characteristics of the array is affected significantly.

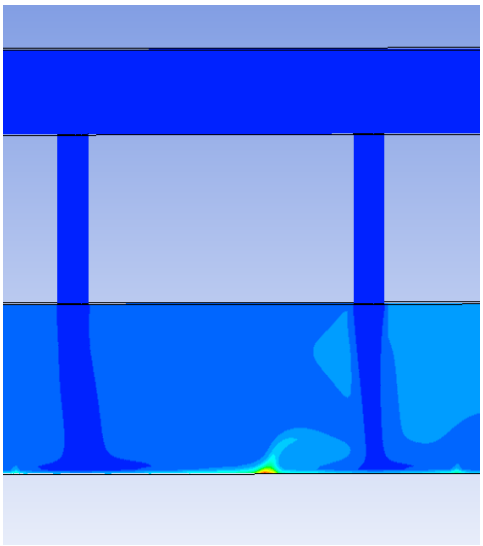

Figure 5.11: Development of thermal boundary layer in a clogged jet

The sensitivity analysis on the geometrical parameters of the multiple jet impingement system provided interesting flow phenomenon results that play a vital role in designing the jet array. Several CFD simulations were performed to study the effect of various geometrical parameters such as change in nozzle to plate distance (Z/D), change in nozzle diameter and the effect of clog jet. It was observed that, with a minor change in nozzle to plate distance (Z/D), the heat transfer characteristics are affected by ± 3%, while there was no significant change with respect to total pressure drop in the jet array.

However, with the change of jet diameter by ± 0.01 mm which is a manufacturing tolerance, the pressure drop characteristics of a jet array was affected significantly by ± 8%, but there was no significant change in terms of heat transfer characteristics. Therefore, it is quite important to manufacture the jet array with a lot of precision to accurately predict the flow phenomenon in an impinging array. Furthermore the effect of clog in any of the jets also plays an important role. The average heat transfer coefficient and total pressure drop of an impinging jet array can be affected upto 6% and 15% respectively by clogging a single jet. From the results, it was understood that, a lot of precision is involved in designing and manufacturing these jet arrays. Therefore, it is important to treat them with utmost importance.

6

CONCLUSIONS

The heat transfer and pressure drop characteristics of multiple impinging jet array in low Reynolds number regime have been studied with help of different numerical approaches such as RANS, URANS and LES. Flow features like cross flow, ring vortices and wall jet collisions adds on complexity to the flow. To understand the flow physics in laminar regime, numerical investigations were performed using CFD simulations and validated with the analytical and experimental results of [Rao *et al.*, 2010]. It is predicted that the results obtained from the present study will provide a greater insight into the flow physics of laminar impinging jet array.

- RANS simulations were performed to assess the capabilities of turbulence model in predicting the flow phenomenon and heat transfer characteristics of multiple impinging jet array. From the simulations, it was realized that, two models (SST $k-\omega$ and RSM model) were able to predict the heat transfer characteristics better than the other turbulence models. However, due to the high computation time required for RSM model, SST $k-\omega$ model was chosen to perform the simulations.
- The results from SST $k-\omega$ model over predicted the heat transfer and pressure drop characteristics in the array. Due to the strong turbulence anistorpies near the wall, the RANS models were not able to determine the flow physics accurately. However, RANS models would definitely act as a preliminary tool to understand the flow physics at a more basic level.
- To gain more insight on the flow characteristics, unsteady RANS simulations were conducted for the same impinging jet array at various Reynolds numbers. A time step of 1 X 10^{-4} was chosen and simulated for 4 flow through times. The results are validated with experimental results to determine the flow characteristics in real time scenario.
  - The heat transfer characteristics obtained from the CFD simulations compares well with the results of [Florscheutz *et al.*, 1981]
  - CFD results were found to predict the heat transfer characteristics accurately when validated with the experimental results. It was found that the CFD simulations over estimate the heat transfer coefficient by around 10%.
  - The non monotonic variation of the Nusselt number along the stream wise direction of the array is due to the interaction of the cross flow. It was found out that spent air enhances the heat transfer rate with medium cross flow. Further downstream, the cross flow effect dominates due to the increase in spent air velocity and therefore, the heat transfer distribution of the jet array is affected.
  - It was observed that the pressure drop characteristics from the CFD simulations over estimated significantly when validated with experimental results. However, these CFD results were found to determine the pressure drop values fairly well with the empirical correlations.

  - From the particle tracing method, it was noticed that the most of the pressure drop occurs due to the contraction effect at the nozzle inlet and the loss of kinetic energy in the nozzles.

- To investigate the potential of LES approach for complex flows and to extract the information of flow field, dynamics of instabilities and vortical coherent structures, a large eddy simulation was performed at $Re = 1625$.

  - It was observed from the LES that the cross flow affects the downstream impinging jets significantly. Furthermore, due to the increase in cross flow velocity, the downstream jets starts to oscillate by shifting the impingement regions on the target plate.
  - The primary vortex formed from the upwash of the wall jets and the shear layer instabilities from the jet coalesce at $X/D = -1$ to create a surface renewal effect on the impinging plate. This results in an enhancement of local heat transfer coefficient at $X/D = -1$.
  - The impinging wall impermeability starts to affect the velocity and stress fields causing them to decrease which results in the increase of the static pressure at the stagnation region.
  - The abrupt increase and decrease of Q criterion values at the stagnation region indicates that the flow possess strong anisotropies near the wall.
  - Due to the pressure diffusion it was observed that, the turbulent kinetic energy production term is negative near the wall.
  - The fluid undergoes high strain rate at the nozzle inlet due to contraction effect. Furthermore, high strain rates appears in the shear flow due to the deformation of the fluid.

- The sensitivity analysis on the effect of geometrical parameters proved that the pressure drop is sensitive to a minor change in the nozzle diameter. If the diameter of a jet is increased or decreased by 10 microns, the pressure drop of the system is affected by ± 5% - ± 35% depending on the number of jets.

- It was also found that with a minor change in Z/D, the heat transfer rate is affected by ± 3% and the pressure drop is insensitive (± 0.1%) to the Z/D difference .

- If a jet producing highest local heat transfer rate is clogged, the average heat transfer rate is decreased by 6 % and pressure drop is increased by 15%.

A

CALCULATION OF TIME-STEP

In large eddy simulations, the Navier - Stokes equations are solved by capturing the large eddies from the length scale of the geometry. Therefore, it is important to define the correct length and time scales to filter the eddies. The best way to define these length and time scale is through Kolmogorov microscales.

The Kolmogorov length, time and velocity scales are defined as:

$$\eta = \left(\frac{\nu^3}{\epsilon}\right)^{\frac{1}{4}} [m] \tag{A.1}$$

$$\tau = \left(\frac{\nu}{\epsilon}\right)^{\frac{1}{2}} [s] \tag{A.2}$$

$$v = (\nu\epsilon)^{\frac{1}{4}} [m/s] \tag{A.3}$$

where ϵ is the average rate of dissipation of turbulence kinetic energy per unit mass, and ν is the kinematic viscosity of the fluid. ϵ is defined in equation A.4.

$$\epsilon = \left(\frac{u'^3}{L}\right) \tag{A.4}$$

From the simulation, u' is calculated. Since we know the computational domain length L, the dissipation rate is calculated from the above equation A.4.

By substituting ϵ and ν, the kolmogorov length and time scales are obtained. From the calculations, the time step and the length scale was found to be :

$$\Delta t = 4X10^{-6}[S] \tag{A.5}$$

$$\eta = 4X10^{-5}[m] \tag{A.6}$$

The number of elements in x,y and z direction can be obtained from the equation A.7.

$$N = \left(\frac{u'^3 * L}{\nu} \right)^{\frac{3}{4}} \tag{A.7}$$

The grid spacing 'dL' can be calculated by equation A.8.

$$N = \left(\frac{L}{dL} \right) \tag{A.8}$$

From the above equations, besides the time step, the filter length, grid spacing, number of elements in X, Y and Z direction are calculated.

B

CALCULATION OF JET REYNOLDS NUMBER

The jet Reynolds number is calculated from the following formulae:

$$\dot{m} = \rho * A * V_{in} \tag{B.1}$$

$$Re_j = \frac{4 * \dot{m}}{\pi * D_j * N * \mu} \tag{B.2}$$

From the above two equations, the mass flow rate, jet Reynolds number can be calculated. Table B.1 represents the Reynolds numbers at which CFD simulations are performed.

Table B.1: Calculation of jet Reynolds numbers for various inlet velocities

V_{in} [m/s]	$\dot{m}$ [Kg/s]	Re_j
0.5	$1.776 \text{ X } 10^{-5}$	420
0.75	$2.665 \text{ X } 10^{-5}$	620
1	$3.552 \text{ X } 10^{-5}$	810
1.5	$5.328 \text{ X } 10^{-5}$	1220
2	$7.104 \text{ X } 10^{-5}$	1625

The above calculations are obtained for 0.4 mm jet diameter with 7.5 jets in the array.

C

Pressure Drop Calculations From Analytical Approach

To understand the variation of pressure and pressure losses in the system, performing CFD simulations and experiments consumes lot of time and energy. Hence, there is a need for an inexpensive analytical approach to predict the pressure losses within a system. In the present study, a simple method known as sum of local resistances approach is used to predict the pressure drop with in the jet impingement system [Idel'chik and Isaak, 1996].

From the schematic of impinging system, it is assumed that the total pressure drop is the sum of pressure drops in nozzle inlet, nozzle outlet, frictional loses inside the nozzles and in the cross flow channel.

$$\Delta P = \Delta P_{n_{in}} + \Delta P_{n_{out}} + \Delta P_{n_{fr}} + \Delta P_{ch_{out}} \tag{C.1}$$

The local pressure drop can be defined by the pressure resistance coefficient as shown in equation eq:pd2

$$\xi = \frac{2.\Delta P}{\rho.V^2} \tag{C.2}$$

The friction inside nozzles can be calculated by:

$$\xi_{n_{fr}} = \frac{\lambda.L}{D} \tag{C.3}$$

Where λ is equal to: $\lambda = \frac{64}{Re}$ for laminar flow. Here, λ is the friction coefficient. In the cross flow channel, the pressure drop is given by the equation C.4

$$\Delta P_{ch} = \frac{\rho.V_{ch_{out}}^2}{2} \tag{C.4}$$

For nozzle inlet, the pressure drop is given by the equation C.5.

$$\Delta P_{n_{in}} = \frac{\rho . V^2 . \xi_{n_{in}}}{2} \tag{C.5}$$

Where $\xi_{n_{in}}$ is given by:

$$\xi_{n_{in}} = \frac{\left[1 - \frac{A_{in}}{A_{ch_{in}}}\right]^{\frac{3}{4}}}{2} \tag{C.6}$$

Similarly, at the nozzle exit:

$$\Delta P_{n_{out}} = \frac{\rho . V_{avn}^2 . \xi_{n_{out}}}{2} \tag{C.7}$$

Where $\xi_{n_{out}}$ is given by:

$$\xi_{n_{out}} = 1.0 \tag{C.8}$$

The pressure resistance coefficient is assumed to be 1 because, it is assumed that all the kinetic energy in the jet is lost due to the impingement. Furthermore, it was observed from the CFD simulations that, at the nozzle exit, the jet decelerates due to the effect of cross flow. However, the value of this coefficient depends on the nozzle location in the array.

BIBLIOGRAPHY

F. Peper, W. Leiner, and M. Fiebig, *Drying performance and surface forces of a pair of impinging radial jets,* Heat Mass Transfer **vol.30**, 313 (1995).

Je-Chin-Han, *Recent studies in turbine blade cooling,* International Journal of Rotating Machinery **vol.10(6)**, 443 (2002).

R. Viskanta, *Heat transfer to impinging isothermal gas and flame jets,* Exp. Thermal Fluid Sci. **vol.6**, 111 (1993).

J. Baughn and S. Shimizu, *Heat transfer measurement from a surface with uniform heat flux and an impinging jet,* Journal of Heat Transfer **vol.111**, 1096 (1989).

J. Lee and S. J. Lee, *The effect of nozzle configuration on stagnation region heat transfer enhancement of axisymmetric jet impingement,* Int. J. Heat Mass Transfer **vol.43**, 3497 (2000).

A. M. Huber and R. Viskanta, *Effect of jet-jet spacing on convective heat transfer to confined, impinging arrays of axisymmetric air jets,* Int. J. Heat Mass Transfer **vol.37(18)**, 2859 (1994).

S. Pope, *Turbulent flows* (Cambridge university press, 2000).

G. A. Rao, M. Kitron Belinkov, K. Vladimer, and Y. Levy, *Heat transfer investigations in multiple impinging jets at low reynolds number,* ASME TURBO EXPO, Glasgow, GT 2010 - 22720, June 14-18 (2010).

Idel'chik and E. Isaak, *Handbook of hydraulic resistance, 3rd ed.* , 790 (1996).

A. J. Yule, *Large-scale structure in the mixing layer of a round jet,* J. Fluid Mechanics **vol.89(3)**, 413 (1978).

D. Cooper, D. C. Jackson, B. E. Launder, and G. X. Liao, *Impinging jet studies for turbulence model assessment,* I. Flow-field experiments. Int. J. Heat Mass Transfer **vol.36(10)**, 2675 (1993).

M. J. Findlay, M. Salcudean, and I. S. Gartshore, *Jets in a crossflow: Effects of geometry and blowing ratio,* Journal of Fluids Engineering - ASME **vol.121**, 373 (1999).

R. Matsumoto, I. Ishihara, T. Yabe, K. Ikeda, S. Kikkawa, and M. Senda, *Impingement heat transfer within arrays of circular jets including the effect of crossflow,* In Proc. 5th ASME/JSME Joint Thermal Eng. Conf. **6386**, 1 (1999).

K. Kataoka, *Impingement heat transfer augmentation due to large scale eddies,* 9th Int. Heat Transfer Conf **vol.1**, 255 (1990).

J. N. B. Livingood and P. Hrycak, *Impingement heat transfer from turbulent air stream jets to flat plates,* NASA TM X-2778, a literature survey (1973).

K. Nishino, M. Samada, K. Kasuya, and K. Torii, *Turbulence statistics in the stagnation region of an axisymmetric impinging jet flow,* Int. J. Heat and Fluid Flow **vol.17**, 193 (1996).

M. Poreh, Y. G. Tsuei, and J. E. Cermak, *Investigation of a turbulent radial wall jet,* J. Appl. Mech. **vol.34**, 457 (1967).

C. O. Popiel and L. Boguslawski, *Mass or heat transfer in impinging single, round jets emitted by a bell-shaped nozzle and sharp-ended orifice,* In Heat Transfer 1986, volume 3 of Proc. 8th Int. Heat Transfer Conf. **vol.3**, 1187 (1986).

J. Barata, *Fountain flows produced by multiple impinging jets in a crossflow,* AIAA Journal **vol.33**, 2523 (1996).

L. W. Florscheutz, D. E. Metzger, and R. A. Berry, *Periodic streamwise variations of heat transfer coefficients for inline and staggered arrays of circular jets with crossflow of spent air,* Journal of engineering for gas turbines and power **vol.102**, 137 (1980).

K. Abe, T. Kondoh, and Y. Nagano, *A new turbulence model for predicting fluid flow and heat transfer in separating and reattaching flows,* Int. Journal of Heat and Mass Transfer **vol.37(4)**, 139 (1994).

G. A. Rao, M. Kitron Belinkov, and Y. Levy, *Numerical analysis of a multiple jet impingement system,* ASME TURBO EXPO, Florida, GT 2009 - 59719, June 8-12 (2009).

L. W. Florscheutz, D. E. Metzger, and C. R. Trumann, *Streamwise flow and heat transfer distribution for jet array impingement with crossflow,* Journal of engineering for gas turbines and power **vol.103**, 337 (1981).

R. J. Goldstein and A. I. Behbahani, *Impingement of a circular jet with and without crossflow,* Int. J Heat Mass Transfer. **vol.25**, 1377 (1982).

A. Leonard, *Energy cascade in large-eddy simulation of turbulent fluid flows,* Adv. Geophys. **vol.18A**, 237 (1974).

N. Uddin, N. Neumann, and B. Weigand, *Les simulations of an impinging jet: On the origin of second peak in the nusselt number distribution,* Int. J. Heat and Mass transfer **vol.57**, 357 (2013).

B. Whelan and A. Robinson, *Effect of nozzle geometry on pressure drop and heat transfer to both free-surface and submerged liquid jet arrays,* 5th European Thermal-Sciences Conference, The Netherlands (2008).

L. W. Florscheutz and H. H. Tseng, *Effect of non-uniform geometries on flow distributions and heat transfer characteristics for array of impinging jets,* Journal of engineering for gas turbines and power **vol.107**, 75 (1985).